# Detection and Analysis of Debris Discs

## Thesis

# Detection and Analysis of Debris Discs

The Open University

Jonathan Peter Marshall, MSci. MSc.

Department of Physics and Astronomy

The Open University

A thesis submitted for the degree of

*Doctor of Philosophy*

Awarded: 15th March 2011

Date of Submission: 15 June 2010

Date of Award: 15 March 2011



ProQuest LLC.
789 East Eisenhower Parkway
P.O. Box 1346
Ann Arbor, MI 48106 – 1346

# Acknowledgements

I am grateful to my supervisory team, Glenn White and Stephen Serjeant, for their guidance and support throughout my PhD, and for the efforts both they and my examiners, Jane Greaves and Hugh Jones, took to convert my rambling three year summary of 'some stuff I did' into a coherent scientific document.

At the Open University, I would like to thank the postdocs Lys, Robin and Calum for their generous help with the surprisingly wide range of unique and intractable problems I encountered (or, more usually, inflicted upon myself) during the course of this project. I am also indebted for the assistance of Geoff, the department's computer manager; without his long suffering support I'd never have been able to get anything done (or would have irretrievably lost the files).

In the course of my travels, I visited the Institute for Space and Astronautical Studies (ISAS) in Japan and Gemini South Observatory in Chile as part of my research training. I am grateful for both of these institutes for hosting me and would like to thank Takao Nakagawa at ISAS and Michelle Edwards at Gemini South in particular for sharing with me with their expertise in infrared astronomy.

During my PhD I made the acquaintance of many colourful characters. In no particular order, I would like to thank the following for their friendship; Michal, Stefano and Vladimir, the motley crew who made sharing an office a pleasure rather than a chore and the many (drink related, usually tea-based) memorable incidents our cohabitation provoked. Stacey, for her level-headed sense and an inexhaustible list of excuses to go and grab a takeaway pizza; Marc for his comfy

sofa and diplomatic silence during the six nations; Jonti, Andy and Kris with their boundless enthusiasm for adventures in grim darkness and adventures with near-lethal cocktails; Olly and Becca for letting me win at Mario Kart occasionally (then destroying me in Halo); Phil for his outstanding good humour in the face of absurdity and lastly, but by no measure least, Robin for his balletic grace, verbal dexterity and delicious chocolate cake.

Most importantly, I would like to thank my family for their emotional, physical and financial support throughout the decade long process that took me from undergraduate to doctorate. Your endless encouragement and unstinting belief were both needed and appreciated. Finally, I dedicate this work to my father, who died shortly after my viva examination, glad to have finally seen this star shine.

# Abstract

Debris discs are the dusty remnants of the planet formation process around main sequence stars, detected through their emission at infrared wavelengths. The study of these objects improves our understanding of both the frequency and the timescale of planet formation around other stars, and, in resolved disc systems, can be used as an indirect method of planet detection in regions of orbital radius-planet mass space where standard methods (e.g. radial velocity, transits) are insensitive.

In Chapter 1, an overview of debris discs is presented, summarising the key results since their discovery and a synopsis of the most recent results. The motivation and goals for the research undertaken in this thesis are also placed within the context of our current understanding of debris discs. In Chapter 2, the mathematics of the computer models used in fitting debris disc observations with physical structure and dust grain properties are explained, starting from the black body approximation.

In Chapter 3, a search for new YSO candidates in the L1551 region is presented, comparing the YSO population with both the Taurus cloud and other similar low mass star forming regions.

In Chapter 4, the results of a search for debris discs in the AKARI FIS all sky survey are presented. Over 50 debris disc candidates are identified in the survey, though half of these have been previously observed by *IRAS*. Two dozen new candidates are identified at 90 $\mu$m.

In Chapter 5, a search for mid infrared excess from DUNES sources in the AKARI

IRC point source catalogue is presented. Fourteen stars with infrared excess are identified, from the 102 stars with 18 $\mu$m photometry in the 133 star sample.

In Chapter 6, the *Herschel* ATLAS field observed during the science demonstration phase is analysed, looking for debris discs at sub-mm wavelengths. The surprising result indicates the presence of several very high mass discs ($> M_{\oplus}$), with no reported excess in the far infrared, implying these discs are widely separated from their stars and very cold.

In Chapter 7, a dynamical study of the HR8799 planetary system is presented, using the *MERCURY* code to test the stability of the observed planetary architecture over Myr timescales. From these simulations, the influence of planetary eccentricity on the system is determined, and a comparison made to previous dynamical models of the planets.

In Chapters 8 and 9, the main findings and conclusions of the thesis are summarised and discussed. A short section giving details of the current and near-future work being undertaken on the basis of this thesis is also provided.

# Contents

# List of Figures

# List of Tables

*Discworld constellations changed frequently as the world moved through the void, which meant that astronomy was cutting-edge research, rather than, as elsewhere, a clever way of avoiding a proper job.*

Pratchett, T.

# 1

# Introduction

Debris discs are the product of an ongoing planet formation process. These discs are composed of second generation dust grains containing silicates (both amorphous and crystalline), carbonaceous molecules and ices (e.g. $H_2O$, CO). The dust in the disc must be continually replenished as the lifetime of dust grains under the action of radiation forces and collisional events is at least an order of magnitude less than the parent star. This second generation dust is produced through the collisional grinding of an (unseen) population of larger (asteroidal) bodies (Backman & Paresce, 1993). Debris discs are relatively depleted of gas, containing little or no CO, geometrically thin and optically thin to their own radiation at far infrared/sub-millimetre wavelengths.

Since the detection of the first circumstellar debris disc around Vega from observations with *IRAS* in 1984 (Aumann et al., 1984), over 200 stars have been observed to exhibit a similar infrared excess that is attributed to the presence of a dust disc (Beichman et al., 2006a). Very few of these systems have been resolved[1], leading to difficulty in separating their physical structure and dust grain properties when modelling them. Debris discs are most easily observed at far infrared wavelengths, where the flux from the cold dust disc peaks, though subsequent observations have imaged known debris discs across the optical (scattered light) to sub-mm

[1] A catalogue of resolved discs is available at http://circumstellardisks.org/

wavelengths.

Studying debris discs is important for several reasons:

- To provide constraints on the absolute incidence of planetary systems around main sequence stars through observations of a statistically significant sample of stars;
- To provide constraints on the mechanisms (either through core accretion or gravitational instability) and the timescales for planet formation (and debris disc evolution) through observation of debris disc stars spanning a wide range of ages (10 Myr – 10 Gyr);
- To detect exoplanets in regions not easily accessible (low masses, large orbital radii) to traditional (e.g. radial velocity or transit) search methods.

In this thesis, I sought to address several specific questions, particularly:

- What is the total incidence of debris discs around main sequence stars near the Sun, using data from the AKARI FIS 90 $\mu$m all sky survey to detect cold dust emission with greater sensitivity than previously possible?
- How does the availability of longer wavelength data, used to better constrain the peak and Rayleigh-Jeans tail of cold dust emission from debris discs, impact on the physical parameters (e.g. mass/temperature) of previously known debris discs (through *IRAS* or *Spitzer* observations) and our understanding of the structure and dynamics of these objects?

In the following Introduction, I will summarise the historical context on which this work is based, and explain how our understanding of debris discs and their evolution has developed through two and a half decades of ground and space based observations. I will also highlight modelling advances that have underpinned our physical understanding of discs and the dust from which they are formed, which will lead into the second introductory Chapter. In Chapter 2, I will describe the mathematical basis of the debris disc computer models that have been used

to obtain quantitative predictions of physical parameters of the disc structures, their masses and dust grain properties. I will also justify the use of particular assumptions used in models, both in this work and the literature, and in particular regarding the use of simple modified black body dust thermal emission models. In Chapter 3, a project to search the L1551 Dark Nebula for faint YSOs using archival *Spitzer* IRAC (InfraRed Array Camera) observations will be presented and compared with previous surveys of the region, and with similar studies of other nearby low-mass star forming regions. We link this study of protostellar regions to their eventual debris disc phase. In Chapter 4, I present results from a search for debris discs in the AKARI far infrared All Sky Survey between 65 and 160$\mu$m and compare the results with *IRAS* and *Spitzer* survey results. In Chapter 5, AKARI IRC observations at 9 and 18 $\mu$m of the DUNES (DUst around NEarby Stars) sample of 133 stars are examined for signs of infrared excess. In Chapter 6 I will present the preliminary findings of a study of an *Herschel* ATLAS field which I have used to serendipitously search for debris discs in the cosmology fields of that program. In Chapter 7, a study of the dynamical stability of the exoplanet and debris disc system HR8799 is presented. The planets around HR8799 were recently discovered by direct imaging techniques and the long term dynamical stability of the three planet system is still in doubt. The results of our simulations look to constrain the combinations of orbital radii and eccentricity that result in stable configurations for the observed planetary masses, assuming the system is presented to us face-on. In Chapter 8, I will summarise the main findings of the work presented in the previous five chapters, and discuss these results in the context of the scientific questions that this work seeks to address, and their contribution to the development of our broader understanding of debris disc evolution. In Chapter 9, I will finish this work with a recapitulation of the conclusions presented in earlier chapters and present some future research opportunities that I will be pursuing based on these results.

## 1.1 Observation

### 1.1.1 Photometry

Different wavelengths sample different dust populations, both in the size of the grains responsible for the emission, and their physical location within the disc (see Fig. 1.2, from Thébault & Augereau, 2007). Mid infrared photometric data sample the warm inner regions of the disc around the Habitable Zone, i.e. the region around the star within which there can exist liquid water on a planetary surface (Kasting et al., 1993). It is sensitive to surface emission from that region (the disc 'atmosphere') and to the emission from small dust grains ($r_{dust} < 10\mu$m), which are hotter due to being inefficient radiators (see Chapter 2.4.1). At far infrared wavelengths, colder dust dominates the SED and the wavelength at which the SED turns over can be used to probe the orbital radius of the dust from the star. Sub-mm photometry can be used to determine the disc mass, as the disc is both optically thin at longer wavelengths and larger mm – cm sized dust grains dominate the observed emission.

### 1.1.2 Spectroscopy

Mid infrared spectroscopy can be used to detect silicate emission features around 8 – 13 $\mu$m from small grains (diameters < 10 $\mu m$) in debris discs. The dust observed in mature debris discs has undergone processing compared to the primordial ISM and a comparison of dust emission features between stars at different ages should reveal an 'evolutionary sequence' of the dust. Primordial dust is produced in a variety of locations, including the atmospheres of cool giants (e.g. Mira variables), novae and supernovae (Jones, 2005). The composition of the dust is a mixture of oxygen-rich silicates and carbon-rich dust. Silicate dust comes in two forms: olivine ($Mg_{2x}Fe_{2(1-x)}SiO_4$)and pyroxenes ($Mg_xFe_{(1-x)}SiO_4$), where the subscript $x$ refers to the number of atoms of a particular element in the preceding expressions. Common mineral species observed both in interstellar and solar system dust include the olivines fayalite ($x = 0$) and fosterite ($x = 1$), and the pyroxenes ferosillite ($x = 0$) and enstatite ($x = 1$)

(Molster, 2003). It should be noted that $x$ can adopt any value from 0 – 1 in the mineral formulae. The dust composition is dependent on its source and the temperature and pressure at the point of formation. For a given pressure, pyroxine dominates the composition at low temperature (Pollack et al., 1994). Silicate grains formed in supernovae and star formation regions are generally Fe-rich and amorphous, but at high temperatures Mg-rich crystalline species are made (Dwek, 2005). In the ISM, only amorphous olivine and pyroxine dust species are observed, providing evidence for processing of material in debris discs due to the silicate features seen in the spectra of pre-main sequence stars (and some debris discs) (Bouwman et al., 2001; Whittet et al., 1997).

In the ISM, which is cold and at low pressure, a mixture of amorphous olivines and pyroxines are observed, dominated by olivine. A comparison between the diffuse ISM and molecular clouds and YSOs suggests some processing of material before the start of the star formation, with the dominant mineral component switching from amorphous olivines to amorphous pyroxines. The material in molecular clouds is kept amorphous due to the effect of cosmic ray impacts. In the solar system, the crystalline fraction of cometary dust is too high by ~ 30% to be explained as primordial ISM material, which has a crystallinity of < 2% (Kemper et al., 2004).

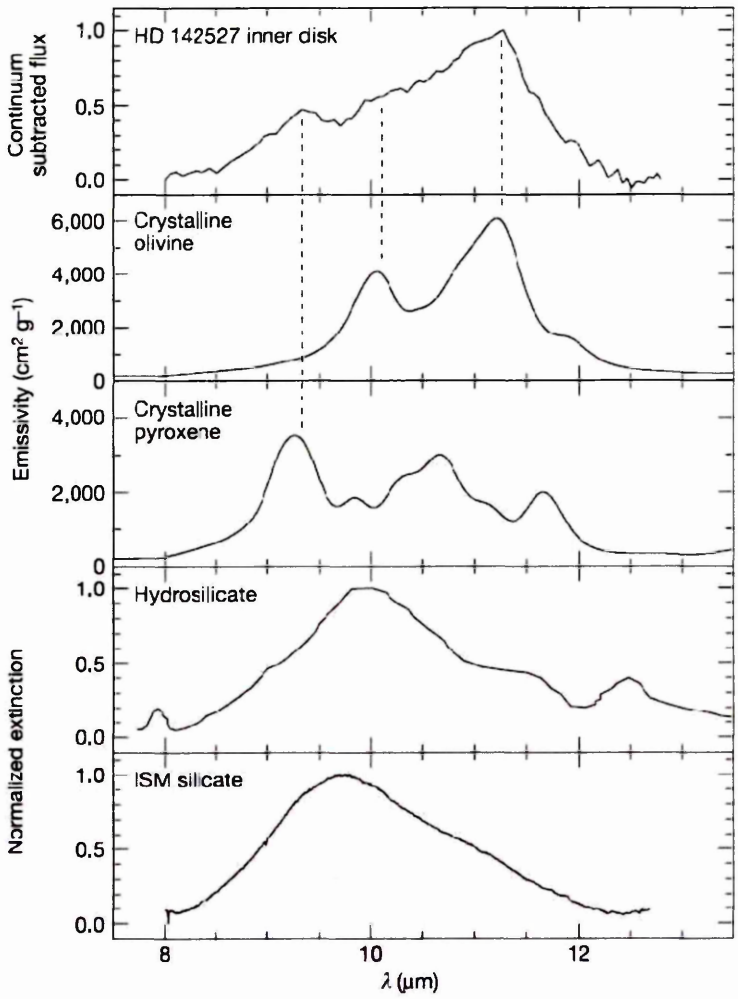


Figure 1.1: Spectrum of the inner disc of HAe star HD144432 compared to mineral spectra and ISM dust. The observed disc spectrum shows a marked difference from the ISM dust, indicative of dust processing within the disc. There are several crystalline emission features in the 8 – 13 $\mu$m region, the most prominent of which is at 11.3 $\mu$m. Diagram taken from van Boekel et al. (2004)

Models of these spectral features can reveal information on the size of dust grains from the shape and strength of the emission features and their crystallinity from the relative strength of peaks at 9 and 11 $\mu$m in the dust spectrum. The shape of the features in this wavelength regime is dependent on a number of factors including: the dust mineral composition; the presence of refractory coatings on the grains (organic species can alter the optical depth of grains at longer wavelengths); the shape of the grains (e.g. spherical or ellipsoidal) and the size of the grains (grains larger than 10 $\mu$m have very weak emission features). Comparison of debris disc dust spectra to solar system examples, e.g. asteroidal or cometary dust, have also been made. These studies revealed similarities between the mineralogy of comets and debris disc dust, e.g. comet Halley (Bregman et al., 1987) with $\beta$ Pictoris (Knacke et al., 1993) and Hale-Bopp (Wooden et al., 1999) with $\beta$ Pictoris, HD144432 and HD69830 (Butner et al., 2003; Lisse et al., 2007; Zuckerman et al., 2001, respectively). Most debris discs observed by the *Spitzer* IRS do not show strong silicate features, implying that the dust grains are mostly $\gtrsim$ 10 $\mu$m in size in those discs (Beichman et al., 2006b; Jura et al., 2004). This may be a function of the observed sample of debris discs being biased towards high mass discs around early spectral type stars (since they are predominantly *IRAS* discovered), where the dust evolution may be quicker (Chen et al., 2006).

Observations of large, young discs have shown that the signature of silicate emission from the disc can change with the radius (van Boekel et al., 2004). This is to be expected, as the inner, hotter regions of the disc are the likely source of crystalline material, whilst dust in the cooler, outer regions remains relatively pristine and amorphous. There is some evidence to suggest that irradiation from the star may play a part in the amorphisation of dust in circumstellar discs (Glauser et al., 2009), and that radial transport of dust through the disc will act to dilute the relationship between dust location and its processing history. The strength of the silicate features have been observed to be stable over periods ~ years for mature discs (Kessler-Silacci et al., 2005), but can vary widely over the space of months to years in younger objects, likely due to the changing composition of dust brought up into the disc atmosphere from the mid-

plane (Przygodda et al., 2003; van Boekel et al., 2003).

## 1.2 Morphology

### 1.2.1 Spectral Energy Distribution

Thermal emission models (black or grey body) can be fitted to photometric observations of a disc to estimate the typical parameters for a disc, e.g. disc mass, dust temperature and disc radius, assuming an underlying particle size distribution and a choice of the physical/optical properties for the grains. The results of disc models derived from photometry alone are degenerate, with a range of values for several parameters often describing the same observations equally well. Photometry in the far infrared regime is important to constrain the shape of the disc emission profile around, and beyond, the SED turnover point (which typically lies in the region 60 – 100 $\mu$m) because the falloff of a debris disc SED does cannot be fitted with a simple black body. High quality photometry covering this region densely enables some structures in the debris disc to be discerned, e.g. *Spitzer/CSO* observations of $\epsilon$ Eridani (Backman et al., 2009). From the shape of their SEDs it can be inferred that most debris discs have a central clearing of up to several 10s of AU across (Bryden et al., 2006).

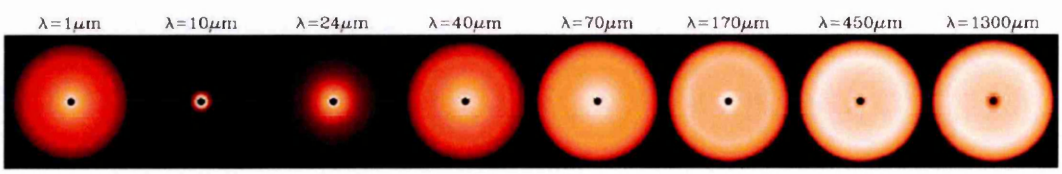


Figure 1.2: Series of model images of a massive face-on debris disc showing the evolution of the resolved emission as a function of grain size and wavelength. The brightness scale of the images is logarithmic. See Chapter 2 for further details.

### 1.2.2 Imaging

A picture is worth a thousand words. This is particularly true for debris disc modelling, due to the degeneracies between various parameters in the models e.g. dust grain size and disc radius, both of which affect the temperature of the dust grains (see Chapter 2.4.1 for more details). More than 200 stars have been identified to possess debris discs, but only the brightest and closest of these have been spatially resolved.

A wide variety of structures have been observed in the ~20 debris discs that have been spatially resolved, including gaps (Koerner et al., 1998), rings (Ardila et al., 2004; Holland et al., 2003; Kalas et al., 2007a; Schneider et al., 2006; Smith et al., 2009), warps (Weinberger et al., 2003), clumps (Greaves et al., 1998), offsets between star and disc centre (Kalas et al., 2004) and disc asymmetries (Holland et al., 1998; Kalas et al., 2007b). Many discs display several of these morphological structures, particularly the presence of an inner gap and outer ring of dust. Some of these structures, e.g. warps in the disc, and clumps of dust, can only be explained by the presence of a Jupiter-mass planet perturbing the orbital motions of the dust grains and shaping the disc. Multi-epoch sub-mm images of the $\epsilon$ Eridani disc show some evidence (at 2-$\sigma$ level) of a rotation in the disc over a period of six years (Poulton et al., 2006), but this picture may be confused by the mis-identification of background objects as structure in the dust ring (Backman et al., 2009).

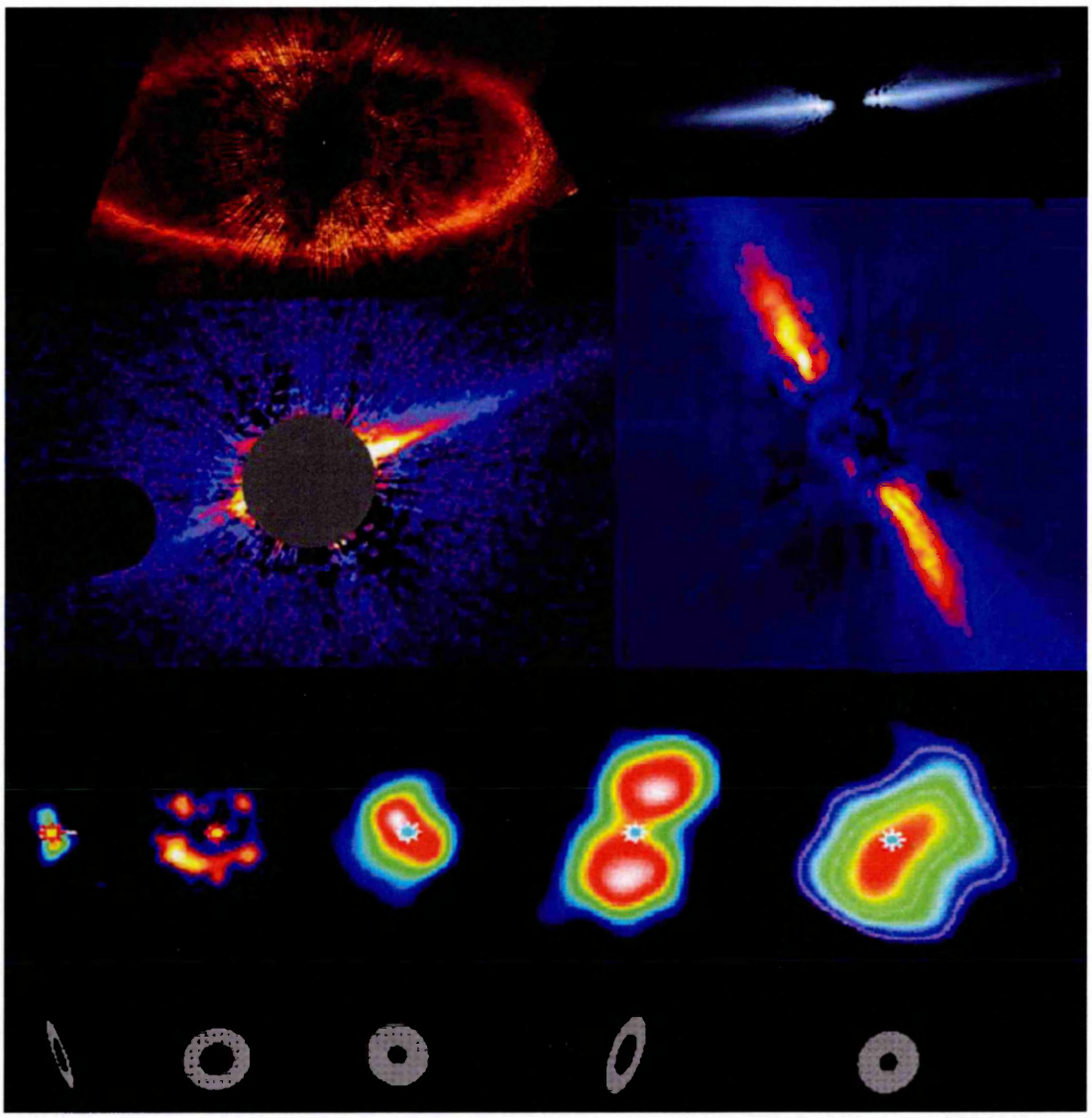

Figure 1.3: Images of several resolved debris disc systems, clockwise from top left: Fomalhaut in scattered light (Hubble ACS); AU Microscopii in scattered light(Hubble ACS); $\beta$ Pictoris at 10$\mu$m (Gemini TReCS);(l-r) $\tau$ Ceti, $\epsilon$ Eridani, Vega, Fomalhaut and $\eta$ Corvii (JCMT-SCUBA); HD15115 in scattered light (Hubble ACS).

## 1.3 Dynamics

### 1.3.1 Dust-Planet Interaction

The inner regions of most mature debris disc systems show signs of clearing, implied from the lack of 24 $\mu$m excess around stars with 70 $\mu$m excess in *Spitzer* surveys of main sequence stars. At young (< 10 Myr) ages, the reduction in near infrared emission from disc systems is attributed to the twin processes of dust settling to the mid-plane of the system and the growth of the dust grains. Whether this clearing is achieved from the inside out (i.e. by stellar radiation pressure) or from the outside in (i.e. blocking of inward migration by a planet, Rice et al., 2006) is still uncertain. The most likely explanations invoke the presence of a massive planet inside the inner edge of the debris disc, a view which is supported by the recent direct imaging of Jupiter-mass exoplanets in just such locations around stars with debris discs (Kalas et al., 2008; Marois et al., 2008). Other explanations for constraining the dust at the outer edges of the disc have been postulated, e.g. photophoresis (Krauss et al., 2007), but rely on the presence of a specific combination of dust grain size and remnant gas density to be effective at constraining the radial spread of dust grains. Three debris disc systems; Fomalhaut, Beta Pictoris and HR 8799 (Kalas et al., 2008; Lagrange et al., 2008; Marois et al., 2008, , respectively), have been imaged with orbiting planets in positions likely to interact with the disc, although the dynamical implications are not yet fully understood in any of these cases.

In addition to acting as a barrier to the inward migration of dust grains, the presence of a Jupiter-mass planet in a debris disc system can also impact on the orbits of bound dust grains. If dust grains are in a mean motion resonance (MMR) with the planet, the dust will be filtered such that the long-lived dust grains are shepherded into orbits that do not approach the planet, similar to the orbital resonance between Neptune and Pluto in the solar system. To an external observer, the disc emission will appear to be offset from the star into one (or more) clumps (Reche et al., 2008; Wolf et al., 2007). These clumps of dust form structures that are much larger than the exoplanet and therefore act as a possible detection mechanism for planets around

other stars, opening up regions of mass–orbital radius phase space to planet detection which would otherwise be difficult to probe due to the long timescales required and weak influence of the planet on the host star. Clumps attributed to the presence of an unseen planet have been observed at sub-mm wavelengths in images of both the $\epsilon$ Eridani and Vega debris discs (Greaves et al., 2005; Marsh et al., 2006, respectively). If the planet orbits the star at an angle inclined to the plane of the debris disc, its orbital motion will excite the inclination of any dust grains it passes close to. This sort of interaction presents itself as a warped disc, or an inclined secondary disc at an angle to the bulk of the debris disc. The $\beta$ Pictoris debris disc has been observed in scattered light to have an inclined secondary disc and a warped main disc (Augereau et al., 2001; Burrows et al., 1995).

## 1.4 Temporal Evolution

### 1.4.1 Formation

Stars form from the collapse of the dense regions (cores) of molecular clouds in the interstellar medium. As the molecular cloud core collapses it fragments into several protostellar cores, each of which will go on to form a star. Due to the presence of some initial rotational motion in the molecular cloud, the in-falling material of the protostellar core is supported against collapse by the conservation of angular momentum and magnetic fields, creating a disc around the protostar (Shu & Adams, 1987; Shu et al., 1987). Matter falling onto the circumstellar disc from the surrounding envelope is accreted by the protostar until the disc is depleted of material or the star becomes bright enough that its radiation pressure or stellar wind drives off the material starting from the innermost regions of the accretion disc. As the disc is being depleted of gas, planet formation is occurring with the removal of gas pressure support in the disc allowing the density of dust in the disc mid-plane to increase. By 10 Myr after formation, almost all stars have lost the gas from their primordial discs, placing a strict constraint on the timescale for the formation of gas giant planets.

### 1.4.2 Sculpting

Three major processes dominate dust grain lifetimes in a debris disc; Poynting-Robertson drag, radiation pressure and collisional destruction (Backman & Paresce, 1993). All of these processes act on timescales much shorter than the stellar lifetime, implying that the dust discs around these stars are not primordial. An unseen population of larger asteroidal bodies is invoked as the mass reservoir for the production of dust grains that we observe in the disc (Artymowicz, 1997; Dominik & Decin, 2003).

#### 1.4.2.1 Poynting-Robertson Drag

The Poynting-Robsertson effect (Robertson, 1937) is a relativistic phenomenon that causes a dust grain orbiting a star to appear to 'see' a headwind of blue shifted stellar photons as it orbits the star. These photons are absorbed and re-emitted isotropically causing a net loss in angular velocity via momentum transfer, thereby causing the dust grain to slow and spiral inwards towards the star. This is most effective on dust grains around cm size, and typically causes the inward spiral of a dust grain from 1 AU in less than a hundred years.

$$t_{PR} = \frac{4\pi a\rho}{3}\frac{c^2 r^2}{L_\star} \tag{1.1}$$

In the above equation, the timescale for loss via PR drag, $t_{PR}$, in years is a function of the grain diameter $a$ and density $\rho$ (in cgs), combined with the orbital radius of the grain $r$ (in AU) around a star of luminosity $L_\star$ (in solar units).

Overcoming the rapid loss of these cm sized grains from the disc by this process is a major problem in current planet formation theories, requiring rapid growth of dust grains from cm to metre sized particles in a matter of years. Dust destruction via PR drag dominates grain removal in debris discs with low surface densities (radiatively dominated discs), such that the grains can travel a significant distance without suffering a collision.

#### 1.4.2.2 Radiation Pressure

Radiation pressure dominates the motions of the smallest sub-micron grains in the disc, driving them out of the system on timescales comparable to that of their orbital period. Dust grains are described by the $\beta$ parameter, the ratio of gravitational to radiation pressure forces acting on them (Burns et al., 1979). Smaller dust grains effectively see a reduced gravitational potential from the central star. $\beta$ values of less than one define grains on bound orbits, while $\beta$ values greater than unity describe the motion of grains on unbound orbits.

$$\beta = \frac{\mathrm{F}_{rad}}{\mathrm{F}_{grav}} = \frac{3L_{\star}}{32\pi cGM_{\star}a\rho} \tag{1.2}$$

In the above equation, the ratio of the radiation and gravitational forces on the dust grain, $\beta$, is a function of the stellar luminosity $L_{\star}$ and mass $M_{\star}$, and grain radius $a$ and density $\rho$.

From the ratio, $\beta$, of these two forces the limiting case of $\beta = 1$ can be calculated. For this case, both outward and inward forces are balanced and the particle remains in a circular orbit, though the effective potential acting on it is zero. Since both the radiation pressure and gravitation vary according to inverse square laws, the ratio of the two forces is constant through the entire disc, so from this relation the minimum size of any bound dust grain in any part of the disc can be determined.

#### 1.4.2.3 Collisional Destruction

In dense debris discs (those with high fractional luminosities) the mutual collision of dust grains, producing a cascade of smaller dust grains (which are subsequently removed via radiation pressure) is the dominant dust destruction mechanism (collisionally dominated discs). Nearly all of the currently known debris discs are in this regime (due to instrument sensitivity favouring the detection of bright, dense and hot dust discs), with a few low S/N detections of EKB analogues around Sun-like stars having been made by *Spitzer* (Greaves & Wyatt, 2010) that are approaching the limits on EKB flux set by *IRAS* and *COBE* at 60 $\mu$m favouring an

upper limit < 1 MJy/sr (Aumann & Good, 1990; Backman et al., 1995).

Small grains being removed from the system by radiation blow-out are especially effective at causing destructive collisions with larger circularly orbiting grains. Considering a grain that moves in a circular orbit with a sinusoidal vertical motion such that it passes through the entire disc width twice per orbit, the timescale for mutual collisions in a disc is:

$$t_{col} \simeq \frac{1}{2\pi a^2 \sigma(r)\Omega} \simeq \frac{2.5 \times 10^6 r_{AU}^{3/2}}{a_{\mu m}^2 \sigma(r)} \left(\frac{M_\odot}{M_\star}\right)^{1/2} \quad \text{yr} \tag{1.3}$$

In the above equation, the timescale for collisional destruction, $t_{col}$, in years is a function of the dust grain radius $a$, disc surface density $\sigma$, orbital radius $r$ and the stellar mass $M_\star$.

This collisional timescale is important only for discs with large amounts of small grains propagating through them, e.g. discs undergoing collisional cascade due to the recent catastrophic disruption of a large cometary body. In a collisional cascade the destruction of two minor planet sized bodies in the system produces large numbers of small dust grains, causing a temporary brightening of the disc. Such events occur stochastically and the brightness increase is short lived ($t_{cc} \sim 10^4$yrs, Rieke et al., 2005). The grains produced in the collision are swiftly removed from the system by the radiative mechanisms previously discussed.

### 1.4.3 Decay

Almost all stars begin their existence surrounded by a disc of gas and dust (Haisch et al., 2001; Shu et al., 1993). After ~6 Myr (3–5 Myr around early type stars), the incidence of circumstellar dust drops to zero (see Fig. 1.4, Haisch et al., 2001; Hernández et al., 2007). The removal of these primordial protoplanetary discs is not 100% efficient (the dust mass in a typical debris disc is $10^{-2}$–$10^{-3}$ of that in a protoplanetary disc, see Fig. 1.5), and the remaining material in the protoplanetary disc after the gas clearing has taken place constitutes the source material for the planetesimals that will eventually become parent bodies of the dusty debris disc.

The incidence of infrared excess around stars has been observed to fall off with a power law decay with a slope of -2, determined from *IRAS* and *ISO* observations of young stellar clusters (Spangler et al., 2001). This is conflict with later results, e.g. Hernández et al. (2007) (see Fig. 1.4) which find a shallower fall off. This is explained as the Spangler et al. results only sampling the brighter end of the stellar disc mass distribution, the objects which constitute it are unrepresentative of the broader sample.

The rate of disc decay around A stars has been measured for both warm (mid infrared excess at 24 $\mu$m) and cold (far infrared excess at 70 $\mu$m) debris discs by *Spitzer* (combined with some *IRAS* and *ISO* results Rieke et al., 2005; Su et al., 2006, for warm and cold excess, respectively). In both cases, the decay in excess can be fitted by a fuction $t_0/t$, where $t_0$ ~150 Myr for warm excess and $t_0 \geq$400 Myr for cold excess. This implies the inner regions of the debris disc evolve more quickly, which is expected from dynamical consideration of the dust motions. The slope of the decay, as a function of $1/t$, implies that the dust destruction is collisionally dominated. This is expected as current debris disc surveys are sensitivity limited, only able to detect discs that are much more massive than the Edgeworth-Kuiper belt.

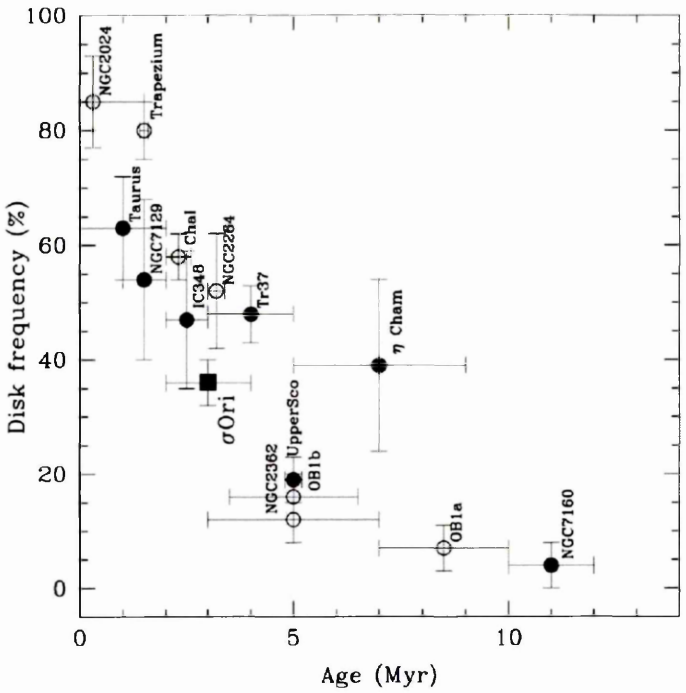


Figure 1.4: Disc frequency vs. Age for young stellar clusters, from Hernández et al. (2007).

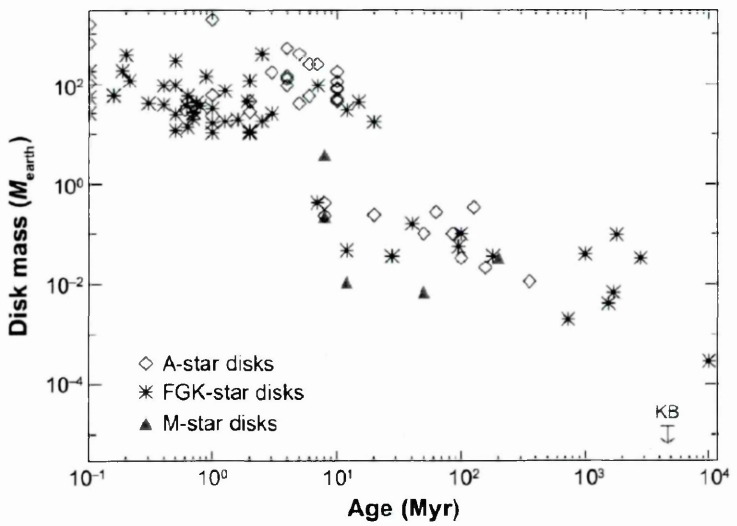


Figure 1.5: Mass vs. Age for known protoplanetary and debris discs, taken from Wyatt (2008). Note the step change around 10 Myr. An upper limit for the Solar System's Edgeworth-Kuiper belt (from Greaves et al., 2004) is included in the bottom right corner.

## 1.5 Frequency

Around main sequence stars of spectral types A – M the total incidence of debris discs is 2±2 % for hot dust and 16±3% for cold dust, derived from *Spitzer* MIPS measurements at 24 and 70 $\mu$m (Trilling et al., 2008). The incidence of debris discs is seen to decline from early to late spectral types, but this may be a selection effect due to the discs around A stars being more massive and hotter, making them more easily detected than those around later stars.

Initial results from *ISO* and *Spitzer* suggested a decline in incidence across F, G and K spectral types (Beichman et al., 2006a), but more recent results show that there is no significant difference between the fraction of disc stars, despite there being almost a factor of five difference in mass between F and K stars (Trilling et al., 2008). There is a paucity of debris discs around M stars, which is probably a selection effect due to the discs around these stars being fainter and cooler than earlier spectral types. A weak constraint on the incidence of debris discs around M stars has been made through mm wavelength observations, placing their frequency at 5%, cf 22% for A stars and 15% for FGK stars (Lestrade et al., 2009).

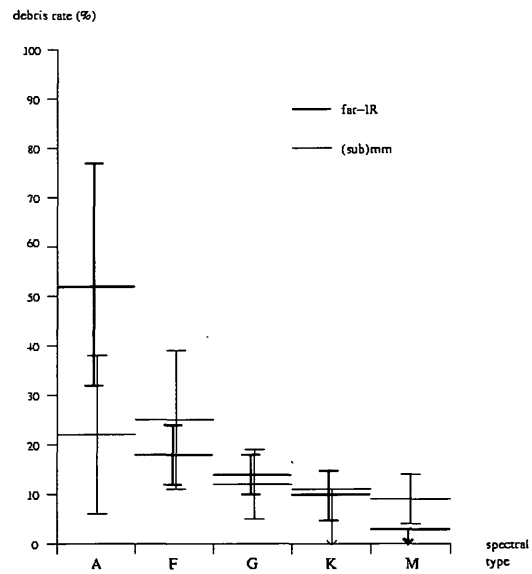


Figure 1.6: Plot of the incidence of debris discs around main sequence stars at far infrared and sub-mm wavelengths from *IRAS*, *ISO* and *Spitzer* results as a function of spectral type. Taken from: http://www.jach.hawaii.edu/JCMT/surveys/dds/

Around close binary stars (separations of a few stellar radii) with a massive (A or F spectral type) primary, the incidence of debris discs is elevated compared to field stars, decreasing around binaries with intermediate separations before increasing to disc frequencies similar to those of field stars of the same spectral type for widely separated binaries (Trilling et al., 2007). This implies that dust production is not inhibited in binary systems, although the formation of larger than planetesimal-sized bodies may be inhibited by gravitational forces, limiting the planetary evolution in such systems.

No debris discs have been detected around the most massive O and early B type stars, due to the large distances to these stars, their rapid evolution shrouding them in the material from which they formed and location within dense stellar environments causing source confusion.

In contrast to exoplanet searches, there is no correlation between the presence of a debris disc and stellar metallicity (Greaves et al., 2006; Moro-Martín et al., 2007a). Only eleven systems have been identified with both an exoplanet (or exoplanets) and a debris disc (see e.g. Kalas et al., 2008; Marois et al., 2008; Moro-Martín et al., 2007b, for details).

## 1.6 Comparison to the Solar System

The Solar System has a debris disc consisting of two separate parts: an inner warm dust disc, the zodiacal dust disc, formed from the main asteroid belt at ~ 3.2 AU); and an outer cool disc, the Edgeworth-Kuiper belt, formed from bodies > 30 AU). This zodiacal dust disc has been observed since the late middle ages (Cassini, 1683) and its structure has been modelled from observations by both *IRAS* and *COBE*. The outer cold component of the Solar System debris disc (SSDD) is too faint to be detected by current instrumentation, and therefore assumed to be an order of magnitude fainter than the limit of current detector capability. The SSDD has not always been faint, indeed models of the early Solar System imply that due to planetary orbital migration, responsible for the Late Heavy Bombardment, the SSDD was abnormally bright (Gomes et al., 2005). More recent estimates of the variability of the zodiacal dust cloud

(from the density of $^3$He in ocean sediments), estimate variation by a factor of 0.6 – 2.6 in the amplitude of the zodiacal dust emission over the past $10^5$ yr (Kuchner, 2008), despite evidence for the breakup of a large comet in the inner Solar System during this period (e.g. Napier, 2010). Estimates of the fractional luminosity and mass of the outer belt, which dominates the Solar System's debris disc emission, are $10^{-7}$ – $10^{-6}$ $L_\odot$ (Stern, 1996) and ~ $10^{-1}$ $M_\oplus$ (Greaves et al., 2004). In comparison, the asteroid belt is believed to have a fractional luminosity ~ $10^{-8}$ – $10^{-7}$ $L_\odot$ (Dermott et al., 2002).

The Solar System is believed to be atypical and comparisons between observed debris discs around nearby field stars and our own should be made with caution. Evidence from both radioactive isotopes in meteorites (Cameron & Truran, 1977; Tachibana et al., 2006) and the sharp cut off at the outer edge of the Edgeworth-Kuiper belt (Quillen et al., 2004) can be interpreted as evidence that the Solar System formed in (or nearby) a dense OB association, in contrast to the debris disc stars we observe in the solar neighbourhood which, from their galactic motions, appear to have originated in less dense, low mass star formation regions similar to Taurus (Song et al., 2003).

# 2

# Modelling Debris Discs

## 2.1 Spectral Energy Distribution

In the absence of resolved emission or images of a debris disc, its physical properties can only be derived from its SED. Most discs have only been observed by one instrument at several wavebands, and thus the number of data points on which to base a model of the disc is also limited. This applies a limit to both the complexity of the model that can be made of a given data set, and the amount of information that can be derived from an SED alone.

Due to the model dependent nature of the SED analysis, physical parameters such as the temperature, grain size and dust optical properties are degenerate. This is true even for well studied debris discs with imaging and photometry across a broad range of wavelengths e.g Augereau et al. (2001); Li & Greenberg (1998) for $\beta$ Pictoris, or Su et al. (2005) for Vega.

## 2.2 Physical Properties

### 2.2.1 Fractional Luminosity

The fractional luminosity, $\tau$, of a debris disc is the ratio of the infrared and stellar emission, $\tau = L_{ir}/L_{\star}$. It is a measure of the total incident stellar radiation intercepted by the disc and therefore

is an approximation of the disc total optical depth. Debris discs have $\tau$ values of $< 10^{-3}$, since they are optically thin, whilst transitional and protoplanetary discs have larger fractional luminosities (approaching 0.1 for the youngest/most massive). The fractional luminosity of a disc can be approximated from the ratio of the peak flux and wavelength at which emission peaks for both star and disc:

$$\tau = \frac{F_{d,max}}{F_{\star,max}} \frac{\lambda_{\star,max}}{\lambda_{d,max}} \tag{2.1}$$

where the disc fractional luminosity $\tau$ is the peak flux and wavelength of the disc, $F_{d,max}$ and $\lambda_{d,max}$, divided by the star's peak flux and wavelength, $F_{\star,max}$ and $\lambda_{\star,max}$ (Wyatt, 2008).

The impact of the temperature and fractional luminosity on a debris disc SED can be seen in Fig. 2.1. Assuming the dust emission comes from a narrow annulus of black body grains, the wavelength of peak emission and dust temperature are related through Wein's law (given here for the Planck function, $B(\nu, T)$):

$$T_d = 2989/\lambda_{d,max} \tag{2.2}$$

As previously stated, most debris disc SEDs peak at wavelengths between 30 – 100 $\mu$m implying dust temperatures 100–30 K, respectively. These temperatures are indicative of a dust belt at similar orbital distances to the Edgeworth-Kuiper belt (10s of AU).

### 2.2.2 Temperature

The shape of the disc SED is defined by the temperature and emissivity of its constituent dust grains, which depend on the dust optical properties. The simplest assumption that can be made to model dust emission is that it emits as a black body, i.e. the dust grains act as perfect spherical grains in thermal equilibrium with the incident stellar radiation field, emitting their radiation isotropically. The intensity of radiation at frequency $\nu$ from a black body surface of temperature $T$ is given by the Planck function:

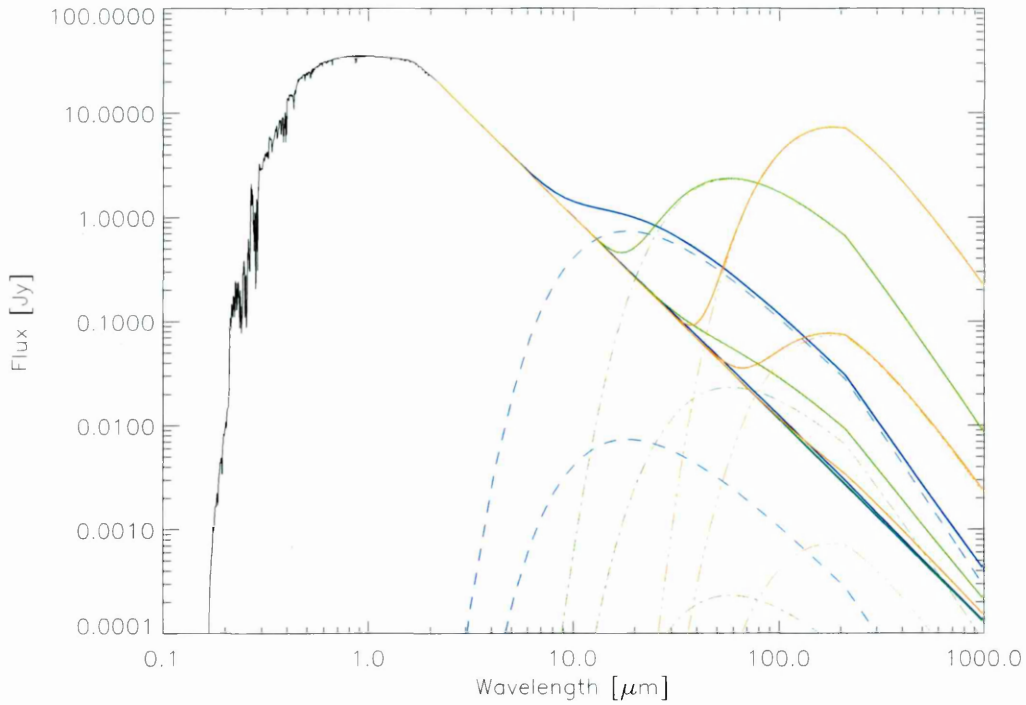


Figure 2.1: Figure illustrating the impact of fractional luminosity and temperature on the shape of a debris disc's SED. The stellar photosphere is a G2V star at 10 pc (black solid line), and three disc component with temperatures of 278, 88 and 28 K (equivalent to dust at 1, 10 and 100 AU for black body grains) indicated by blue, green and red lines respectively. The total emission of the disc and star is indicated by solid lines, whilst the disc contribution at each temperature is given by a broken line (dashed, dot-dash or triple dot-dash) in the appropriate colour. Each temperature component is scaled with fractional luminosities of $10^{-3}$, $10^{-5}$ and $10^{-7}$ (after Wyatt, 2008).

$$B(\nu, T) = \frac{2h\nu^3}{c^2}\left(e^{\frac{h\nu}{kT}} - 1\right)^{-1} \tag{2.3}$$

Using Stefan's law the integrated intensity can be related to the effective temperature of the stellar surface (where $\sigma$ is the Stefan-Boltzmann constant):

$$\sigma T^4 = \pi \int_0^\infty \mathrm{B}(\nu, T)\,\mathrm{d}\nu \tag{2.4}$$

The total emitted power (luminosity) of a star is therefore the surface area of the star multiplied by the energy it emits across all frequencies per second:

$$L_\star = 4\pi R_\star^2 \sigma T_\star^4 \tag{2.5}$$

The flux incident on a dust grain from the star at an orbital distance $R_{dust}$ is the luminosity of the star divided by the surface area of a sphere of radius $R_{dust}$ (assuming $R_{dust} \gg R_\star$, broadly true for main sequence dwarfs):

$$F_\star = \frac{L_\star}{4\pi R_{dust}^2} \tag{2.6}$$

The flux absorbed by a spherical grain of radius $a_{dust}$ at distance $R_{dust}$ from the star is the area of incident radiation that the grain intercepts multiplied by the fraction of the stellar flux that the grain absorbs:

$$F_{abs} = \pi a_{dust}^2 (1 - A_{dust}) F_\star \tag{2.7}$$

The radiation absorbed by the grain will heat it and be re-radiated in turn as the grain's own luminosity. Assuming that the grain also acts as a black body (i.e. $A_{dust} = 0$), the dust luminosity and temperature can therefore be calculated.

$$L_{dust} = F_{abs} = 4\pi a_{dust}^2 \sigma T_{dust}^4 \tag{2.8}$$

Rearranging Eqn. 2.8 for temperature:

$$T_{dust} = \left( \frac{L_{dust} R_{\star}^2 T_{\star}^4}{R_{dust}^2} \right)^{0.25} \tag{2.9}$$

We can also derive an effective radius at which the dust is located, giving an estimate of the extent of the disc. This tells us if the disc location is similar to the asteroid belt or the Edgeworth-Kuiper belt in the Solar System (where 278 K is the temperature of a dust grain at 1 AU from the Sun):

$$R_{dust} = (278/T_{dust})^2 L_{\star}^{0.5} \tag{2.10}$$

The treatment presented here is very simplistic, but suffices for systems where the infrared excess is only weakly constrained by one or two data points. It should be noted that the assumption of black body emission can underestimate the radial location of the dust by up to a factor of three compared to using e.g. astrosilicate dust models to fit observations of resolved debris discs. A more sophisticated approach to estimating the dust temperature is presented in Sect 2.4.1, and the impact of adopting 'real' materials for the dust optical properties is discussed in Sect 2.4.3.

### 2.2.3 Mass

At long (sub-mm and mm) wavelengths, a debris disc is optically thin through its entire width, and therefore the observed flux from a disc can be assumed to be a measure of the emission from all the material in the disc. The mass, $M_{dust}$, of a debris disc can be derived from the sub-mm flux, $S_{\nu}$:

$$M_{dust} = \frac{S_{\nu} d^2}{B(\nu, T)\, \kappa_{abs}} \tag{2.11}$$

The value of $\kappa_{abs}$ has been estimated as 1.7 $\mathrm{cm^2 g^{-1}}$ at 850 $\mu$m (Zuckerman & Becklin,

1993). The disc mass derived from the sub-mm flux does not measure the mass held in dust grains larger than ~300 $\mu$m, due to the fall off in emissivity at longer wavelengths. The total disc mass must therefore be estimated by assuming a maximum size for particles in the disc (e.g. 1000 km asteroids) and scaling the mass derived from the PSD appropriately based on the sub-mm measurement.

## 2.3 Thermal Emission

### 2.3.1 Disc

Resolved observations of debris discs show that they are not thin annuli or shells of dust at tightly constrained orbital radii, but can extend out to 100s of AU from their parent star. To calculate the total observed emission for a model disc, we therefore integrate the observed emission from a number of discrete annuli between the inner and outer extent of the disc, within which the disc temperature can be assumed constant. The contribution to the thermal emission at wavelength $\lambda$, $F(\lambda)$, from a disc annulus width d$R$ at a distance $R$ from a star composed of dust grains radius $a$ can be calculated from:

$$F(\lambda) = \sigma(R)\epsilon(a,\lambda)B(\lambda,T)\frac{2\pi R\mathrm{d}R}{d^2} \tag{2.12}$$

Where $\sigma(R)$ describes the variation of the disc surface density with respect to radial distance, for which most discs have a $\tau \propto R^{-1.5}$, as predicted in (Strubbe & Chiang, 2006). The emissivity, $\epsilon(a,\lambda)$ represents the inefficiency of emission and absorption of radiation by dust grains much smaller than the wavelength of the radiation (see next section). The distance $d$ is that of the star from the observer. At sub-mm wavelengths, $\lambda > 210\ \mu m$, a further factor $\propto (1/\lambda)$ is required to fit models to the observed fluxes, due to the lower surface area to volume ratio of larger dust grains resulting in a reduced contribution to the total emission (Dent et al., 2000; Williams & Andrews, 2006).

### 2.3.2 Star

The total emission from a debris disc system is dominated by the dust contribution at far infrared wavelengths, outweighing the photospheric contribution to the total emission by several orders of magnitude (incidentally providing hope for the direct detection of terrestrial exoplanets, Kaltenegger et al., 2004).

Accurate determination of the stellar spectral type is important in the mid infrared (around 20 $\mu$m) where the dust excess may be small (perhaps only a few percent of the total flux), and the photospheric contribution is large. It is also important more generally for determining the radiation budget of the dust disc, where the dust radial location determined through modelling is sensitive to the (assumed) stellar luminosity and temperature. Although main sequence stars are faint in the far infrared, giant (spectral class III) stars are infrared bright and constitute a large source of contamination when cross matching stellar catalogues which have no spectral type information.

The spectral type of a star can be determined via photometry by fitting its optical and near infrared colours (differences in magnitudes between various wavelength bands) to those of standard stars. Using this process, the distance to a star can also be measured (Eqn. 2.13), typically to within 20% (compared to HIPPARCOS parallaxes).

$$m_V - M_V = 5log_{10}(d) - 5 + A_V \tag{2.13}$$

The distance $d$ is a function of the difference between the absolute ($M_V$) and apparent ($m_V$) magnitudes and the interstellar extinction ($A_V$).

The colours of standard stars, both dwarfs (V) and giants (III) are taken from Bessell & Brett (1988) and Glass (1999). A least squares minimisation of the observed colours to the given standards is made weighted by the uncertainties and allowing for interstellar extinction, and thus the spectral type is determined, more or less accurately.

### 2.3.3 Correction Factors

The AKARI FIS detectors have a relatively large response over broad wavelength ranges (see Fig. 2.3), and this response is not uniform with wavelength. The observed flux, $F_\nu$, of a source must therefore be corrected for the colour (temperature) of the source being observed. This is known as the colour correction factor. The corrected flux $F_{\nu,cc} = F_\nu / K$, where $K$ is the colour correction factor.

The colour correction factor for a source at temperature $T$ in a waveband is determined by the integral sum of the flux of a flat spectrum ($\nu F(\nu)$ = const.) at the detector central frequency divided by the observed flux multiplied by the detector spectral response $R$ (normalised to the central frequency).

The colour correction factor is usually only of the order ~ a few percent for the dust temperatures in debris discs, though for steeply rising (or falling) emission profiles (i.e. very cold or very hot bodies at FIS wavelengths), the colour correction is large (see Table 2.1).

$$K = \int \frac{F_{obs}(\nu)}{F_{flat}(\nu)} R(\nu) \mathrm{d}\nu \tag{2.14}$$

Table 2.1: FIS colour correction factors for black body emission profiles. Taken from Verdugo et al. (2007) (all sky survey) and Shirahata et al. (2009) (slow scan).

| Waveband | Temperature [K] | | | | | |
|---|---|---|---|---|---|---|
| | 10 | 30 | 50 | 100 | 300 | 3000 |
| N60 | 3.38 | 1.05 | 0.98 | 0.99 | 1.03 | 1.05 |
| WIDE-S | 1.84 | 0.89 | 0.98 | 1.15 | 1.32 | 1.40 |
| WIDE-L | 1.55 | 0.96 | 0.94 | 0.93 | 0.94 | 0.94 |
| N160 | 1.10 | 0.99 | 0.99 | 0.99 | 0.99 | 0.99 |

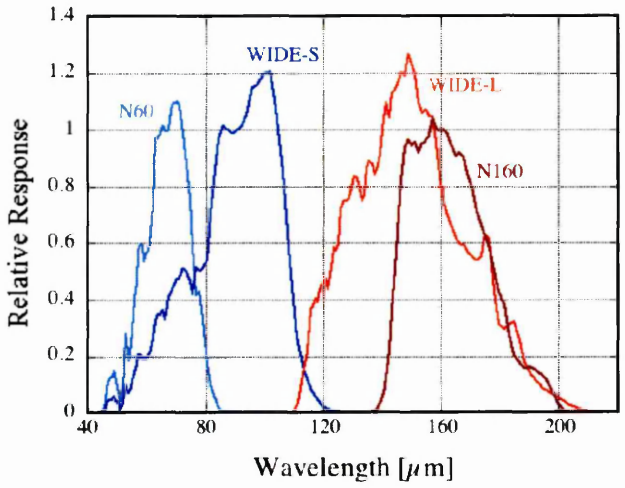


Figure 2.2: The spectral responses of the four FIS detectors, normalised to their nominal wavelengths: 65, 90, 140 and 160 $\mu$m, taken from Verdugo et al. (2007).

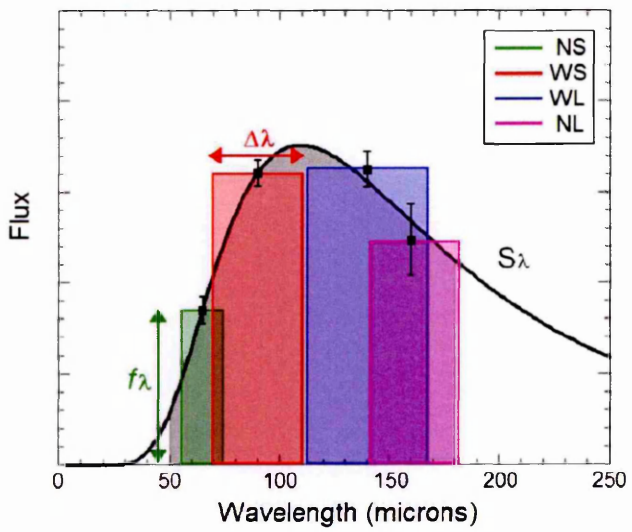


Figure 2.3: On a plot of flux vs wavelength, the bandwidths of the four FIS detectors (solid oblongs) are plotted with a 50 K black body emission curve. The black body curve is typical of the expected temperature of cold, Edgeworth-Kuiper belt like, debris disc dust that we hope to find in the AKARI FIS all sky survey (figure courtesy of M. Etxaluze).

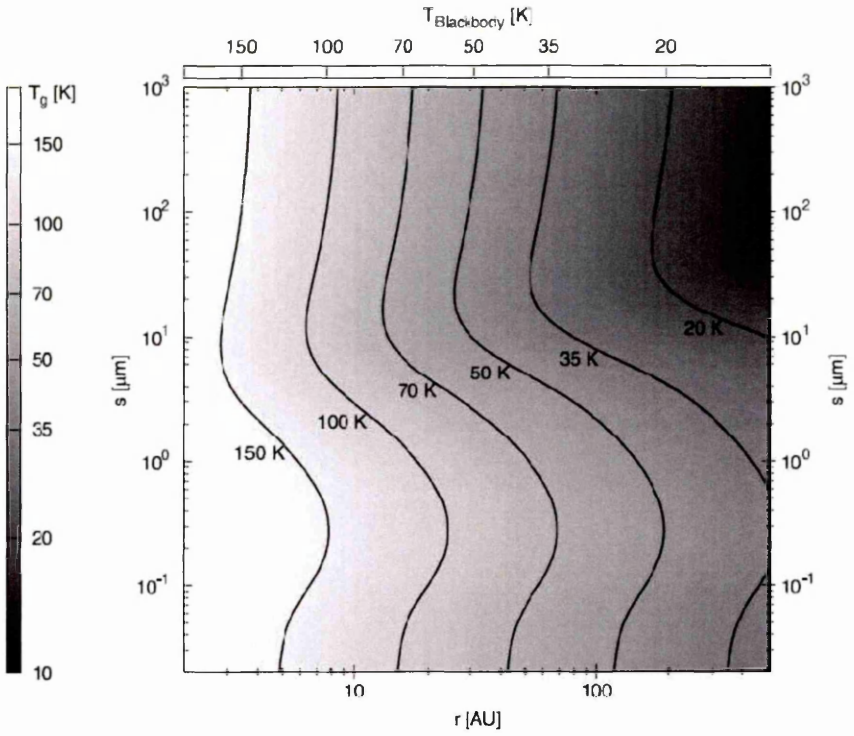


Figure 2.4: Diagram to illustrate the degeneracy between the dust grain size and temperature. Solid lines mark the temperature isolines for grains with the size given on the vertical axis. Horizontal axes are (top) black body temperature and (bottom) radial distance for the given temperature, whilst vertical axis is the size of the dust grain (adapted from Krivov et al., 2006).

## 2.4 Optical Properties

The optical properties of a dust grain depend on its size, shape and physical composition (see Fig. 2.4, from Krivov et al., 2006). Whilst the following section has been split into three parts along those lines, these facets of dust modelling are mutually interdependent, and there is some cross over between the sections below.

### 2.4.1 Particle Size

In the previous section, it was assumed that the disc was composed of large, single sized, spherical dust grains acting like perfect absorbers and emitters across the full wavelength range. In reality, the emissivity, $\epsilon$, of a dust grain with diameter $a_{dust}$ is a function of the wavelength which it is radiating (Greenberg, 1978). For dust grains that are larger than a critical wavelength, $\lambda_0$, the emissivity is unity and the grains act like black body emitters. The critical wavelength is approximated as:

$$\lambda_0 = \frac{a_{dust}}{2\pi} \tag{2.15}$$

The ratio of the critical wavelength and the dust grain radius varies depending on the optical properties of the dust. Grains emit radiation less effectively at wavelengths longer than the critical wavelength such that the emission is reduced by a factor:

$$\epsilon(\lambda) = \left(\frac{\lambda_0}{\lambda}\right)^{\beta} \tag{2.16}$$

The exponent $\beta$ is dependent on the dust grain material, varying between 1 – 2, dependent on the material properties. Values of $\beta$ around 1 are typical of amorphous materials whilst values around 2 are more closely approximated by crystalline dielectrics and metals (Witt, 1989).

The efficiency of absorption is also affected by the size of the dust grain. Grains that are much smaller than the peak wavelength of incident light (sub-micron grains, e.g. ISM dust) will be both poor absorbers and emitters of radiation and can be heated greatly by single UV photon absorption events. The temperature of such grains can be estimated as a function of the dust orbital radius and grains size (Backman & Paresce, 1993):

$$T_{dust} = 636 L_{\star}^{2/11} R_{AU}^{-4/11} (T_{\star}/T_{\odot}) \tag{2.17}$$

Grains that are larger than the incident radiation, but smaller than the peak wavelength of dust emission are efficient absorbers, but inefficient emitters of radiation, and therefore have a temperature-orbital radius relationship (Backman & Paresce, 1993):

$$T_{dust} = 468 L_{\star}^{0.2} R_{AU}^{-0.4} \lambda_0^{-0.2} \tag{2.18}$$

The dust particle size distribution in a debris disc can be more realistically modelled as a power law profile $N_a \propto a^{-3.5} \mathrm{d}a$ (Dohnanyi, 1969; Mathis et al., 1977). This is appropriate for the young and massive debris discs since the dust dynamics will be collisionally dominated, but in mature debris discs the presence of large amounts of small dust grains can be interpreted as a sign of a recent catastrophic break up due to the mass loss from the system associated with small dust grains being unsustainable over the lifetime of the disc (Su et al., 2005). The SED of a disc with a power law PSD can be mimicked by a dust disc composed of single sized grains (Backman et al., 1992). In such a case, the model can only constrain the minimum size of dust grains, such that $a_{min} = a_{dust}/4$.

In reality the PSD is not a power-law and the relative frequency of dust grains is a function of their size. The collisional destruction of larger grains by those slightly smaller creates deviations from a power law distribution of grain sizes, and the removal of the smallest grains from the system by radiation blowout (see Fig. 2.5 Campo Bagatin et al., 1994; Thébault & Augereau, 2007). A test of the veracity of this theoretical PSD will be possible with *Herschel* sub-mm observation of debris discs.

### 2.4.2 Grain Structure

Solar system interplanetary dust particles (IDPs), similar to those that may be found in debris discs, have a poor resemblance to the smooth spherical grains often assumed in disc emission models (Sandford, 1996). These IDPs have a complex, 'fluffy' (porous), fractal structure (see Fig. 2.6). The optical properties (e.g. albedo, absorption efficiency and scattering asymme-

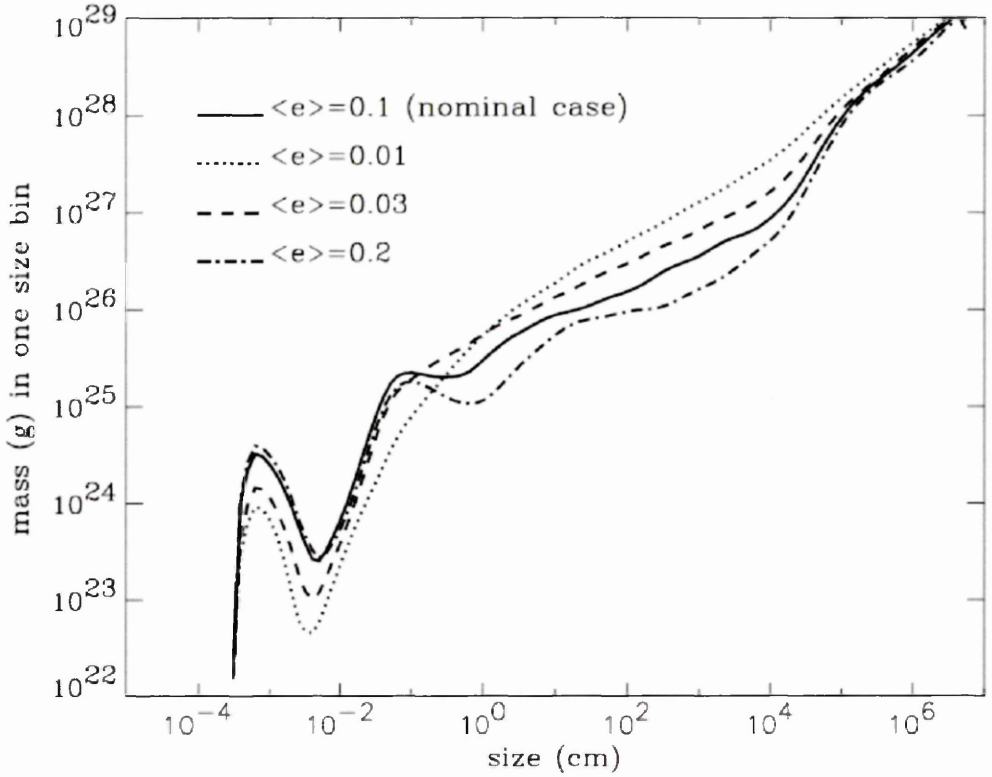


Figure 2.5: Distribution of dust grains (mass vs. particle size) in a massive circumstellar disc collisionally evolved from a power law distribution for 10 Myr, summed across the entire disc (from Thébault & Augereau, 2007). The parameter $< e >$ denotes the mean initial eccentricity of the dust grains in the disc.

try) of dust grains of a given size can be calculated from the efficiency derived from dielectric coefficients using Mie Theory (Bohren & Huffman, 1983; Wolf & Voshchinnikov, 2004). Fortunately, the scattering efficiencies of these particles are similar to the spherical approximation (Lumme & Rahola, 1994; Shen et al., 2009).

Dust models of the $\beta$ Pictoris disc emission revealed that the mid-infrared features could not be reconciled with the bulk cold dust emission by use of compact particles. Using porous dust grains (Iatì et al., 2001), both the emitted flux and dust distributions could be successfully modelled in each of these systems (see Greenberg & Li, 1997). This was taken to imply a cometary (opposed to an asteroidal) origin for the dust in these systems. In other examples,

e.g. AU Mic (Augereau & Beust, 2006), the assumption of dust grains as hard spheres proved adequate to replicate the SED and brightness profile of the disc.

Dust optical properties can be determined through either modelling astronomical observations (e.g. of the ISM Draine & Lee, 1984; Weingartner & Draine, 2001), or via laboratory experiment on analogues of interstellar dust materials (e.g. particular mineral species/ices Gálvez et al., 2009; Henning et al., 1999; Henning & Mutschke, 1997). Models of circumstellar dust based on ISM observations are applicable due to the similar chemical composition, despite the different PSDs in the two environments (Beckwith & Sargent, 1991; Mathis et al., 1977).

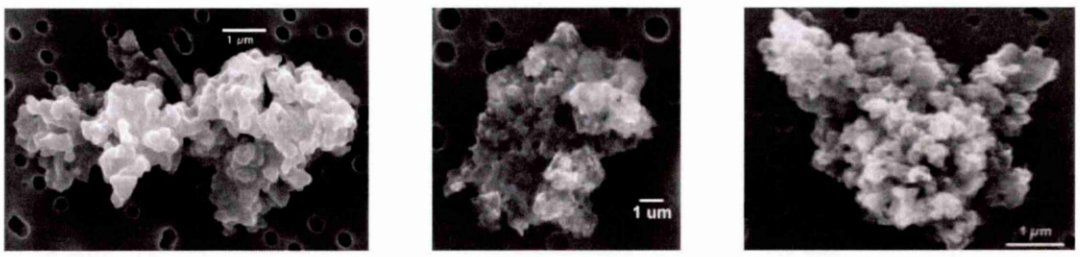


Figure 2.6: Images of typical dust grains from interplanetary sources, taken from Grn, E. and Gustafson, B.A.S. and Dermott, S.F. and Fechtig, H. (2001). Scale bars are included for each of the grains.

In this thesis we have assumed that the dust grains are grey body spheres. Whilst clearly an erroneous assumption, the lack of more detailed information (e.g. mid infrared spectra, resolved or scattered light observations) above and beyond the disc SEDs for many of the debris discs in this thesis do not justify the use of more advanced dust models than this.

### 2.4.3 Dust Composition

The dust in circumstellar discs shows a much greater crystalline content compared to the ISM, where such grains are quickly destroyed (and amorphised) by e.g. the harsh radiation environment, cosmic ray sputtering and supernova shocks. Initial efforts focused on replicating broad

silicate features observed in the ISM through comparison with materials such as 'astronomical silicate' (Draine & Lee, 1984; Draine & Li, 2001), or broad categories of materials e.g. a mixture of silicate, graphite and SiC species. Since the advent of *Spitzer* IRS spectroscopy, a determination of likely dust material composition can be made through least-squares fitting of an ensemble of dozens of mineral and ice materials to the disc infrared spectrum, revealing similarities between the dust in different debris discs and Solar System archetypes (e.g. cometary or asteroidal dust) (e.g. Lisse et al., 2007, and other references in Sect 1.1.2).

# 3

# *Spitzer* IRAC Observations of L1551

## 3.1 Introduction

In this Chapter we summarise an investigation into the YSO population of the L1551 Dark Nebula. As a young, low mass star formation region, the stars observed in this environment are progenitors of the main sequence field stars we observe in the stellar neighbourhood. At an age of ~ 1 Myr, the discs around the stars in this environment are still optically thick and gas rich, quite different from the debris discs they will eventually become. Studying these discs provides insight into the timescale for disc clearing processes (Bouwman et al., 2008) and a snapshot of the earliest stages of planet formation (Greaves et al., 2008).

The L1551 dark nebula is part of the Taurus-Auriga complex. As a nearby (Kenyon et al., 1994, $d = 140 \pm 10$ pc) site of low mass star formation it is well studied (Fridlund et al., 2005; White et al., 2006, 2000), not only in the infrared, but across the spectrum from X-rays (Favata et al., 2003) to sub-millimetre (Di Francesco et al., 2008) wavelengths. The region shows signs of recent star formation activity including complex outflow and jet structures from sources within the cloud (Fridlund & White, 1989; Stojimirović et al., 2006), pre-main sequence stars (Briceño et al., 1998) and Herbig-Haro objects (Devine et al., 1999; Fridlund & Liseau, 1994, 1998; Fridlund et al., 1993). The region is dominated by two pairs of sources; HL and XZ

Tau and L1551 NE and L1551 IRS5. Analysis of the extent of the bipolar outflow from HH30 (Burrows et al., 1996), a nearby Herbig Haro object, gives an estimated age of $\sim 10^5$ yrs (Stapelfeldt et al., 1997), in agreement with the observed (proto-)stellar population. Also, the very large $\approx$ 1 pc) outflow centered on L1551 IRS5/NE (Fridlund & White, 1989; Phillips et al., 1982, 1988; Rainey et al., 1987), has a dynamical timescale of between $\sim 10^4 - 10^5$ yrs (Fridlund et al., 1989). Many of the YSO sources observed within L1551 are found to be binary (incidence of 0.4 $\pm$ 0.08, Ghez et al. (1993)) or multiple stars including L1551 NE (Emerson et al., 1984; Moriarty-Schieven et al., 2000) and, very prominently, L1551 IRS5 (Fridlund & Liseau, 1998; Liseau et al., 2005; Rodríguez et al., 1998; Rodríguez et al., 2003).

Previous published infrared surveys of the region looking for YSOs include observations made with balloons (Fridlund et al., 1980), *IRAS* (Emerson et al., 1984), *ISO* (Gålfalk et al., 2004) and most recently, *Spitzer* (Luhman et al., 2009). In the ISO study, 15 new Young Stellar Objects (YSOs) were identified from 6.7 $\mu$m and 14.3 $\mu$m images out of a total of 97 sources. A recent analysis of the L1551 region was carried out by Moriarty-Schieven et al. (2006). Their results pointed to evidence of an ongoing, multigenerational star formation process in L1551, associating a molecular cloud core, previously identified from $NH_3$ and CO emission (Swift et al., 2005, 2006), with an extended sub-millimetre source (Moriarty-Schieven et al., 2006; Swift & Welch, 2008).

The data indicate the birth of a T-association, or low mass open cluster with about 100 members of which 81 are associated with X-ray sources by Favata et al. (2003), and are made up of both young classical T Tauri stars (CTTS), as well as older weak line T Tauri stars (WTTS). This suggests that the age of the cluster is around at least $10^6$ years. Star formation is, however, evidently still ongoing as indicated by the presence of a large number of embedded objects, such as the above mentioned L1551 NE and IRS5, which are still accreting heavily. Whether star formation has been episodic or is continuous has not been answered at this time. It is, however, one of the youngest and closest regions of its kind and as such constitutes a laboratory within which to examine the formation of low mass stars. It would therefore be

desirable to determine if there are several populations of objects indicative of several instances of star formation.

## 3.2 Observations and Data Reduction

### 3.2.1 Infra-red Observations

The observations presented here are from the *Spitzer* public archive (P6 - Structure and incidence of young embedded clusters, PI: Fazio). The observations were taken on $10^{th}$ June 2004. Data for all four IRAC (Fazio et al., 2004) wavebands (3.6, 4.5, 5.8 and 8.0 $\mu$m – channels 1 to 4, respectively) were obtained for processing and analysis. The original archive basic calibrated data products (bcds) for each waveband cover a region of$\sim$ $0.6^\circ \times 0.5^\circ$ in L1551 centered on $4^h31^m38^s$ $18^d14^m20^s$ (J2000). As High Dynamic Range (HDR) data, there are two complementary data sets covering the same field with exposure times of 0.6s and 12s. In our analysis we have used only the long exposure data, in order to be able to simultaneously trace both the faint emission and the point sources in the region, which is vital for determining the true nature of red sources, where shocked emission can be mistaken for YSOs.

Each of the four mosaics consists of 84 separate bcds. Before mosaicing, the bcds were corrected for artifacts using the artifact mitigation scripts written by S. Carey, available from the SSC website. Subsequent bcd processing was carried out using the relevant MOPEX processing scripts from v18.2.2 of the *Spitzer* MOPEX GUI with the standard (default) settings, combined with the latest dead pixel masks and IRAC Point Response Functions (PRFs) from the *Spitzer* Science Centre (SSC) website[1].

Sources in each of the four mosaiced images were identified and measured using aperture photometry performed with the *Spitzer* APEX scripts, controlled via the MOPEX GUI. Aperture photometry was performed with a 2 pixels radius aperture and an annulus of 12 – 20 pixels in order to limit the contamination from background flux, particularly for the 5.6 $\mu$m and 8.0 $\mu$m

[1] http://ssc.spitzer.caltech.edu/irac/

images. Appropriate aperture corrections and colour corrections were applied according to the annulus dimensions and position of the source on the bcd (see IRAC data handbook v3.0[1]).

Using the position errors calculated by APEX, sources were correlated between the four bands. In total, 193 sources were identified with fluxes in all of the images. Source spectral index values were calculated using the 3.6 $\mu$m and 8.0 $\mu$m fluxes, while fluxes from all four bands were used to plot their positions on a colour-colour diagram.

Additional 2MASS (Skrutskie et al., 2006) observations on the region were obtained from the IPAC on-line infra-red archive[2]. Of the 193 IRAC sources, 169 had 2MASS counterparts. These sources were correlated with observed IRAC sources to obtain near-mid infra-red spectral energy distributions and to enable a comparison between the stellar photospheric emission and longer wavelength fluxes. Targets in the 2MASS and IRAC data were considered coincident if their positions lay within 1.2″. Typical RA and Dec position errors for the mosaics were ~1.0″ in 3.6 $\mu$m and ~1.4″ in 8.0 $\mu$m.

The source SEDs show some extinction in the *J*,*H* and $K_s$ bands. The source of this reddening was assumed to be the sum of the extinction within L1551 itself and the extinction from the interstellar medium. In order to calculate and correct for the line of sight extinction, a stellar spectral type for each source was estimated from the 2MASS colours compared to standards from Bessell & Brett (1988). The difference between the observed and predicted K-band magnitudes for a star of the same spectral type as the source at a distance of 140 pc was assumed to be the total line-of-sight extinction for that source in the $K_s$ band. Using the $K_s$-band extinction and the IRAC reddening laws from Flaherty et al. (2007), the observed IRAC colours were dereddened.

[1] http://ssc.spitzer.caltech.edu/irac/dh/iracdatahandbook3.0.pdf
[2] http://www.ipac.caltech.edu/

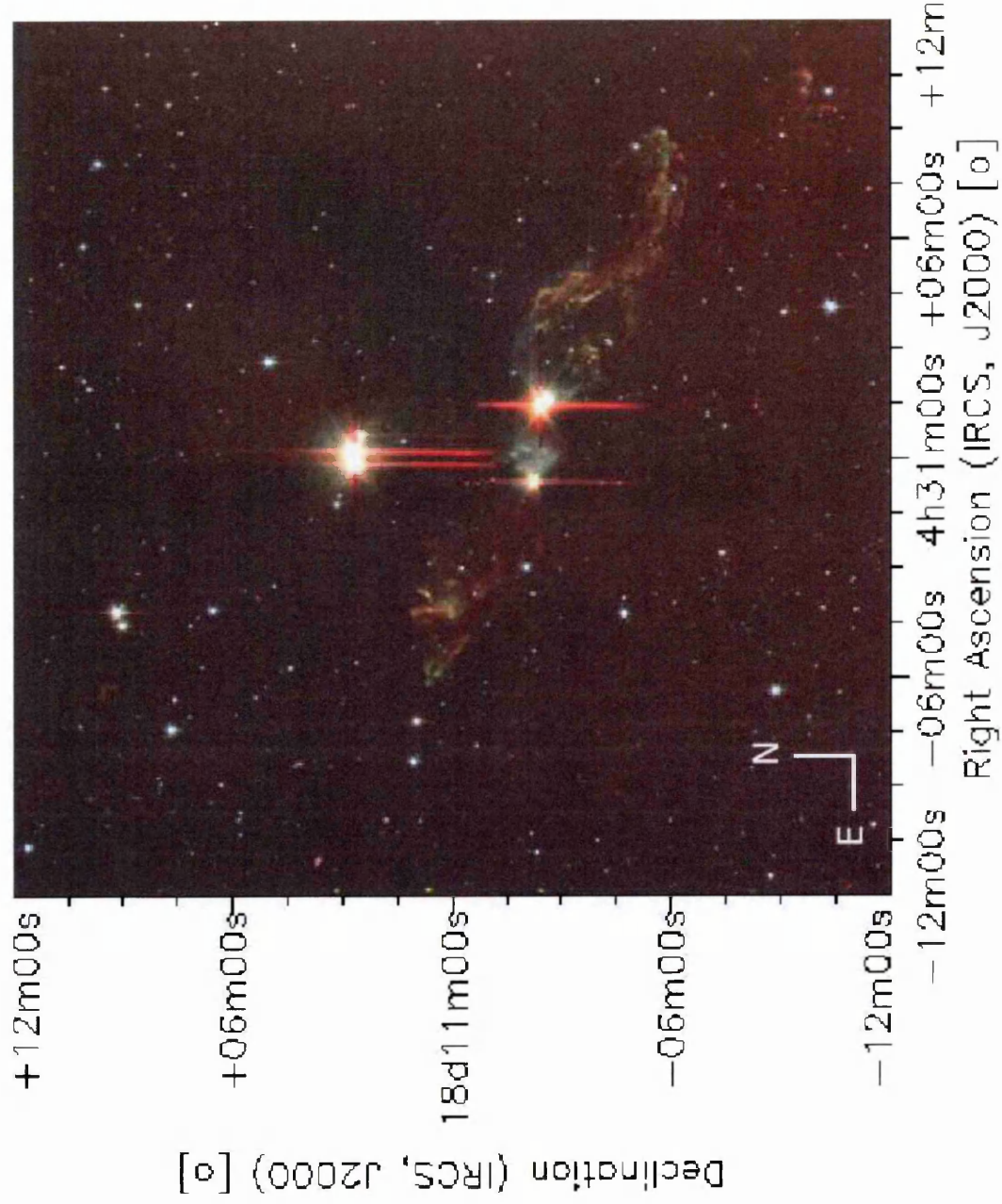


Figure 3.1: False colour image of the L1551 Dark Nebula, created from combined *Spitzer* observations at 3.6, 4.5 and 8.0 $\mu$m.

## 3.3 Results

### 3.3.1 Candidate YSOs

For all the sources with 3.6 and 8.0 $\mu$m fluxes their spectral index (Lada, 1987) was calculated using Eqn. 3.1. The spectral index $\alpha_{3.6-8.0}$ in the mid infra-red can be used to distinguish between YSOs and field stars, and between different classes of YSO. Three classes of YSO were defined by Lada (Lada & Wilking, 1984), corresponding to the three later stages of YSO evolution from embedded protostar (class I) to bare photosphere (class III). The limits of each YSO class with respect to $\alpha$ and their relative abundances in the L1551 sample are given in Table 3.1.

$$\alpha_{\lambda_1-\lambda_2} = \frac{\log_{10}(F_{\lambda_2}/F_{\lambda_1})}{\log_{10}(\lambda_2/\lambda_1)} - 1 \tag{3.1}$$

Most of the sources identified in our sample have star-like values of $\alpha_{3.6-8.0}$, which is to be expected given the wide area covered by the IRAC mosaic. The majority of sources with YSO-like spectral indices are class II objects, which implies a young age for the region ~ 1-3 Myr. The vast majority of sources in the field, 151, are identified as stars (class III), however. From the number density of stars in the stellar neighbourhood (0.122 stars/pc$^3$), we expect ~30 interloping foreground field stars in the *Spitzer* image, assuming a uniform distribution of stars within a 140 pc volume (given a scale height of 300 pc at the distance of the Sun from the galactic center Jurić et al., 2008). Foreground contamination does not account for all of these stars, therefore. In 2MASS observations, a stellar density of ~ $10^3$ stars per square degree is expected at 20° latitude, approximately 300 stars in an area the size of the IRAC field presented here. The number of stars in this field can therefore be comfortably accommodated by this. Any shortfall between the expected and observed number of background stars is attributed to absorption by the star formation region, instrumental artefacts (e.g. diffraction spikes) and inhomogeneities in the distribution of stars across space reducing the observed number of stars.

A comparison of the spectral indices of sources in L1551 with the wider Taurus region

Table 3.1: Table of sources detected in all four IRAC wavebands, and their YSO classification, from their spectral index.

| YSO Class | Spectral Index $\alpha_{3.6-8.0}$ | Number of Sources | Fraction (%) |
|---|---|---|---|
| I..... | $\alpha > 0.0$ | 7 | 4 |
| II..... | $\alpha < 0.0$ | 13 | 8 |
| III..... | $\alpha < -2.0$ | 151 | 88 |
| | Total: | 171 | 100 |

shows some similarity, implying that the regions are likely co-temporal (see Fig. 3.2 and Fig. 3.3. Another test of the age of the system is to compare the median separations of the PMS and MS stellar populations. Comparing the distributions of all sources in the field we find that the median separation between class I/II sources is 3.41′, whilst the median separation between class III sources is 5.62′, equivalent to 0.1 and 0.16 pc respectively at the distance of Taurus. These results are consistent with the values given in Luhman et al. (2009) for the entire Taurus region, in which a separation of 3.6′ between class I/II sources is quoted. Several of the bright YSO sources (e.g. XZ and HL Tau, L1551NE and L1551 IRS5) have been omitted from our sample due to saturation and it is expected that the median distance between YSO sources has been slightly over estimated in this analysis. The difference in separation for the PMS and MS objects in L1551 imply that the star formation is clustered as the separation of YSOs is smaller than that of field stars, and that the region very young as the PMS objects have not moved far from their initial locations and there are still some class I objects in the region (which have a lifetime ~0.7 Myr). Compared to other stellar clusters, the Taurus region as a whole is quite diffuse, with a mean (projected) separation between class I/II objects around twice that of other regions at a similar age (Gutermuth et al., 2010)

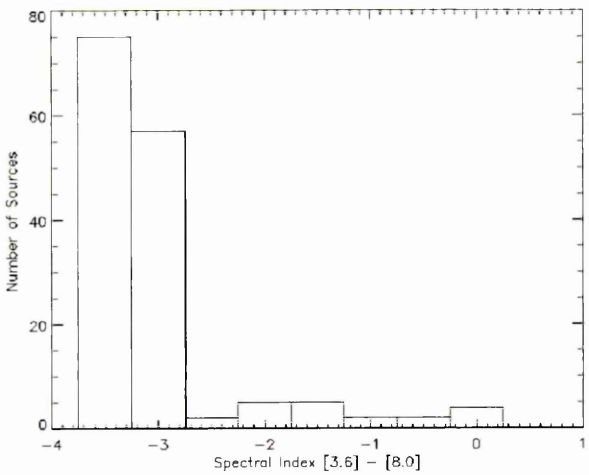


Figure 3.2: Plot of 3.6 $\mu$m - 8.0 $\mu$m spectral index for sources for sources in the L1551 region analysed here.

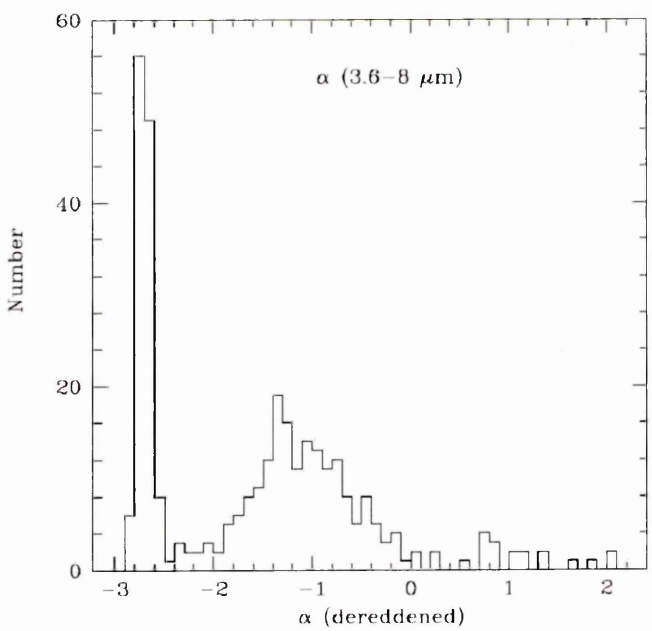


Figure 3.3: Plot of 3.6 $\mu$m - 8.0 $\mu$m spectral index for sources in the Taurus star forming region taken from Luhman et al. (2010).

To distinguish the YSO class of each source, a mid infra-red colour-colour plot was used. Class boundaries are obtained from cluster synthesis in Robitaille et al. (2006). Most of the sources are clustered around the origin, implying the source has a class III nature. The remainder of the sources are scattered towards large values of [5.8]-[8.0], which we interpret as the excess from circumstellar material only becoming apparent at the longest IRAC wavelength.

Possible contaminants to the source list of candidate YSOs we are searching for are regions of shocked emission, background giant stars and extragalactic sources. We use only the long exposure data from the HDR observations for photometry, so that we trace the extended emission in the region in relation to the position of the YSOs we identify. Correlating IRAC sources identified in all four bands with 2MASS and using the J-K, J-H and H-K colours to identify the source spectral type eliminates potential contamination from giant stars. Discrimination on the basis of $m_{5.8}$-$m_{8.0}$ colour, and $m_{8.0}$ brightness (see Harvey et al., 2007) with a colour-magnitude diagram eliminates background galaxies, which would appear as faint and red.

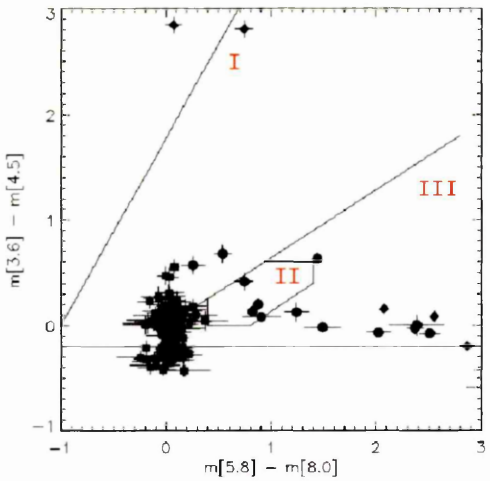


Figure 3.4: IRAC Colour-Colour Diagram for determining the class of YSO. The lines delineate the regions of the plot where particular YSO classes are most likely to be found. In the above diagram, Class I sources are plotted as diamonds, Class II as circles and Class III as squares.

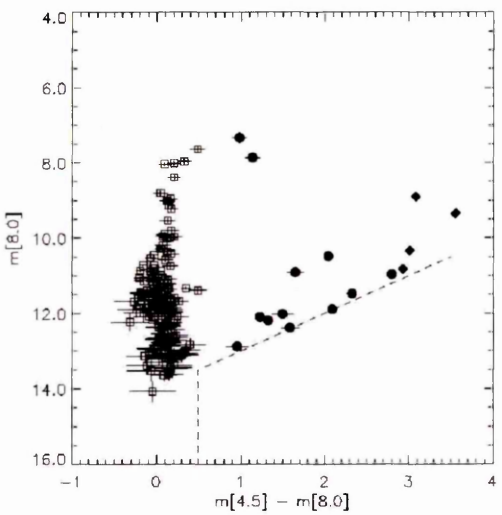


Figure 3.5: IRAC Colour-Magnitude Diagram. The YSO class of each source (I – III, from the spectral index) is identified by a diamond, circle or square, respectively. Filled symbols denote YSO candidate sources. The dashed line marks the region of the diagram within which extragalactic sources should be found. None of the sources in this survey are consistent with extragalactic origin.

Table 3.2: Summary of infrared excess sources, their positions and IRAC colours. Sources that have been identified in previous surveys of the region are named.

| Source ID | Right Ascension (J2000) | Declination (J2000) | $m_{3.6}$ [mags] | $m_{8.0}$ [mags] | $m_{3.6}$-$m_{4.5}$ [mags] | $m_{5.8}$-$m_{8.0}$ [mags] | Notes |
|---|---|---|---|---|---|---|---|
| 1 | $4^h32^m31.20^s$ | $18^d14^m10.1^s$ | 13.95 | 12.38 | 1.49 | -0.016 | |
| 2 | $4^h32^h29.46^h$ | $18^d14^m00.2^s$ | 12.69 | 10.91 | 1.24 | 0.13 | [GBA2007] 1441 |
| 3 | $4^h32^m34.01^s$ | $18^d01^m14.2^s$ | 13.68 | 10.96 | 2.51 | -0.074 | Extended |
| 4 | $4^h32^m16.07^s$ | $18^d12^m46.4^s$ | 9.41 | 7.86 | 0.74 | 0.42 | [GOK2004] 96 |
| 5 | $4^h32^m10.30^s$ | $18^d23^m41.4^s$ | 12.47 | 9.33 | 3.15 | -0.43 | |
| 6 | $4^h32^m17.12^s$ | $18^d04^m15.1^s$ | 12.37 | 9.36 | 3.05 | -0.59 | |
| 7 | $4^h31^m59.68^s$ | $18^d21^m30.5^s$ | 9.00 | 7.33 | 0.54 | 0.68 | |
| 8 | $4^h32^m01.57^s$ | $18^d15^m23.0^s$ | 13.52 | 12.09 | 0.88 | 0.20 | |
| 9 | $4^h32^m01.25^s$ | $18^d05^m01.2^s$ | 13.92 | 10.83 | 2.08 | 0.16 | [GOK2004] 85 |
| 10 | $4^h31^m49.97^s$ | $18^d19^m15.1^s$ | 13.92 | 11.89 | 2.02 | -0.07 | |
| 11 | $4^h31^m46.57^s$ | $18^d19^m10.7^s$ | 13.91 | 12.88 | 0.91 | 0.08 | |
| 12 | $4^h31^m37.5^s$ | $18^d12^m25^s$ | 12.45 | 11.39 | 0.26 | 0.57 | HH 30 |
| 13 | $4^h31^m36.62^s$ | $18^d01^m28.8^s$ | 13.43 | 10.34 | 2.55 | 0.09 | |
| 14 | $4^h31^m08.9^s$ | $18^d01^m43^s$ | 11.78 | 8.90 | 2.87 | -0.20 | [GOK2004] 27 |
| 15 | $4^h30^m58.84^s$ | $18^d22^m26.5^s$ | 13.52 | 12.02 | 2.39 | 0.01 | |
| 16 | $4^h30^m58.2^s$ | $18^d03^m29^s$ | 13.16 | 10.48 | 1.44 | 0.64 | [GOK2004] 13 |
| 17 | $4^h30^m54.39^s$ | $18^d12^m14.7^s$ | 13.78 | 11.48 | 2.37 | -0.03 | |
| 18 | $4^h30^m53.8^s$ | $17^d59^m09^s$ | 13.64 | 12.19 | 0.82 | 0.13 | [GOK2004] 10 |

### 3.3.2 Comparison with Gålfalk et al., 2004

The ISOCAM survey identified 14 candidate YSO sources in L1551, of which two were previously identified (HH 30 and MHO 5, their sources ISO-L1551-61 and -96). The overlap between the IRAC and ISOCAM fields is almost complete, and we identify 12 of their sources in the IRAC data, but ISO-L1551-2 and -3 are outside of the IRAC field and no analysis could be made on those sources.

ISO-L1551-13 is located within a knot of shocked emission in the IRAC images, perhaps leading to it being identified as extended in the ISOCAM survey.

ISO-L1551-19 is seen to consist of two components in a patch of bright emission in the IRAC images. Only the western component is visible in all four IRAC images. Both components are very faint in the 5.8 $\mu$m image.

ISO-L1551-74 is two sources with some extended emission lying between them in the IRAC images except for 8.0 $\mu$m, in which it appears as a single extended source.

ISO-L1551-85 is resolved as two components of which only the brighter, southern, component is visible in all four IRAC images.

ISO-L1551-86, noted as lying close to HH 262, is not coincident with a point source in the IRAC data, instead being associated with a bright patch of nebulous emission.

### 3.3.3 Comparison with Luhmann et al., 2009

The most recently published study of the Taurus star-forming region, Luhman et al. (2009), used both *Spitzer* IRAC 3.6–8.0 $\mu$m and MIPS 24 $\mu$m observations to determine the YSO population of the region and it's evolutionary state, compared to the more limited IRAC-only based analysis presented here. The additional MIPS data enables the detection of cooler dust excesses, extending the effective range of disc masses and ages which could be sampled.

In their analysis, a total of 28 sources are identified as members in the L1551 region, of which 10 have a 3.6–8.0 $\mu$m spectral index indicative of infrared excess. Of the remainder, 4 have no spectral index due to saturation of the source at one or both of the wavelengths. There

is good agreement between the spectral indices of their work and the one presented here (see their Table 7, Luhman et al., 2009). The number of YSO sources identified in this work is twice that of Luhman et al. (2009), although the relative ratio of class I to class II objects is the same in both. We attribute the larger number of sources identified in this work as a vindication of our use of only the long exposure data from the HDR observations of the L1551 dark nebula, reducing the sky noise in the combined mosaics of the region.

## 3.4 Conclusions

We have combined *Spitzer* IRAC and 2MASS observations of the L1551 star forming region to search for faint YSOs. We detected 193 sources with fluxes in all four IRAC bands, of which 169 had counterparts in the 2MASS data. Using colour-magnitude and colour-colour diagrams, we have determined the YSO class for the 169 sources. Eighteen of the sources have both spectral indices and positions in colour-magnitude/colour-colour plots consistent with infrared excess. Of these, twelve have not been previously identified as YSO candidates in the literature.

We find evidence that the PMS sources in L1551 are more closely associated than the stellar sources (class I/II vs class III), with comparable median separation of the nearest neighbour in both the case of PMS vs star and star vs star separation to that of Luhman et al. (2010). This implies that the star formation in this region occurred in cluster rather than isolation, as the objects are too young (1–3 Myr) to have moved far from their initial point of formation. We also find that the distribution of sources by spectral index in L1551 is consistent with the wider Taurus region.

# 4

# Debris Discs in the AKARI FIS All Sky Survey

## 4.1 Introduction

The work presented in this Chapter was started during a two month visit to ISAS in Japan, made at the end of my first year. During the visit I was embedded within the AKARI FIS Vega Disks team, working on the initial reduction of the FIS All Sky Survey data. As part of my contribution to the Vega Disks team, I worked on the correlation of FIS counterparts to red IRC sources from the 9/18 $\mu$m All Sky Survey and debugging of the data reduction pipeline (e.g. pointing offsets, flux calibration and source (mis)identification). The visit gave me the opportunity to gain hands-on experience with the pipeline and experience working in a scientific environment different to my home institution. Due to the fluid state of both the instrument calibration and data reduction at the time of my visit, much of the work that is presented here was carried out at the OU over the subsequent two years.

### 4.1.1 AKARI

AKARI (Murakami et al., 2007) is an infrared survey satellite launched by the Japanese Aerospace eXploration Agency (JAXA) at the beginning of 2006. It is operated by the Japanese with assistance from the European Space Agency (ESA) and the UK led consortium with the Netherlands[1]. The primary goal of the mission was the survey of the entire sky in six wavebands from 9 - 160 $\mu$m at higher sensitivity, superior resolution and over a broader wavelength range than the previous survey by *IRAS*. AKARI carries two instruments, the Infrared Camera (IRC, Onaka et al., 2007) operating at mid-infrared wavelengths between 2 – 24 $\mu$m, and the Far infrared Surveyor (FIS, Kawada et al., 2007) operating between 50 – 180 $\mu$m. This phase of the AKARI mission was complete as of September 2007, due to the evaporation of all helium coolant from the telescope bringing cryogenic operations to an end. During its cryogenic operational period, the FIS observed over 94% of the sky at least twice in four wavebands from 65 to 180 $\mu$m. The wavebands were calibrated to 65 $\mu$m and 90 $\mu$m (N60 and WIDE-S) for the SW bands and 140 $\mu$m and 160 $\mu$m (WIDE-L and N160) for the LW bands. AKARI also took pointed observations of particular targets with greater sensitivity than that of the all sky survey, some of which are presented in Chapter 6.

### 4.1.2 Telescope

AKARI is equipped with a 68.5 cm aperture f/6 Richty-Chrétien telescope. The optics and detectors of the telescope are held in a cryostat which is thermally isolated from the rest of the satellite. The cryostat is cooled by liquid He (179 *l* on launch) evaporation and two sets of Stirling-cycle mechanical coolers. The telescope and IRC are kept at a temperature of 5.8 K, whilst the FIS is cooled to 2.0 K. The telescope mirrors are constructed from Silicon Carbide, a rigid and lightweight material. The focal plane of the telescope is shared between the two instruments (IRC and FIS) and the star trackers (see Fig. 4.2(a)).

[1]Consisting of: The Open University, Imperial College (University of London), University of Sussex (UK) and SRON-Groningen with University of Groningen (NL).

The satellite was launched into a 700 km high orbit above the day-night terminator with an orbital period of 100 min. The orbit, similar to that of *IRAS*, was chosen as that best suited to all sky observation whilst avoiding both the Earth and the Sun. Initial operations (and removal of the telescope shield) were delayed for a month as the Sun tracking sensors on the telescope did not work, though the total lifetime for cryogenic observations was not adversely affected as the He evaporation rate was found to be lower than predicted.

### 4.1.3 Far Infrared All Sky Survey

For the all sky survey observations, the telescope was continuously scanned across the sky at a rate of $3.6\,'s^{-1}$. Upon completion of FIS observations, over 94% of the sky had been observed in two separate pointings. Some regions of the sky had been missed due to scattered light from the Moon or interference passing through the South Atlantic Anomaly.

The FIS instrument's primary mission was the completion of a new all sky infrared survey. In this it has been phenomenally successful, observing over 250,000 sources at 90 $\mu$m (see Fig. 4.1), contained within the publicly available Bright Source Catalogue (BSC). The $5\sigma$ noise levels of the AKARI all sky survey offer a vast improvement over the *IRAS* survey at mid infrared wavelengths. In the far infrared, only the WIDE-S (90 $\mu$m) band is more sensitive than *IRAS* and the N60 (65 $\mu$m) band is distinctly poorer than *IRAS* (see Table 4.2). There are several contributing factors to the poor performance of AKARI in the far infrared. The telescope aperture of 67cm is smaller than the design specification due to a defect being introduced into the original primary mirror after the failure of a support strut during vibrational testing creating a chip at the mirror's edge. The level of electronic noise in the FIS instrument was twice the level expected. The FIS detector temperature at 90$\mu$m was lower than optimal, reducing the efficiency of the detector surface (White G.J., priv. comm.). The benefit of the AKARI FIS survey is therefore in the extended wavelength range and better source discrimination in regions with bright cirrus or galactic background contamination.

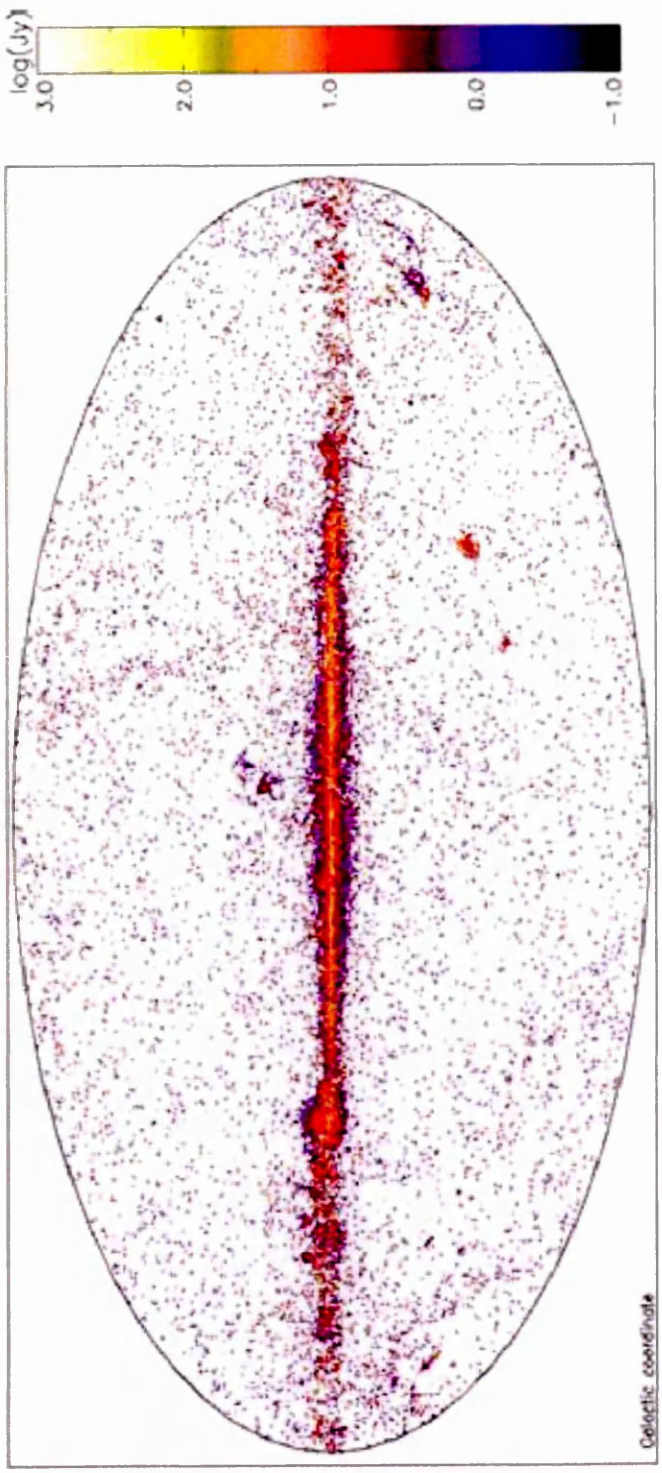


Figure 4.1: Illustration of the sky distribution of sources in the AKARI FIS BSC. The sky is displayed in galactic coordinates, with the galactic centre in the middle of the image. Taken from Verdugo et al. (2007).

### 4.1.4 Detectors

The FIS was equipped with two separate detector arrays for the SW and LW bands, offset from the telescope's optical axis. For the SW bands, the detector surface was made from two monolithic Ge:Ga arrays cooled to 2.2 K, whilst in the LW bands the detectors were two stressed Ge:Ga arrays cooled to 2.0 K. The dimensions of the detector arrays were 15×2 pixels for N60, 15×3 for WIDE-S, 20×3 for WIDE-L and 20×2 for N160. The arrays were orientated at an angle of 26.5° with respect to the scan direction (see Fig. 4.3(a)). Pixel sizes were 26.8″ for the SW bands and 44.2″ for the LW bands (Kawada et al., 2007).

Detector readout was performed by a Capacitive Trans-Impedance Amplifier (CTIA). Infrared photons incident on the detector induced a charge on the capacitor, which was read out (reset) at regular intervals. The frequency of detector resets was increased in regions of high sky brightness (e.g. the galactic plane) to avoid saturation. The signal detected between two resets is defined as a ramp. To calculate the flux from the source, the gradient of the signal is calculated (this is described in more detail in the next subsection).

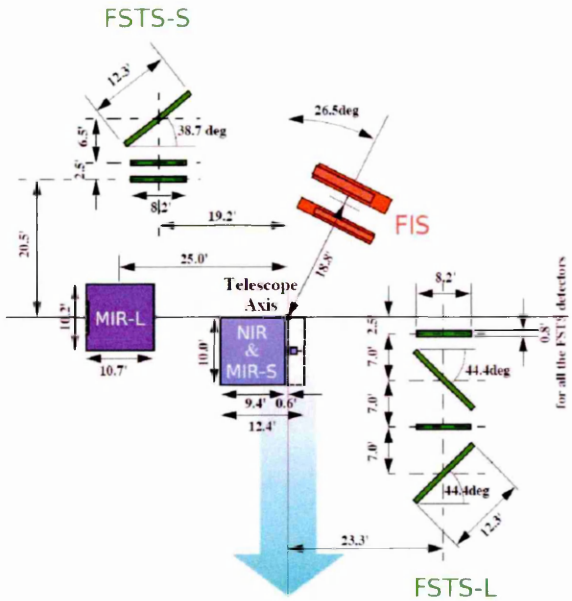


Figure 4.2: Layout of the AKARI focal plane, including the two star trackers (FSTS-S and FSTS-L). The on-sky scan direction is indicated by the large blue arrow. Taken from Verdugo et al. (2007).

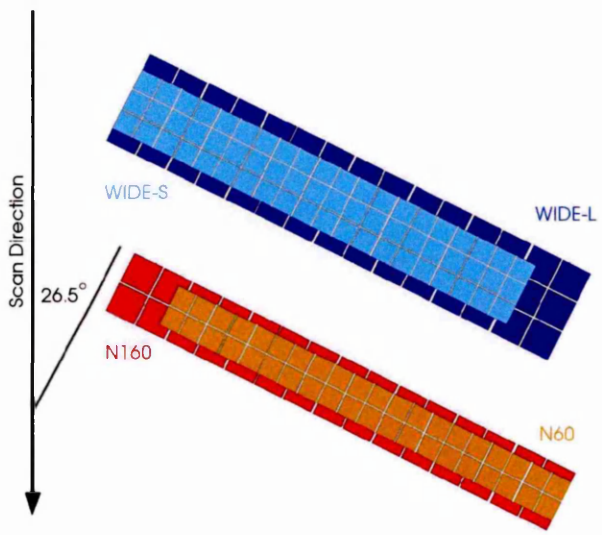


Figure 4.3: Schematic representation of the FIS detectors. Taken from Verdugo et al. (2007).

### 4.1.5 Data Processing

Data reduction of the all sky survey observations were carried out with the participation of several European institutions, collectively referred to as the IOSG consortium. All sky survey data was reduced and calibrated using a purpose built pipeline, the 'green box' (see Fig. 4.5). A brief summary of the major stages follows:

The time series data (TSD) are obtained from the local data server (LDS). Sections of the raw TSD are flagged if the associated pixels are identified as 'bad' i.e. saturated/hot or dead pixels by the pipeline, or the pixel is too close to the moon, and may suffer from elevated background levels due to scattered light.

The TSD units are then converted from the instrument output ADU signal to Volts and a correction is applied to the ramp signal due to the non-linear response of the electronics.

The TSD are then analysed for cosmic ray hits (glitches) which are distinguished from real source events by the short time over which the detector signal changes compared to real sources (0.1 s for a glitch cf. ~1 s for real sources). The sections of the TSD associated with glitches are flagged as unreliable by the pipeline and not used in subsequent image reconstruction. If multiple glitches are detected within a single ramp (between resets) the ramp is split into subsections and each is analysed separately.

The signal current then is calculated from the gradient of the ramp, which is fitted with a linear function. If there are several subsections to be analysed, these are handled separately, and the mean signal current for the ramp calculated from the weighted average of the subsections.

The dark current, estimated from the sections of the TSD that are taken with the shutter closed, is subtracted from the signal. A flat field correction applied based on the response of the detector to 120 s exposure to the calibration lamp.

The main contribution to the background in AKARI images is Earth-shine scattered into the detector from the telescope baffle. This is removed by median filtering of the TSD.

In order to produce an image from the TSD scan data, the position of each pixel in the detector is calculated, accounting for the offset from the optical axis (bore-sight) and any dis-

tortion in the detector. An image plane matching the size of the sky region sampled by the scan strip in the TSD is formed and filled using the contributions of each instrument pixel to the corresponding position on the plane, summing the contribution from the data points and averaging over the number of data points per pixel.

Lastly, the image flux units are converted from V $s^{-1}$ to MJy $sr^{-1}$, calculated as a conversion factor derived from the detector signal observed when the calibration lamp is active. The output .fits image from the pipeline can now be analysed using standard packages, and aperture photometry will return source fluxes in Janskys (subject to aperture, colour and systematic correction, see Chapter 2 for details).

The source extraction process was handled by a separate routine (SUSSEXtractor, SXT) that will be described in a later section. The SXT program includes the full pipeline processing detailed above and allowed the user to select regions of the sky for analysis and query particular source positions for photometry.

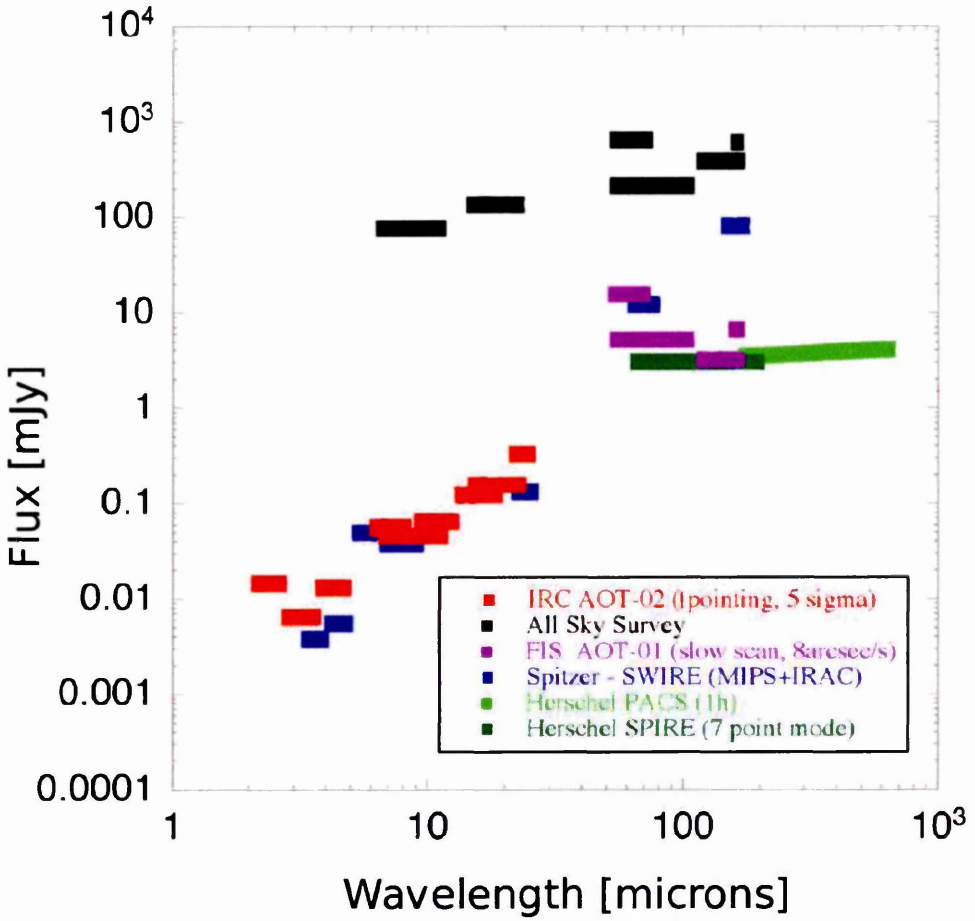


Figure 4.4: AKARI $5\sigma$ sensitivities compared to similar infrared observatories, including *Spitzer* and HERSCHEL. Taken from Verdugo et al. (2007).

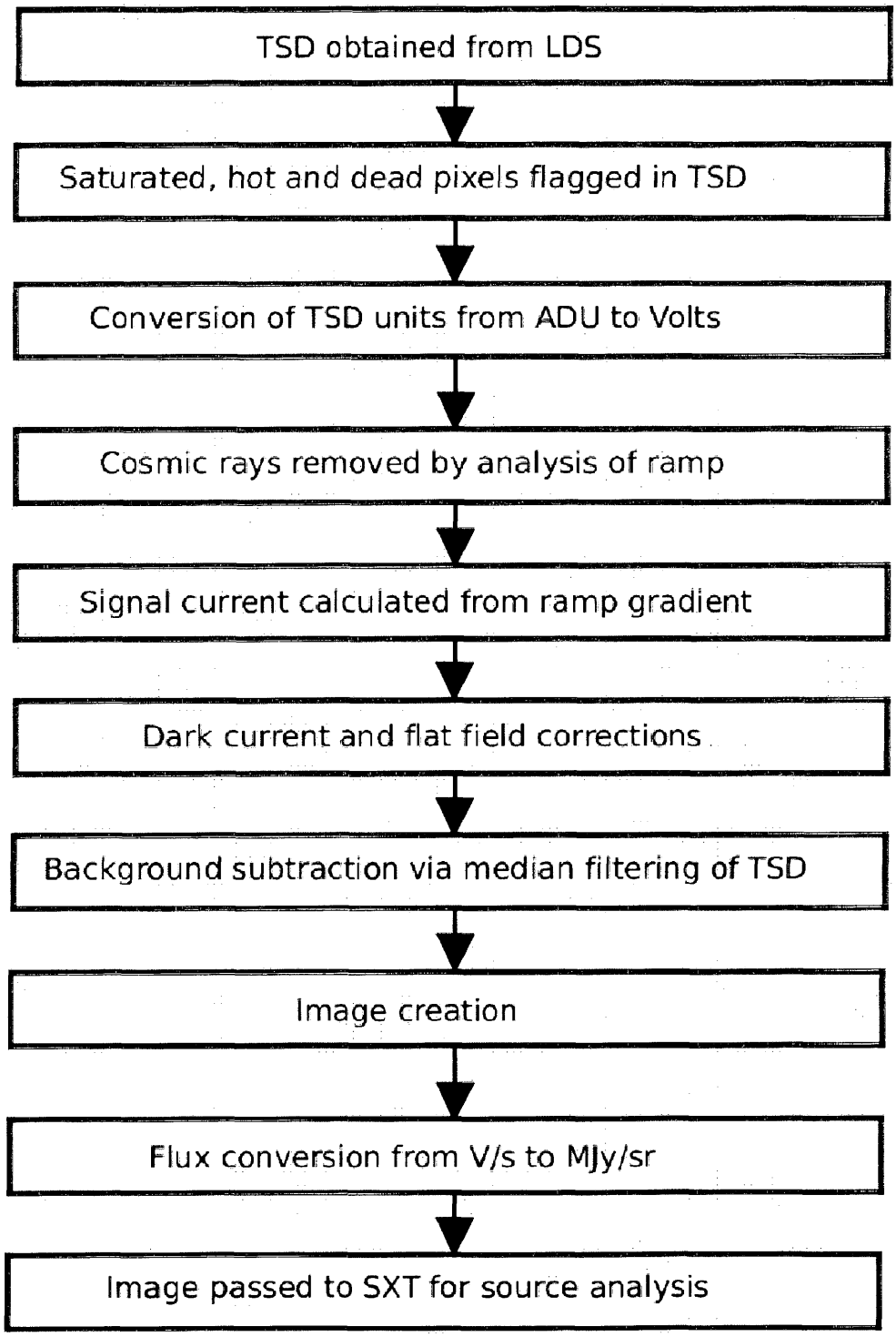


Figure 4.5: A schematic representation of the major stages of data processing undertaken by the 'green box' pipeline.

## 4.2 Studies of FIS Data

I performed two separate studies using the FIS survey data. The first, working directly with the data, was based on a sample of ~13,000 targets that I had identified as previously known, or likely candidates for, debris disc stars. The second was a simple cross correlation of the SAO and HD catalogues with the AKARI FIS BSC, produced by the FIS data analysis team.

### 4.2.1 Targeted Search

#### 4.2.1.1 Target Selection

A list of candidate stars was compiled to search for debris discs in a more focused manner than simply searching the Tycho-2 catalogue. The main objective of this list was to provide a statistically valid sample of stars that would produce the greatest detection rate of new debris discs from those observed in the all sky survey.

The bulk of the list was compiled from ten separate sources; the DARWIN and TPF preliminary target lists; the SIM (Space Interferometer Mission) Tier 1 target stars; the California & Carnegie Planet Search list with planetary mass companions; 120 M dwarfs from the Catalogue of Nearby Stars 3 (CNS3); the Mayor-Queloz sample of > 320 stars; the CORALIE sample of > 1650 stars; all G dwarfs from 10–15 pc in the Appalachian Survey; the RECONS list of nearby stars; the Lindroos catalogue of binaries with a low mass companion and the Geneva catalogue of 164 stars with companion objects of $m\sin(i) < 18M_{jup}$.

This raw list of over 15,000 sources was then trimmed to remove any duplicates from the component target lists and then correlated against the *Spitzer* reserved observations catalogue[1] (ROC) in order to remove targets that had been observed in the mid infrared at superior sensitivity to that of AKARI. After this filtering process some 10,000 candidate stars remained.

In order to guarantee that the source list was as unbiased as possible, all dwarf stars of spectral type A0–M7 from the NStEDs catalogue within 100 pc were added to the reduced

[1] ssc.spitzer.caltech.edu/ROC/

target list to ensure complete coverage of nearby stars in the sample. The spectral type was cut off at M7 to avoid contamination of the sample with brown dwarfs. The distance requirement was a function of the expected limit of detection for a $\beta$ Pictoris type dust disc at 90 $\mu$m (WIDE-S) assuming sensitivities from the all sky survey (200 mJy 5-$\sigma$ sensitivity, $F_{\beta Pic} \sim 9$ Jy at 19.3 pc, so at 100pc, $F_{\beta Pic} \sim 330$ mJy). No sources were excluded from the list based on sky position, presence of a binary companion, variability or whether it was previously identified as having excess emission in the mid infrared.

Finally, targets not already included in the list were added from two specific target lists; the 500 stars of the SCUBA-2 Unbiased Nearby Stars Survey (SUNSS, Matthews et al., 2007), a legacy program for the JCMT's new SCUBA-2 instrument, and the Royal Observatory Edinburgh's Debris Disc Database (ROE DDD[1]), which is a complete list of known debris discs (mostly *IRAS* discovered) before 2001.

In the final list of sources there are 12,760 stars, comprising those in Table 4.2.1.1:

Table 4.1: AKARI Debris Disc Candidate Stars A – M by Spectral Type

| Spectral Type | Number |
|---|---|
| A | 742 |
| F | 3942 |
| G | 4961 |
| K | 2383 |
| M | 732 |

Combining these numbers with the detection rates quoted in Chapter 1, we might expect the detection of several hundred debris discs. Several factors act to reduce the detection rate, however. The in-orbit sensitivity of the FIS instrument was lower than that expected from the bench tests, with a 5$\sigma$ limit of 550 mJy at 90 $\mu$m, reducing the effective range of the instrument to detect faint dust emission by a factor of $\sim$ 4. The AKARI 65 $\mu$m band is a lot less sensitive than the *IRAS* 60 $\mu$m band (5-$\sigma$ sensitivities of 2.4 and 0.4 Jy, respectively) in which most of the cold debris discs were detected. The AKARI FIS does however have an improved beam

[1] www.roe.ac.uk/ukatc/research/topics/dust/identification.html

Table 4.2: Table comparing the relative beam size, sensitivity and resolution of AKARI (Murakami et al., 2007) and *IRAS* (Neugebauer et al., 1984).

| | AKARI | | *IRAS* | |
|---|---|---|---|---|
| | 65 $\mu$m | 90 $\mu$m | 60 $\mu$m | 100 $\mu$m |
| Beam FWHM [″] | 37 | 39 | 60 | 120 |
| Scan speed [′/sec] | 3.6 | | 3.85 | |
| Resolution[″/pixel] | 30 | 30 | 60 | 120 |
| Wavelength Range [$\mu$m] | 50–80 | 60–110 | 40–80 | 83–120 |
| Bandwidth [$\mu$m] | 21.7 | 37.9 | 32.5 | 31.5 |
| Sensitivity Limit [Jy] | 2.40 | 0.55 | 0.5 | 1.5 |

FWHM and higher resolution compared to *IRAS* (see Table 4.2). The benefit of this is the reduction in contamination from the background or multiple sources in bright or dense regions, with the drawback of a reduced sensitivity towards extended emission. The FIS SW wavebands are narrower than their *IRAS* 60 and 100 $\mu$m counterparts. This reduced the contamination of the measured far infrared excess flux with shorter wavelength photospheric emission, but also reduces the total flux observed in a given waveband. There is no reason why the uncorrected flux for a given object should be the same in AKARI and *IRAS*, but the narrower AKARI bandwidth reduces the probability of detection of debris discs that peak at wavelengths shorter than 90 $\mu$m. The combination of these factors made it certain that some of the *IRAS* discovered debris discs would be missed by AKARI.

#### 4.2.1.2 Data Reduction & Calibration

Time Series Data (TSD) files were downloaded from the Local Data Server (LDS) for each target covering a box region of 12′ around the expected position (IRCS J2000 coordinates) of each target. The TSD files were processed by the AKARI FIS pipeline (Savage & Oliver, 2007), developed by Richard Savage and Nurur Rahman of Sussex University (see previous section for details). Outputs from the pipeline comprised four images, one for each of the wavebands, and a list of sources identified in each field including their positions, observed brightness and an estimate of the background. The images were created using the standard 8″

Table 4.3: Table of Aperture and Absolute Corrections for AKARI FIS Photometry, taken from the FIS Data Users Manual v1.3.

| | | | Correction | |
|---|---|---|---|---|
| Waveband | Wavelength [$\mu$m] | Aperture ['] | Aperture | Absolute |
| N60 | 65 | 0.625 | 1.58 | 1.7 |
| WIDE-S | 90 | 0.625 | 1.74 | 1.7 |
| WIDE-L | 140 | 0.750 | 1.71 | 1.9 |
| N160 | 160 | 0.750 | 2.03 | 3.8 |

per pixel image scale for the SW bands, and 15″ per pixel for the LW bands. The source log-evidence threshold within each image was 10, equivalent to a signal-to-noise ratio of 4.5 above the local background. The observed source brightness values, $S$, were converted to fluxes, $F_\nu$, in Janskys by the following waveband dependent corrections (from the FIS data manual v1.3[1], Verdugo et al., 2007):

$$F_{N60} = \frac{S}{0.35477 + 0.11616 \log_{10}(S)} \tag{4.1}$$

$$F_{WIDE-S} = \frac{S}{1.41220 + 0.55729 \log_{10}(S)} \tag{4.2}$$

$$F_{WIDE-L} = \frac{S}{6.44215} \tag{4.3}$$

$$F_{N160} = \frac{S}{9.79258} \tag{4.4}$$

Appropriate aperture and absolute calibration corrections for each waveband were applied to the converted fluxes, also taken from the FIS Manual, using the aperture sizes from the table. In Table 4.3, the aperture flux correction ($K_{ap}$) is multiplicative and the absolute correction ($K_{ab}$) is divisive, such that the corrected flux $F_{corr} = F_{obs} \times (K_{ap}/K_{ab})$.

Source positions were correlated between the expected target location (image centre) and the observed sources in the field of view (see Fig. 4.6). A maximum correlation radius of 40″, equivalent to a displacement of up to 5 pixels from the image centre, was derived from

[1] www.ir.isas.jaxa.jp/ASTRO-F/Observation/IDUM/

the scatter of target location from expected position of known, bright *IRAS* debris discs in the sample. There was no observed correlation between source brightness and separation from the image centre, nor was any preferential direction observed in the scatter of the sources. A visual inspection of the WIDE-S images of those targets with a source within the rejection radius was then carried out, removing those targets from the final list that had non-stellar shapes, or were positioned close by bright glitches or artifacts in the field. All targets with an observed infrared excess were detected at 90 $\mu$m, but only the brightest were detected in either 65 $\mu$m or 140 $\mu$m. None of the debris discs in the sample were detected at 160 $\mu$m.

### 4.2.2 Cross Correlation

#### 4.2.2.1 Target Selection

The public release of the AKARI FIS BSC was cross correlated with both the Tycho-2 (Høg et al., 2000) (for all sky coverage and faint stars) and HD (Cannon & Pickering, 1993) catalogues (for bright stars). The sources selected by the AKARI data analysis team for inclusion in the BSC catalogue were all detected at 90 $\mu$m with SNR > 5. Where possible, additional fluxes, or upper limits, from the other three FIS bands are included, but the sources in the remaining three FIS bands are a subset of the 90 $\mu$m set. To avoid high background, crowded regions and the part of the all sky survey observed with the CDS (Correlated Double Sampling, rather than Normal) mode, for which faint sources (flux < 1 Jy), are not as well calibrated, sources within ±20° of the galactic plane were removed from the sample.

#### 4.2.2.2 Pointing Accuracy

A major issue with the previous *IRAS* all sky survey was the interplay between the low resolution (large pixel size) and broad PSF. These two limitations reduced the discrimination between sources and bright background regions (e.g. close to the galactic plane) in the survey and meant that (from the large beam size) significant contributions could be made to the observed flux at a stellar position which was in fact due to the presence of a background galaxy in the beam (e.g.

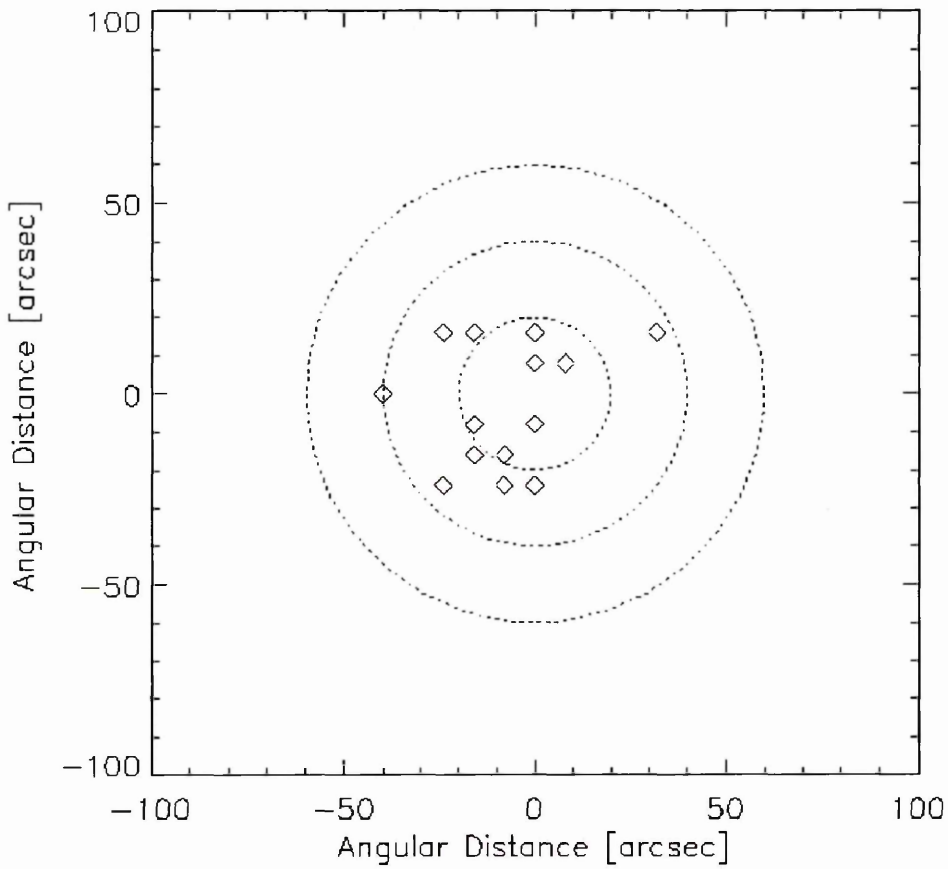


Figure 4.6: Plot of the scatter in observed position of known debris discs detected by AKARI around the image centre of the 90 $\mu$m image. Dotted circles represent radii of 20, 40 and 60″, respectively. The positions presented here are based on the preliminary, in-orbit AOCS (Attitude and Orbital Control System) pointing calibration rather than the more accurate, ESA derived, GADS (Ground-based Attitude Determination System) pointing due to the uneven state of the data reduction in the LDS at the time of analysis.

55 Cnc, Jayawardhana et al., 2002).

To avoid the incorrect association of an infrared excess with the presence of a debris disc, the position accuracy of the AKARI all sky survey was evaluated. The positions of 250,000 stars in the SAO stellar catalogue (SAO Staff, 1995) were cross correlated with the AKARI FIS BSC catalogue. Taking a distance of 20″ as the maximum radius for two sources in each catalogue to be positionally associated (derived from the analysis of the position scatter in my targeted search), a total of 1,391 matches were found. The distribution of these positions is offset around the SAO coordinates, by 1″ in Right Ascension and 1.42″ in Declination (see Fig. 4.7). This offset, although small, is significant and has been observed across the entire sky with similar magnitude in a variety of populations (e.g. stars, emission line galaxies and radio sources all show a similar offset).

Although the offset in the AKARI catalogue positions is real, the consistency in this shift across different object types (radio sources, infrared luminous galaxies and stars) allows the observed AKARI positions to be trusted to within 2″. Fitting the source distribution fall-off as a function of radius, more than 99.9% of sources lie within 10″ of the expect position. This is equivalent to about the width of one pixel in the all sky survey images.

### 4.2.3 Contamination

The AKARI all sky survey covered 94% of the sky, with 290,000 sources in the BSC. Most of these sources are expected to be galaxies. Not all regions of the sky were covered to equal depth (e.g. the ecliptic poles were observed much more frequently). The probability that a false-positive correlation could be made between a star and a galaxy that lies along the same line of sight is therefore estimated from the density of far infrared sources in the field, using the prescription from Condon et al. (1998) (their Eqn. 4).

$$P(< r) = 1 - e^{-\pi\rho r^2} \tag{4.5}$$

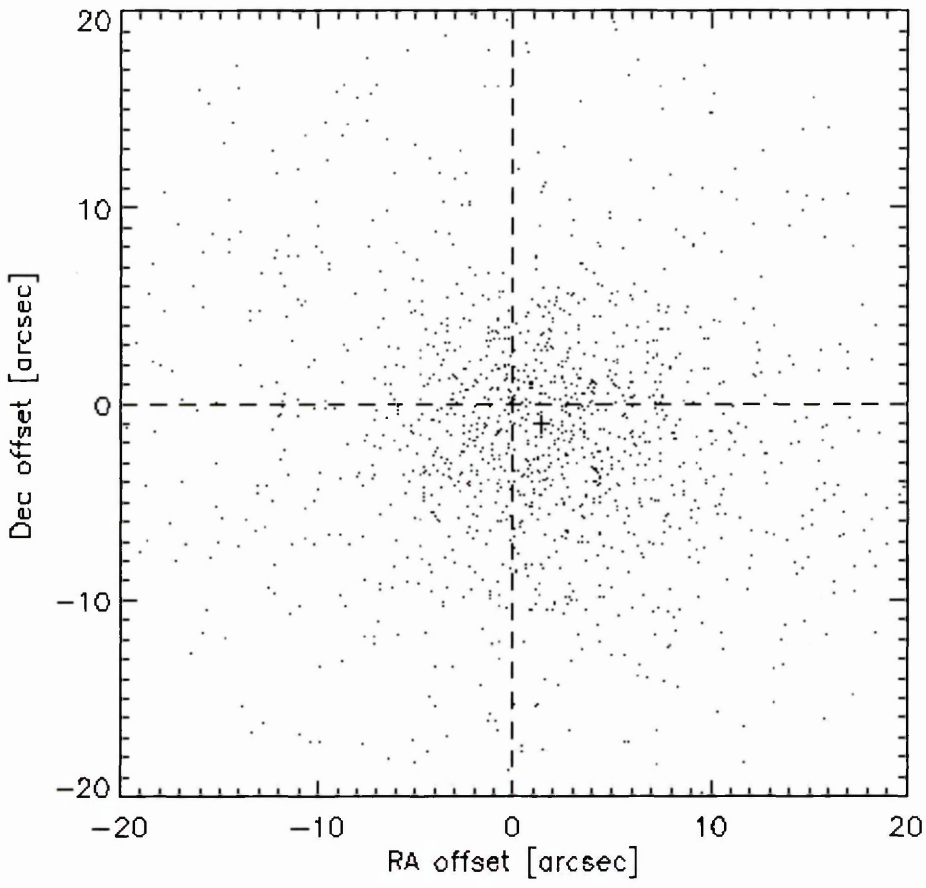


Figure 4.7: The scatter in the AKARI positions of 1,391 objects around the expected SAO coordinates. The centroid of the AKARI positions is offset from the SAO positions (by 1.4″ in RA and 1.0″ in Dec) and is denoted by a + symbol.

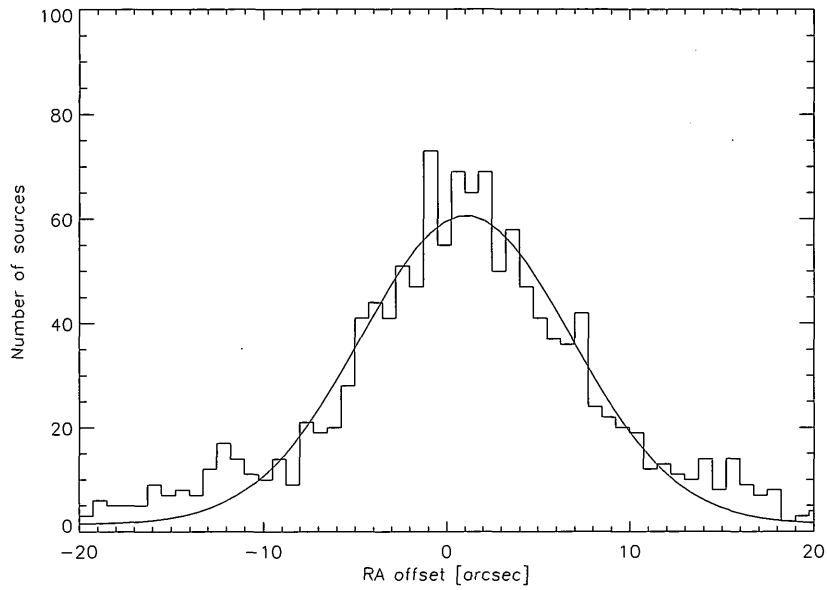


Figure 4.8: Histogram of the offset in Right Ascension between 1,391 sources correlated between the AKARI FIS BSC catalogue and the SAO star catalogue. The histogram has been fitted with a Gaussian curve (peak centre -1.4″, FWHM 9″).

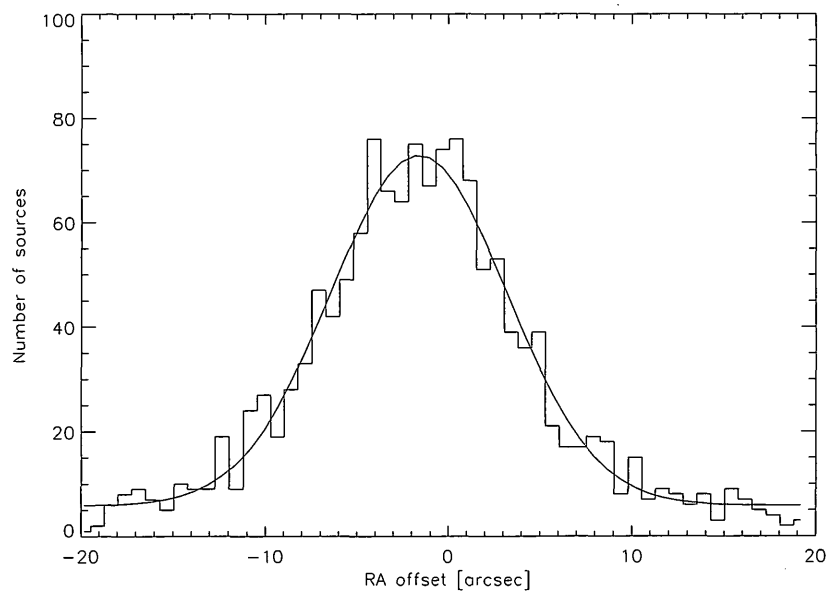


Figure 4.9: Histogram of the offset in Declination between 1,391 sources correlated between the AKARI FIS BSC catalogue and the SAO star catalogue. The histogram has been fitted with a Gaussian curve (peak centre 1.0″, FWHM 11″).

In the above equation, the probability $P$ that a source within a distance $r$ of an optical counterpart is a false positive is a function of the source density $\rho$ and the critical radius, $r$. For the FIS all sky survey, the number density of sources is sources per square degree is 7.05. For critical radii of 2, 5 and 10″, the probabilities of a false positive are therefore estimated as $6\times10^{-6}$, $4\times10^{-5}$ and $1.7\times10^{-4}$, respectively. We therefore conclude that sources found within 10″ of the stellar position are associated with the target.

In the targeted search, we used a correlation radius of 40″, due to the observed scatter in position of known, bright debris discs. Using the same method as for the correlated sample, we see that the chance alignment of a debris disc star with an unassociated far infrared source is 0.1% in the targeted search by position alone. Combining this probability with the density distribution of far infrared sources with fluxes bright enough to be detectable by AKARI at 90 $\mu$m, approximately 1 per square arcminute, reduces the chance of contamination of the sample through coincidental alignment to $< 10^{-3}$).

## 4.3 Disc Modelling

The stellar photosphere of each target was estimated by least squares fitting of a Castelli-Kurucz (Castelli & Kurucz, 2004) stellar atmosphere model with appropriate $T_{eff}$ and log($g$) values to the optical and near infrared fluxes. The accuracy of the determination of the stellar spectral type was limited by the Tycho $B$ and $V$ magnitudes which had uncertainties that for early (A and F) spectral types were ~ the difference between the magnitudes, allowing an equally good fit for slightly falling or flat B-V colours. Discrimination between best-fit models was therefore weighted in favour of the near infrared fluxes. The colours used in the best-fit process were taken from Bessell & Brett (1988), with a linear interpolation between the colours for the missing spectral types. The photospheric emission was extrapolated to far infrared wavelengths from the 2MASS $K_s$ band flux.

The infrared excess of each target was treated in one of two ways, depending on the amount

of ancillary data available. Targets that were only observed in the AKARI WIDE-S band and had no ancillary data, were fitted with a modified black body peaking at 90 $\mu$m (equivalent to a temperature of 33 K) in order to calculate the disc maximum fractional luminosity. For these targets, the mass of the disc was calculated assuming the disc was composed of single temperature 10 $\mu$m radius dust grains with a density of 2.5 g cm$^{-3}$. For targets with AKARI and *IRAS* (or other, e.g. sub-mm observations), the disc SED was fitted to the peak flux (usually *IRAS* 60) using a two component modified black body model to match both the inner, warm dust and outer, cold dust contributions. The disc mass was then calculated assuming that the dust emission was produced by a disc of 10 $\mu$m grains with a density of 2.5 g cm$^{-3}$, as before. In both cases, the disc fractional luminosity and mass were calculated as per the equations in Chapter 2.

## 4.4 Results

### 4.4.1 Targeted Search

A total of 105 sources in the FIS all sky survey data were found within 40″ of the expected stellar position. These candidate objects were scrutinised visually to remove those which were caused by glitches (e.g. lamp reset or cosmic ray strikes) or bright cirrus emission. Sources were also removed from the list of candidates that had a fractional luminosity greater than $10^{-3}$, or a significance value ($\chi_{90}$) of less than 2. It is noted that the limit on the significance value is arbitrary, but based on the values obtained for sources associated near known debris discs (some of which had $\chi_{90}$ values less than 2, e.g. $\tau$ Ceti $\chi_{90}$ = 1.47). There were 53 debris disc candidates left after the quality filters had been applied.

The frequency of debris discs obtained from the AKARI All Sky Survey compares very poorly with recent studies of the previous *IRAS* All Sky Survey (Rhee et al., 2007) and results from various *Spitzer* stellar samples (e.g. Beichman et al., 2006b; Bryden et al., 2006; Trilling et al., 2008, 2007). In the latter cases, this can be interpreted as the result of the fainter excesses

that can be probed by a pointed observation due to longer on-source integration times (MIPS 70 $5\sigma$ sensitivity was 20 mJy cf AKARI WIDE-S 550 mJy). A discussion of the reasons behind the expected reduced detection rates of AKARI compared to *IRAS* was given in Section 4.2.1.1. The dearth of disc detections at 90 $\mu$m, whilst certainly a function, in part, of the reduced sensitivity of a survey satellite over a pointed observatory, also implies that dust emission from debris discs peaks shortward of 90 $\mu$m, or equivalently above temperatures of 50 K. This result is a reflection of our sample (and that of *IRAS*) being biased towards detection of debris discs being easier around hotter, early spectral type stars.

Table 4.4: Table of photometry used to model the photospheres of those A stars observed to have an infrared excess.

| Target | RA (J2000) | Dec (J2000) | Spec. Type | $F_{0.44\mu m}$ [Jy] | $F_{0.55\mu m}$ [Jy] | $F_{1.24\mu m}$ [Jy] | $F_{1.66\mu m}$ [Jy] | $F_{2.16\mu m}$ [Jy] |
|---|---|---|---|---|---|---|---|---|
| HD9414 | 22.912523 | -45.575710 | A0V | 15.06 | 13.66 | 6.04 | 3.84 | 2.65 |
| HD9672 | 23.657412 | -15.676359 | A0V | 24.81 | 22.35 | 10.18 | 6.30 | 4.37 |
| HD13161 | 32.385944 | 34.987297 | A0V | 257.68 | 249.42 | 128.02 | 80.00 | 56.59 |
| HD13218 | 32.023685 | -41.880421 | A4V | 9.76 | 9.87 | 5.84 | 3.90 | 2.74 |
| HD14055 | 34.328613 | 33.847195 | A0V | 113.52 | 99.29 | 48.05 | 29.21 | 17.40 |
| HD17848 | 42.256199 | -62.806522 | A0V | 33.13 | 31.03 | 13.97 | 8.87 | 6.85 |
| HD14943 | 35.727814 | -51.092129 | A1V | 16.85 | 17.16 | 9.30 | 6.51 | 4.45 |
| HD39060 | 86.821198 | -51.066513 | A2V | 113.63 | 112.86 | 60.60 | 40.39 | 27.29 |
| HD54341 | 106.58722 | -43.610752 | A1V | 11.51 | 9.78 | 4.06 | 2.63 | 1.71 |
| HD60178 | 113.65044 | 31.888496 | A2V | 1044.91 | 258.78 | 468.26 | 312.10 | 214.75 |
| HD88300 | 152.64357 | -18.603285 | A1V | 5.048 | 5.51 | 3.65 | 2.48 | 1.77 |
| HD89328 | 154.33409 | -46.834942 | A2V | 9.067 | 10.068 | 7.31 | 5.02 | 3.68 |
| HD102647 | 177.26491 | 14.572061 | A3V | 595.77 | 550.72 | 290.06 | 174.70 | 118.01 |
| HD109573 | 189.00430 | -39.869507 | A4V | 22.40 | 19.22 | 7.74 | 4.93 | 3.28 |
| HD158352 | 262.20691 | 0.33062530 | A5V | 25.79 | 26.75 | 18.94 | 11.41 | 7.98 |
| HD161868 | 266.97318 | 2.7072761 | A6V | 141.61 | 125.01 | 58.57 | 35.15 | 23.74 |
| HD172167 | 279.23474 | 38.783691 | A5V | 4519.38 | 3845.27 | 1881.43 | 1052.69 | 591.47 |
| HD181296 | 290.71335 | -54.423931 | A8V | 44.45 | 38.45 | 14.59 | 8.94 | 6.62 |
| HD216956 | 344.41269 | -29.622236 | A8V | 1469.19 | 1358.08 | 623.00 | 396.55 | 267.87 |
| HD218396 | 346.86966 | 21.134251 | A9IV | 15.41 | 16.27 | 11.20 | 7.91 | 5.34 |

Table 4.5: Table of photometry used to model the debris discs of those A stars observed to have an infrared excess.

| Target | $F_{12\mu m}$ [Jy] | $F_{25\mu m}$ [Jy] | $F_{60\mu m}$ [Jy] | $F_{100\mu m}$ [Jy] | $F_{65\mu m}$ [Jy] | $F_{90\mu m}$ [Jy] | $F_{140\mu m}$ [Jy] |
|---|---|---|---|---|---|---|---|
| HD9414 | | | | | | 0.36± 0.20 | |
| HD9672 | 0.33 ± 0.03 | 0.41 ± 0.07 | 2.00± 0.20 | 1.91 ± 0.19 | | 1.92± 0.41 | |
| HD13218 | | | | | | 0.67± 0.25 | |
| HD13161 | 3.67 ± 0.15 | 1.10±0.09 | 0.78± 0.06 | | | 0.40± 0.24 | |
| HD14055 | 1.07 ± 0.06 | 0.47 ± 0.08 | 0.86 ± 0.07 | 0.85 ± 0.10 | | 0.77± 0.24 | |
| HD14943 | | | | | | 0.52± 0.23 | |
| HD17848 | 0.46 ± 0.02 | | | | | 0.39± 0.16 | 5.15± 1.55 |
| HD39060 | 3.46 ± 0.21 | 9.05 ± 0.45 | 19.9 ± 1.39 | 11.28± 0.90 | 6.63± 0.66 | 7.65± 0.21 | |
| HD54341 | | | | | 1.32± 0.74 | 0.58± 0.18 | |
| HD60178 | | | | | | 0.47± 0.25 | |
| HD88300 | | | | | | 0.73± 0.35 | |
| HD89328 | | | | | | 0.39± 0.22 | |
| HD102647 | 6.97 ± 0.35 | 2.11 ± 0.23 | 1.18 ± 0.13 | | | 0.58± 0.21 | |
| HD109573 | -0.43 ± 0.00 | 3.38 ± 0.30 | 7.36 ± 0.96 | 3.81 ± 0.42 | 5.86± 1.37 | 3.59± 0.31 | 3.02± 0.94 |
| HD158352 | 0.63 ± 0.16 | 0.25 ± 0.04 | -0.51 ± 0. 00 | -1.34 ± 0.00 | | 0.47± 0.27 | |
| HD161868 | | | | | | 1.01± 0.43 | |
| HD172167 | 41.56± 1.66 | 11.02± 0.55 | 9.51 ± 0.76 | 7.76 ± 0.70 | 6.55± 1.32 | 3.78± 0.24 | |
| HD181296 | 0.54 ± 0.08 | 0.48 ± 0.04 | 0.53 ± 0.04 | | | 0.69± 0.36 | |
| HD216956 | 18.21± 2.19 | 4.81 ± 0.38 | 9.02 ± 1.08 | 11.19± 1.45 | 3.31± 0.93 | 7.23± 0.31 | |
| HD218396 | | | | | | 0.60± 0.29 | |

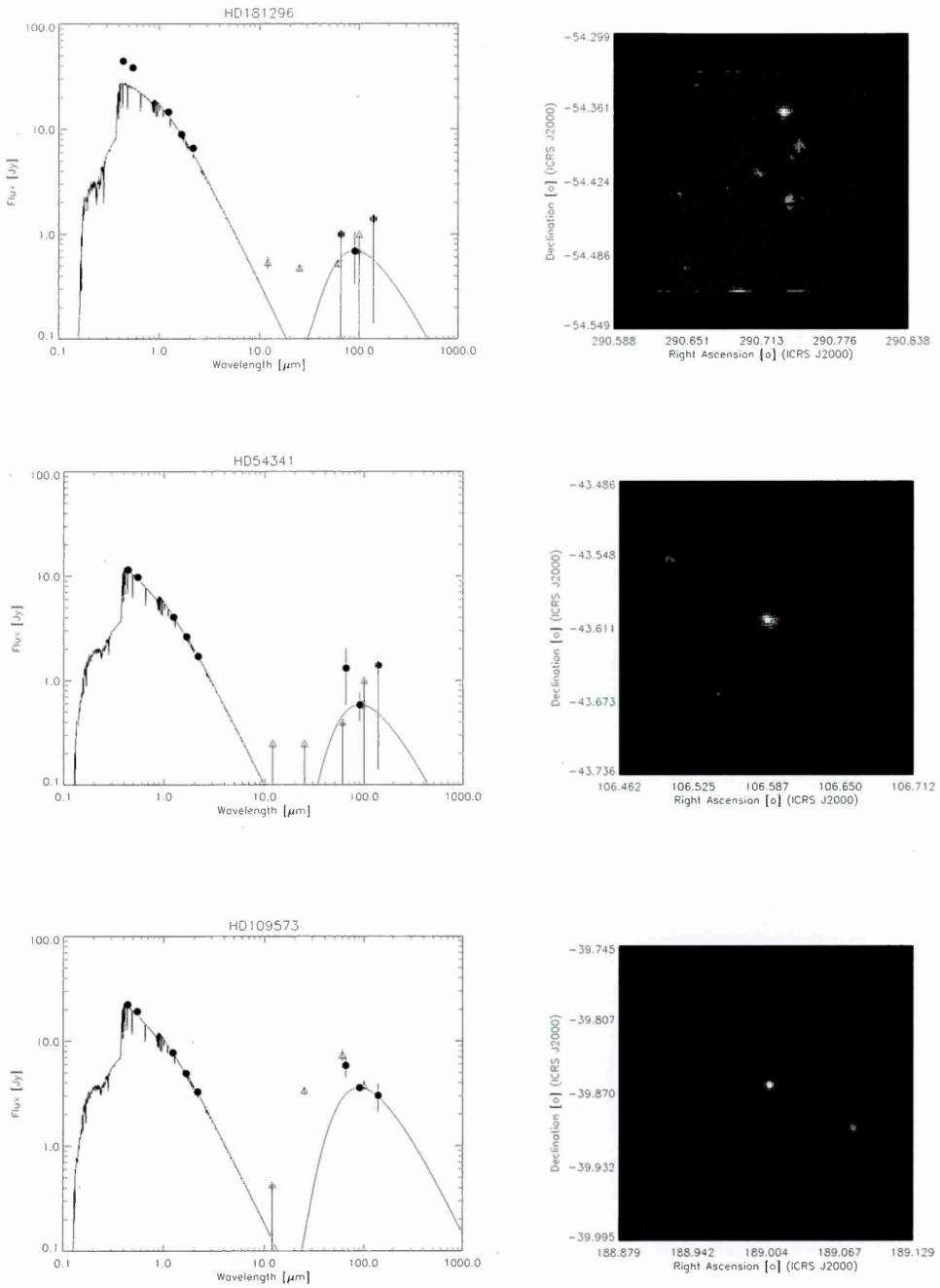


Figure 4.10: SEDs (l) and 90 $\mu$m all sky survey images (r) of the A star debris disc candidate sources HD181296, HD54341 and HD109573. The SEDs are composed of optical/near infrared (diamonds), *IRAS* (triangles) and AKARI (squares) fluxes. A black body (solid curve), peaking at 90 $\mu$m, has been fitted the observed excess. The stellar photosphere is extrapolated from the $K_s$ flux (solid line). Fluxes have not been colour corrected.

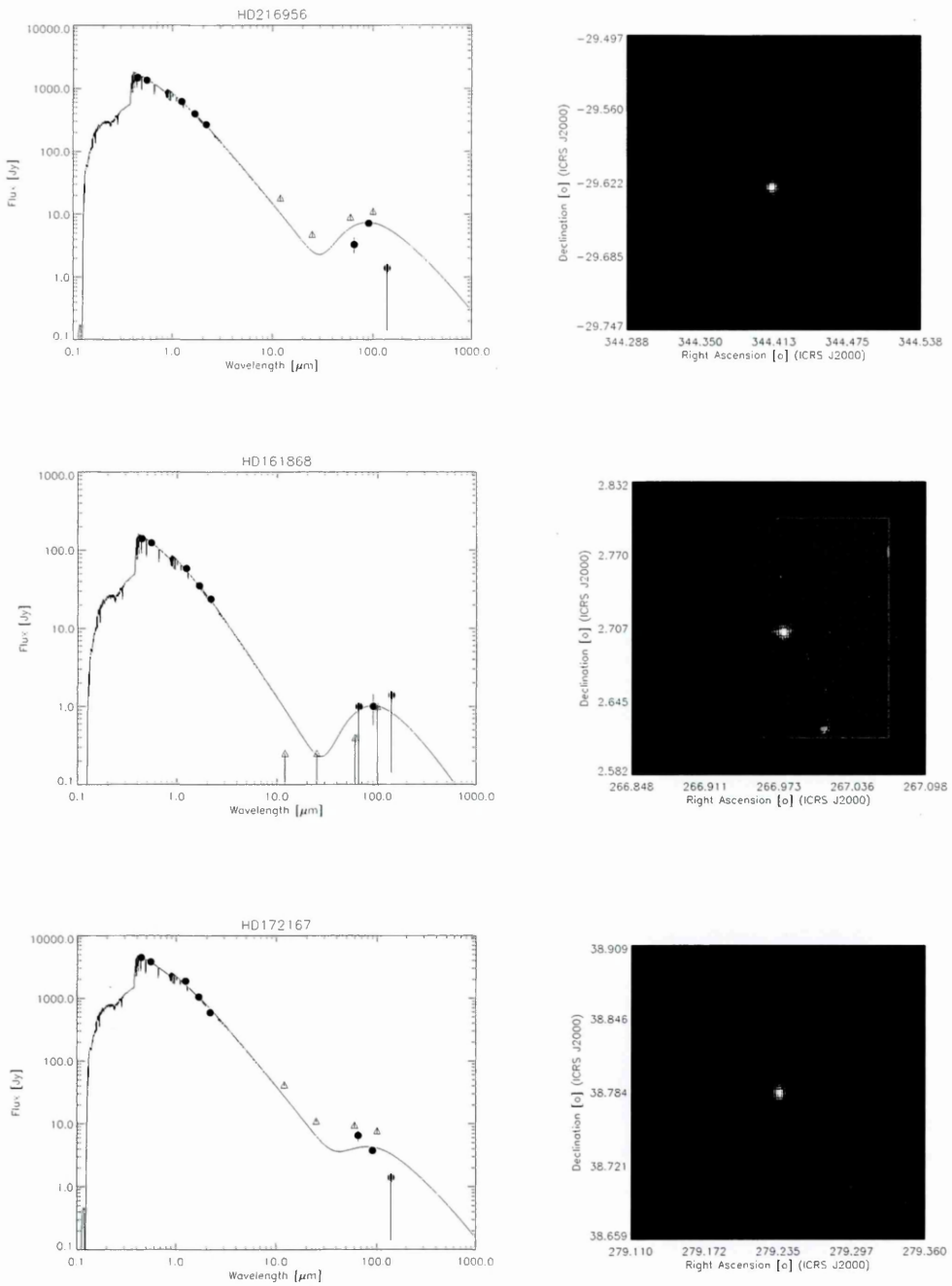


Figure 4.11: SEDs (l) and 90 $\mu$m all sky survey images (r) of the A star debris disc candidate sources HD216956, HD161868 and HD172167. The SEDs are composed of optical/near infrared (diamonds), *IRAS* (triangles) and AKARI (squares) fluxes. A black body (solid curve), peaking at 90 $\mu$m, has been fitted the observed excess. The stellar photosphere is extrapolated from the $K_s$ flux (solid line). Fluxes have not been colour corrected.

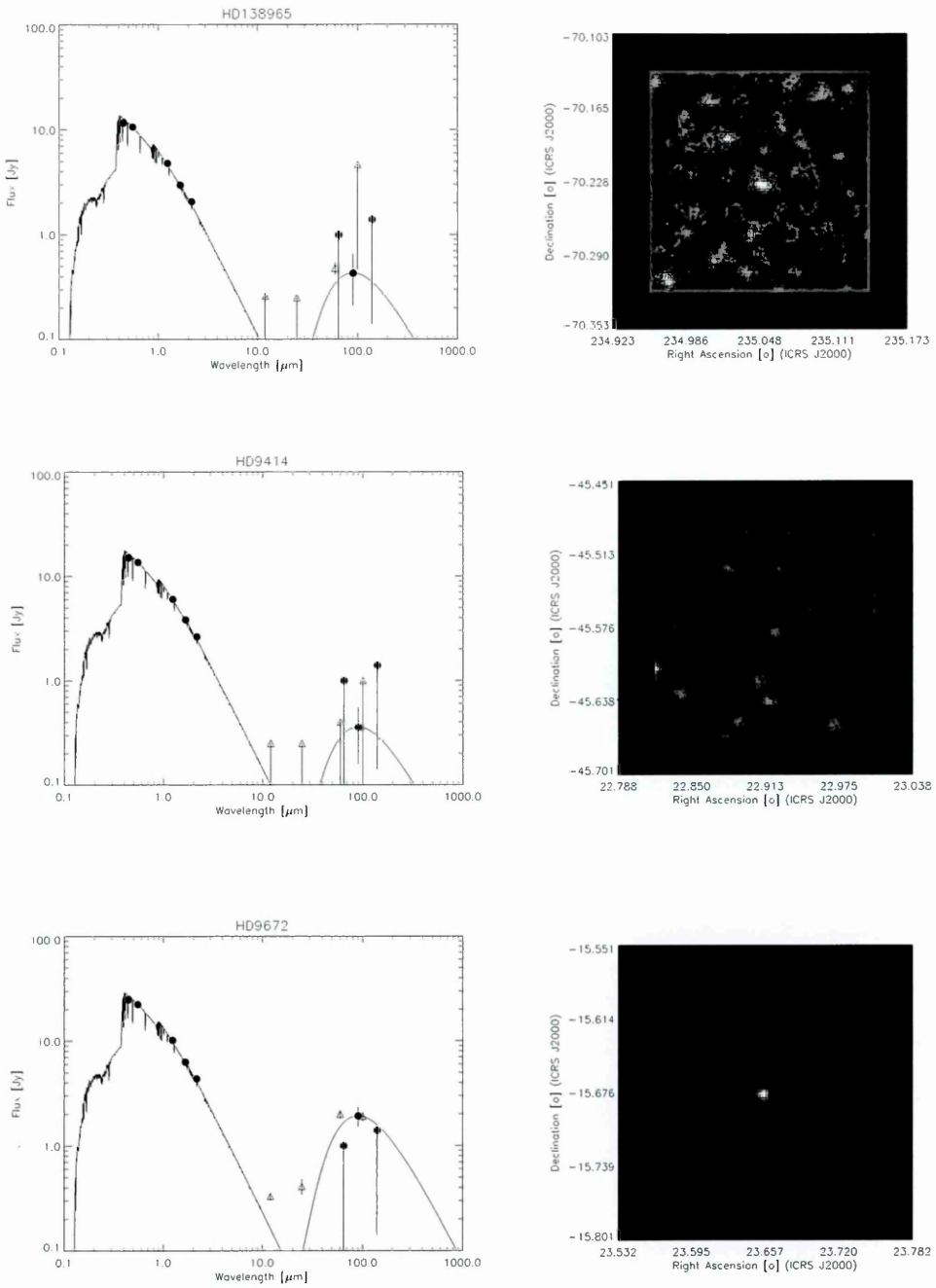


Figure 4.12: SEDs (l) and 90 $\mu$m all sky survey images (r) of the A star debris disc candidate sources HD138965, HD9414 and HD9672. The SEDs are composed of optical/near infrared (diamonds), *IRAS* (triangles) and AKARI (squares) fluxes. A black body (solid curve), peaking at 90 $\mu$m, has been fitted the observed excess. The stellar photosphere is extrapolated from the $K_s$ flux (solid line). Fluxes have not been colour corrected.

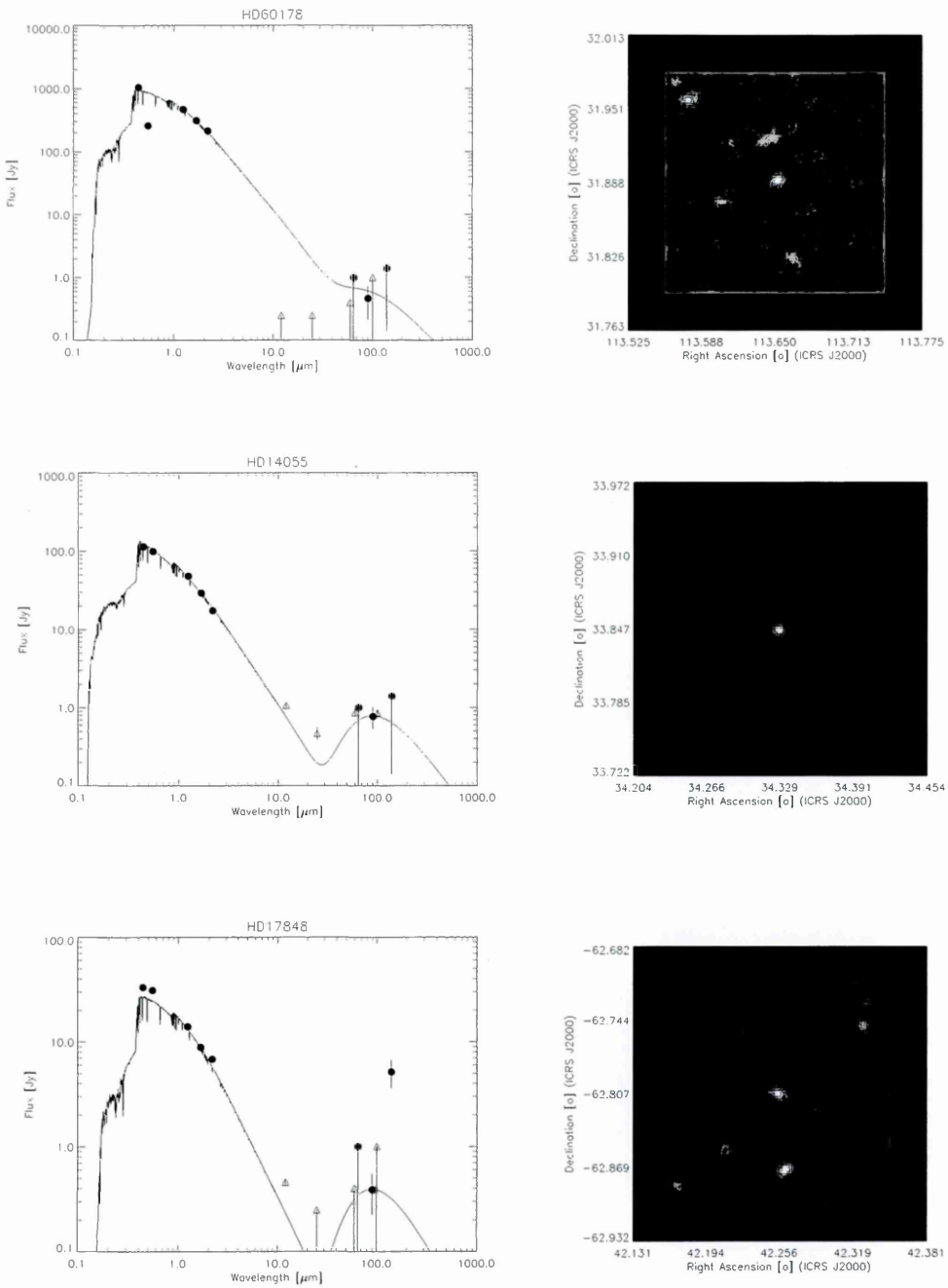


Figure 4.13: SEDs (l) and 90 $\mu$m all sky survey images (r) of the A star debris disc candidate sources HD60178, HD14055 and HD17848. The SEDs are composed of optical/near infrared (diamonds), *IRAS* (triangles) and AKARI (squares) fluxes. A black body (solid curve), peaking at 90 $\mu$m, has been fitted the observed excess. The stellar photosphere is extrapolated from the $K_s$ flux (solid line). Fluxes have not been colour corrected.

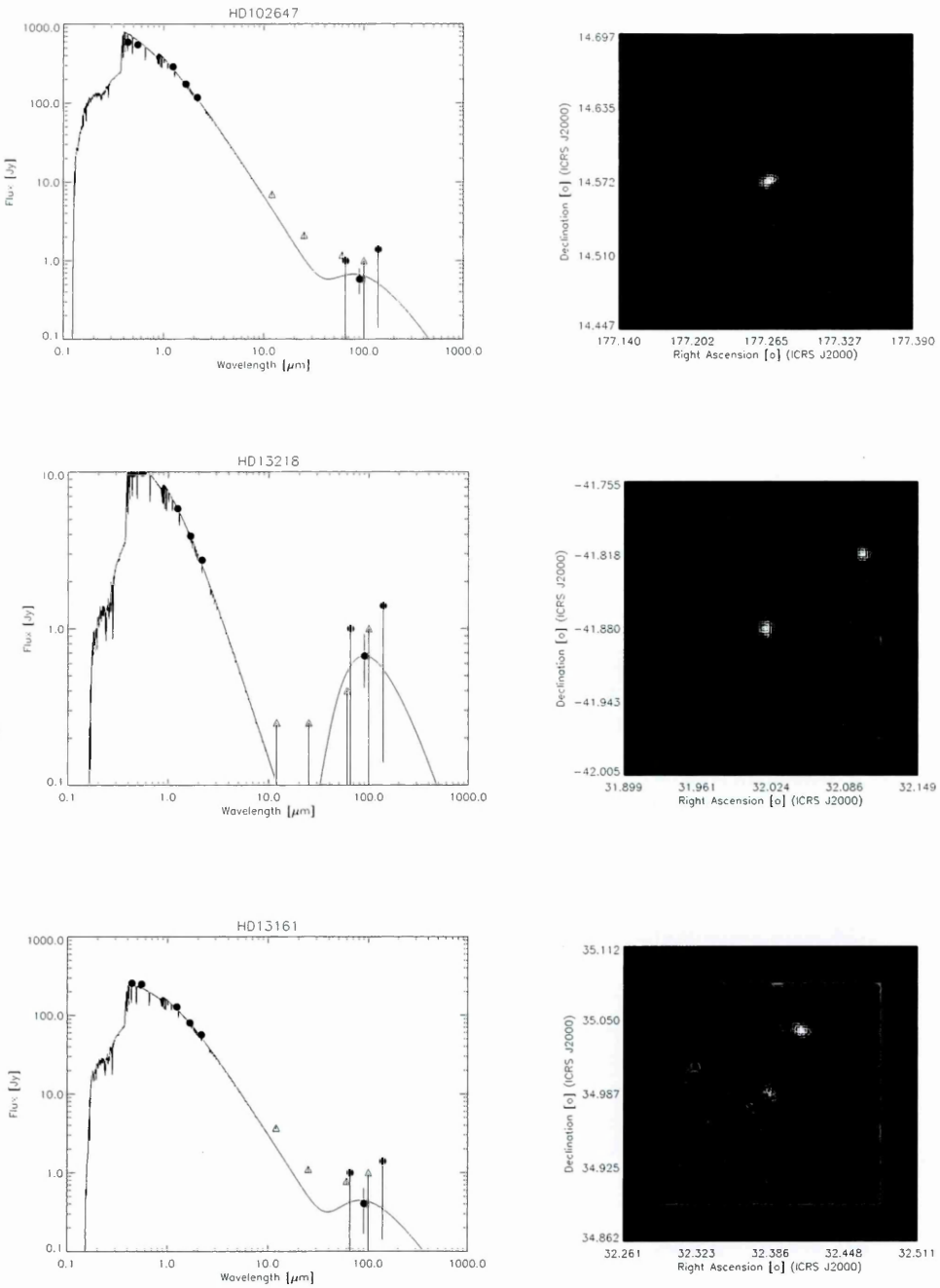


Figure 4.14: SEDs (l) and 90 $\mu$m all sky survey images (r) of the A star debris disc candidate sources HD102647, HD13218 and HD13161. The SEDs are composed of optical/near infrared (diamonds), *IRAS* (triangles) and AKARI (squares) fluxes. A black body (solid curve), peaking at 90 $\mu$m, has been fitted the observed excess. The stellar photosphere is extrapolated from the $K_s$ flux (solid line). Fluxes have not been colour corrected.

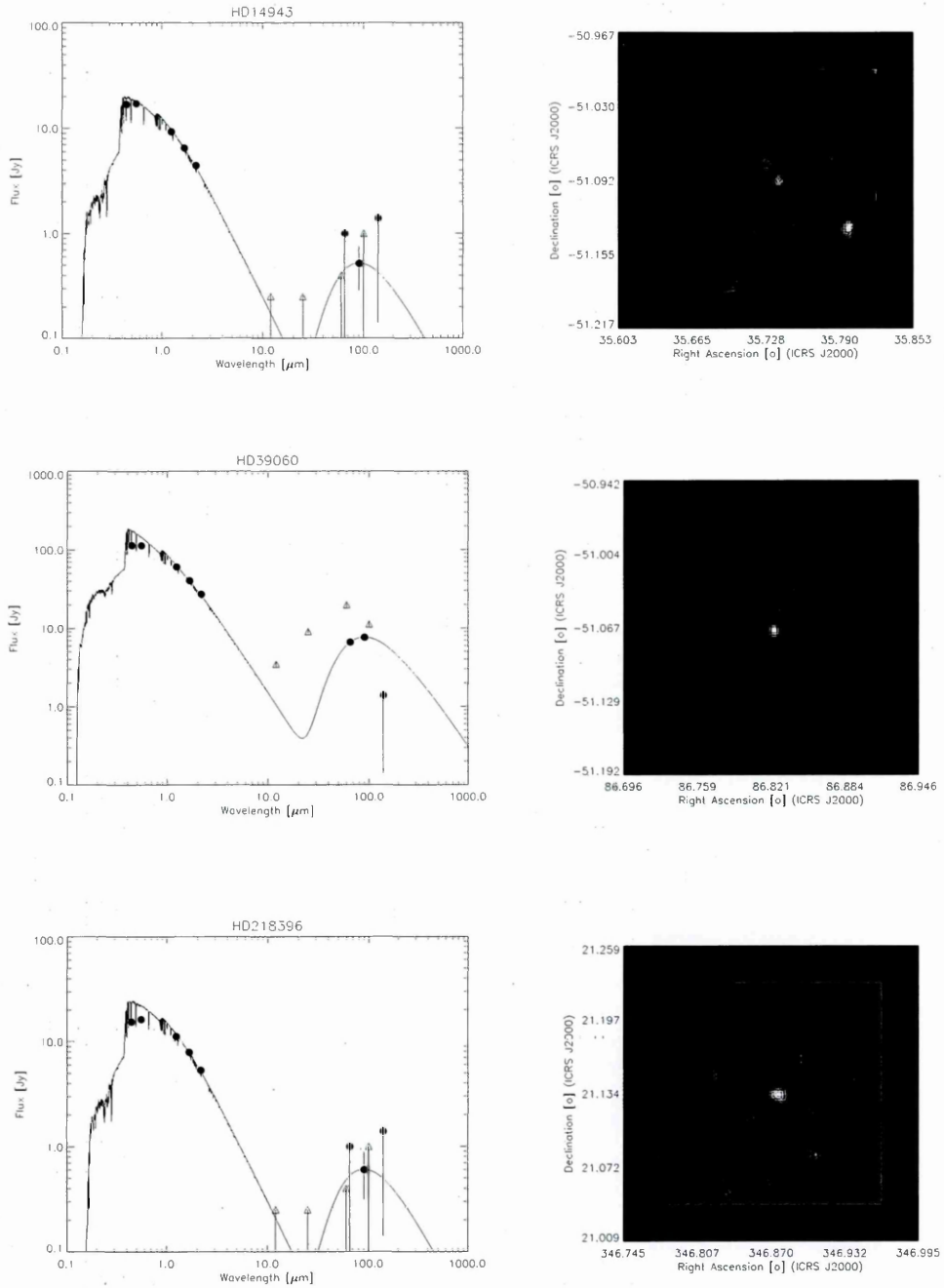


Figure 4.15: SEDs (l) and 90 $\mu$m all sky survey images (r) of the A star debris disc candidate sources HD14943, HD39060 and HD218396. The SEDs are composed of optical/near infrared (diamonds), *IRAS* (triangles) and AKARI (squares) fluxes. A black body (solid curve), peaking at 90 $\mu$m, has been fitted the observed excess. The stellar photosphere is extrapolated from the $K_s$ flux (solid line). Fluxes have not been colour corrected.

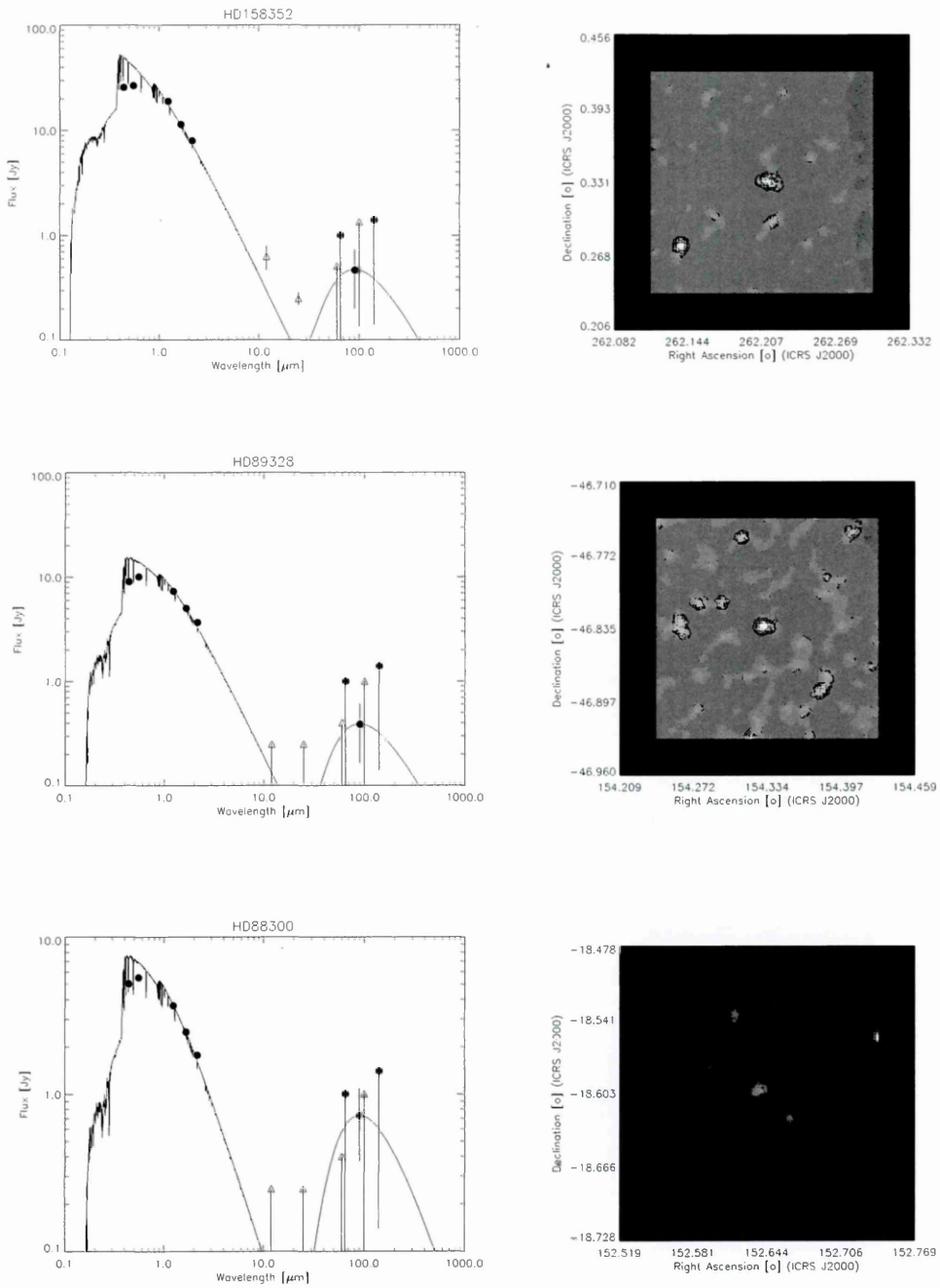


Figure 4.16: SEDs (l) and 90 $\mu$m all sky survey images (r) of the A star debris disc candidate sources HD158352, HD89328 and HD88300. SEDs are composed of optical/near infrared (diamonds), *IRAS* (triangles) and AKARI (squares) fluxes. A black body (solid curve), peaking at 90 $\mu$m, has been fitted the observed excess. The stellar photosphere is extrapolated from the $K_s$ flux (solid line). Fluxes have not been colour corrected.

Table 4.6: Table of modelling results for all debris disc candidates detected in AKARI FIS all sky survey. Table is divided by spectral type in order: AFGK.

| Target | Significance [$\chi_{90}$] | Fractional Luminosity [$\times 10^{-4}$] | Dust Mass [$\times 10^{-4} M_{\oplus}$] | Notes |
|---|---|---|---|---|
| HD54341 | 3.29 | 2.48 | 1112 | |
| HD109573 | 11.41 | 7.83 | 3505 | |
| HD216956 | 22.52 | 0.24 | 108 | Fomalhaut [1] |
| HD161868 | 2.31 | 0.35 | 156 | |
| HD172167 | 14.36 | 0.04 | 18 | Vega [1] |
| HD9672 | 4.68 | 3.79 | 1697 | 49 Ceti [1] |
| HD14055 | 3.15 | 0.33 | 148 | |
| HD17848 | 2.34 | 0.57 | 256 | |
| HD102647 | 2.44 | 0.048 | 21 | [1] |
| HD13218 | 2.65 | 4.14 | 1855 | |
| HD14943 | 2.22 | 1.85 | 827 | |
| HD39060 | 35.91 | 3.29 | 1474 | $\beta$ Pictoris [1] |
| HD218396 | 2.07 | 2.26 | 1013 | HR8799 [1] |
| HD88300 | 2.05 | 8.08 | 3616 | |
| HD22216 | 2.73 | 17.32 | 1294 | |
| HD29645 | 4.03 | 8.98 | 671 | |
| HD40951 | 3.58 | 66.99 | 5006 | |
| HD65134 | 2.93 | 14.10 | 1053 | |
| HD85683 | 2.19 | 6.53 | 487 | |
| HD98770 | 3.57 | 115.68 | 8643 | |
| HD114371 | 2.24 | 1.57 | 118 | |
| HD117214 | 2.61 | 12.48 | 932 | |
| HD181327 | 3.38 | 12.40 | 927 | |
| HD186502 | 2.06 | 7.62 | 570 | |
| HD192886 | 3.31 | 3.40 | 254 | |
| HD224752 | 12.33 | 113.83 | 1859 | |
| HD1040 | 2.49 | 93.36 | 1525 | |
| HD10513 | 3.33 | 109.00 | 1780 | |
| HD19682 | 2.86 | 62.58 | 1022 | |
| HD28199 | 2.51 | 54.82 | 895 | |
| HD28471 | 3.49 | 20.73 | 339 | |
| HD54794 | 2.03 | 45.36 | 741 | |
| HD71386 | 2.17 | 12.56 | 205 | |

Table continues on next page...

| Target | Significance [$\chi_{90}$] | Fractional Luminosity [$\times 10^{-4}$] | Dust Mass [$\times 10^{-4} M_{\oplus}$] | Notes |
|---|---|---|---|---|
| HD76062 | 4.39 | 67.98 | 1111 | |
| HD81221 | 2.54 | 27.76 | 454 | |
| HD97998 | 2.25 | 15.30 | 250 | |
| HD107146 | 2.63 | 11.62 | 190 | [1] |
| HD112019 | 3.52 | 49.09 | 802 | |
| HD112164 | 2.05 | 3.80 | 62 | |
| HD113767 | 2.73 | 34.08 | 557 | |
| HD115844 | 3.63 | 136.71 | 2234 | |
| HD142018 | 2.02 | 98.93 | 1616 | |
| HD180161 | 2.32 | 3.23 | 53 | |
| HD181428 | 2.33 | 14.30 | 234 | |
| HD184357 | 2.50 | 98.78 | 1614 | |
| HD191434 | 2.34 | 15.39 | 252 | |
| HD193193 | 2.12 | 14.40 | 235 | |
| HD200854 | 2.62 | 61.12 | 999 | |
| HD207129 | 2.21 | 1.60 | 26 | HIP 107649 [1] |
| HD222480 | 2.01 | 14.44 | 235 | |
| HD22049 | 2.21 | 0.67394329 | 3.1001168 | $\epsilon$ Eridani [1] |
| HD33263 | 2.04 | 11.21 | 51.58 | |
| HD81961 | 2.13 | 8.55 | 39.34 | |
| HD101206 | 2.85 | 22.36 | 102.86 | |
| HD130373 | 2.07 | 13.36 | 61.43 | |

[1] *IRAS* discovered debris disc
[2] *Spitzer* discovered debris disc

### 4.4.2 Cross Correlation

We obtain 47 matches between the FIS and HD/Tycho-2 catalogues, with a correlation radius of 20″. All of the stars detected via the cross correlation analysis have a signal to noise > $5\sigma$. The debris disc stars noted in the targeted search with a $\chi_{90}$ greater than 5 were recovered from the catalogue, comprising half of the detected sample in this analysis. The remaining objects have not previously been identified as debris discs. Their labelling as such is not without difficulty, however.

Table 4.7: Table of fitting results for discs identified through cross correlation between AKARI FIS BSC and Tycho-2 and HD catalogues.

| Target | RA J2000 [◦] | Dec J2000 [◦] | SpType | Distance [pc] | Dust Radius [AU] | $\tau$ [$\times 10^{-4}$] | Dust Mass [$\times 10^{-4} M_{\oplus}$] |
|---|---|---|---|---|---|---|---|
| HD9672 | 23.657412 | -15.676359 | A1V | 61.3 | 38.2 | 1.62 | 9.15 |
| HD10647 | 25.622149 | -53.740834 | F9V | 17.4 | 24.6 | 2.25 | 0.03 |
| HD14055 | 34.328614 | 33.847194 | A1V | 36.0 | 40.9 | 0.09 | 0.83 |
| HD15745 | 38.232543 | 37.333624 | F2V | 63.7 | 30.4 | 3.50 | 2.26 |
| HD31295 | 73.723866 | 10.150833 | A0V | 37.0 | 38.2 | 0.15 | 0.86 |
| HD32297 | 75.614319 | 7.4610225 | A0V | 112.1 | 32.2 | 6.37 | 14.77 |
| HD244152 | 82.558270 | 33.538964 | A0 | — | 34.1 | 11.13 | 41.47 |
| HD39060 | 86.821199 | -51.066514 | A6V | 19.2 | 32.2 | 2.07 | 4.79 |
| CD-444940 | 133.61116 | -45.321960 | A0 | — | 34.0 | 15.66 | 58.35 |
| HD76582 | 134.39667 | 15.581281 | F0IV | 49.2 | 32.2 | 0.41 | 0.95 |
| HD98800 | 170.52204 | -24.777711 | K5V | 46.6 | 17.1 | 105.63 | 0.06 |
| HD102647 | 177.26491 | 14.572060 | A3V | 11.0 | 41.0 | 0.01 | 0.10 |
| HD102870 | 177.67383 | 1.7647181 | F9V | 10.9 | 26.1 | 0.12 | 0.01 |
| HD107146 | 184.77709 | 16.548297 | G2V | 28.5 | 24.7 | 4.33 | 0.07 |
| HD109573 | 189.00430 | -39.869505 | A0V | 67.0 | 34.1 | 5.15 | 19.18 |
| HD114959 | 198.43018 | 20.416265 | K0 | 387.5 | 19.6 | 19.78 | 0.02 |
| HD131835 | 224.22695 | -35.695457 | A2IV | 111.1 | 34.1 | 3.36 | 12.51 |
| HD140855 | 236.70511 | -25.242744 | A5IV | — | 27.4 | 32.44 | 5.48 |
| HD141569 | 237.49062 | -3.9212111 | A0V | 99.0 | 32.2 | 14.88 | 34.49 |
| HD143840 | 240.70620 | -4.8181783 | F1V | 98.7 | 27.4 | 6.72 | 1.13 |
| HD146897 | 244.87184 | -21.403684 | F3V | 131.7 | 27.4 | 19.73 | 3.33 |
| HD168912 | 274.82569 | 52.651919 | K5 | 322.6 | 19.1 | 3.98 | 0.003 |
| HD172167 | 279.23474 | 38.783692 | A0V | 7.8 | 41.0 | 0.02 | 0.20 |
| HD181327 | 290.74560 | -54.538048 | F6V | 50.6 | 27.4 | 8.02 | 1.36 |
| HD185053 | 297.64841 | -81.274375 | F6V | — | 24.7 | 39.99 | 0.62 |
| HD191089 | 302.27173 | -26.224036 | F5V | 53.5 | 29.0 | 2.51 | 1.04 |
| HD195627 | 308.89521 | -60.581749 | F0V | 27.6 | 34.1 | 0.11 | 0.43 |
| HD216956 | 344.41269 | -29.622236 | A4V | 7.7 | 32.2 | 0.17 | 0.40 |

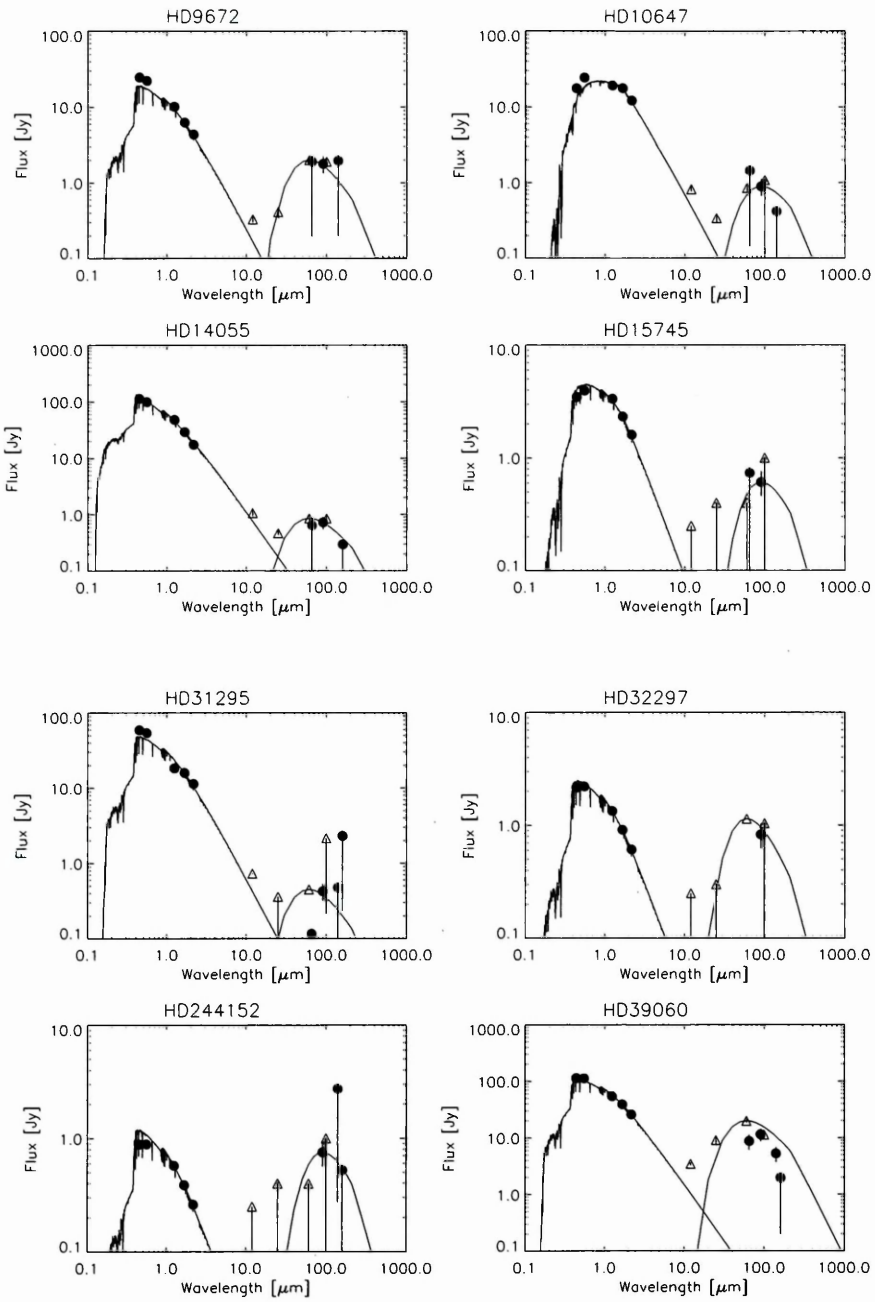


Figure 4.17: SEDs of debris disc candidates picked out from the cross correlation of AKARI and TYCHO-2 catalogues. The stellar SEDs (solid line) have been fitted to the JHK colours. *IRAS* fluxes and upper limits are denoted by triangles, AKARI fluxes and upper limits are denoted by filled circles. Error bars are $1\sigma$.

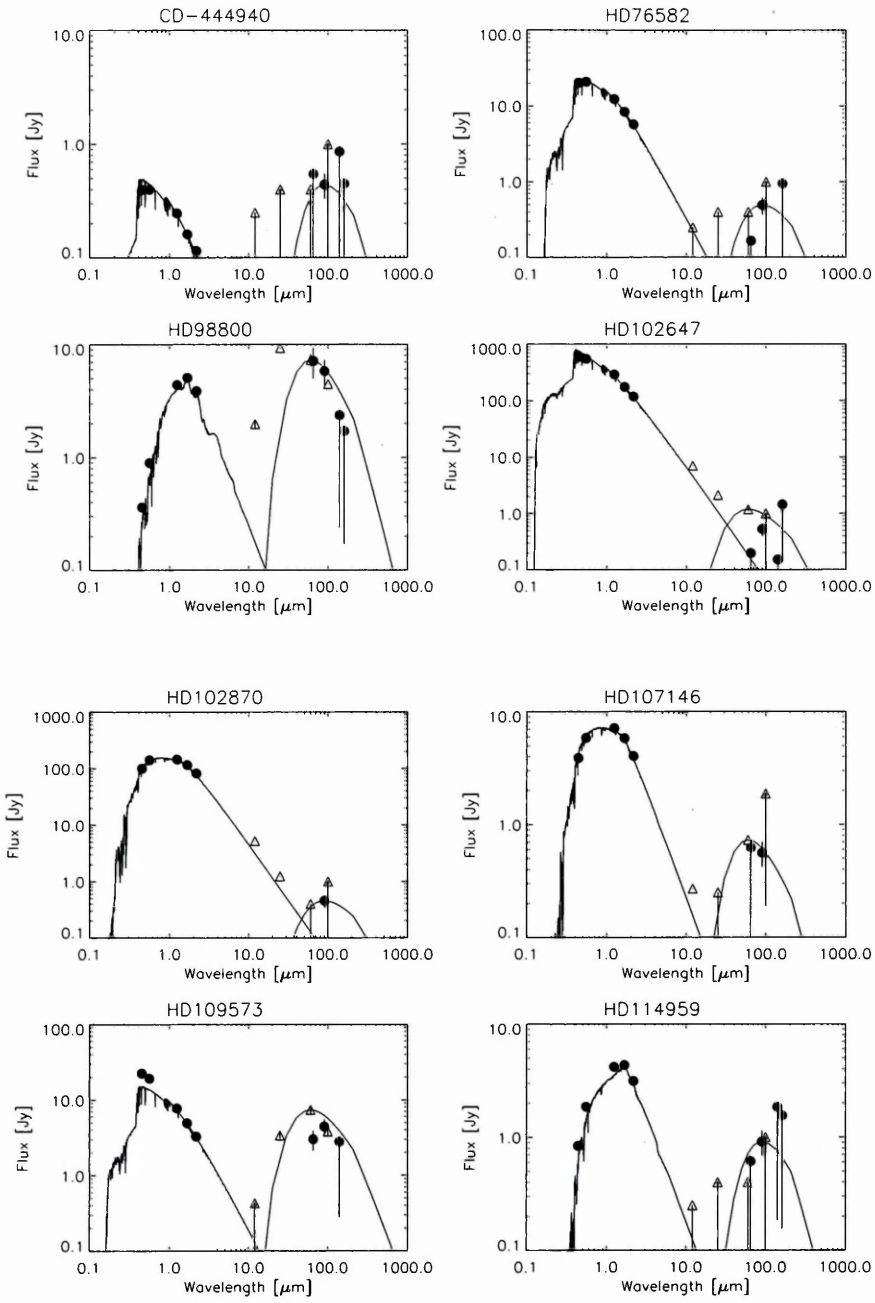


Figure 4.18: SEDs of debris disc candidates picked out from the cross correlation of AKARI and TYCHO-2 catalogues. The stellar SEDs (solid line) have been fitted to the JHK colours. *IRAS* fluxes and upper limits are denoted by triangles, AKARI fluxes and upper limits are denoted by filled circles. Error bars are $1\sigma$.

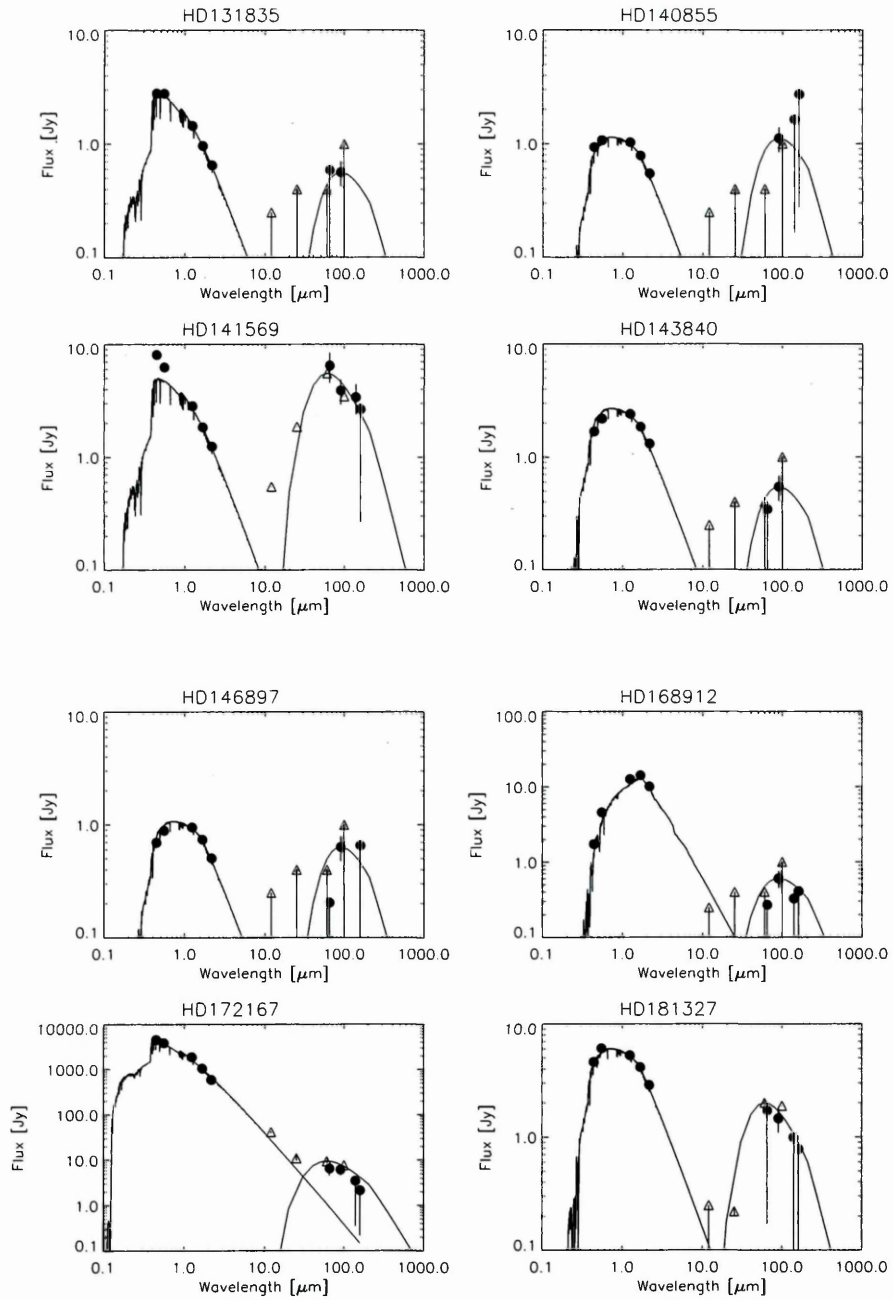


Figure 4.19: SEDs of debris disc candidates picked out from the cross correlation of AKARI and TYCHO-2 catalogues. The stellar SEDs (solid line) have been fitted to the JHK colours. *IRAS* fluxes and upper limits are denoted by triangles, AKARI fluxes and upper limits are denoted by filled circles. Error bars are $1\sigma$.

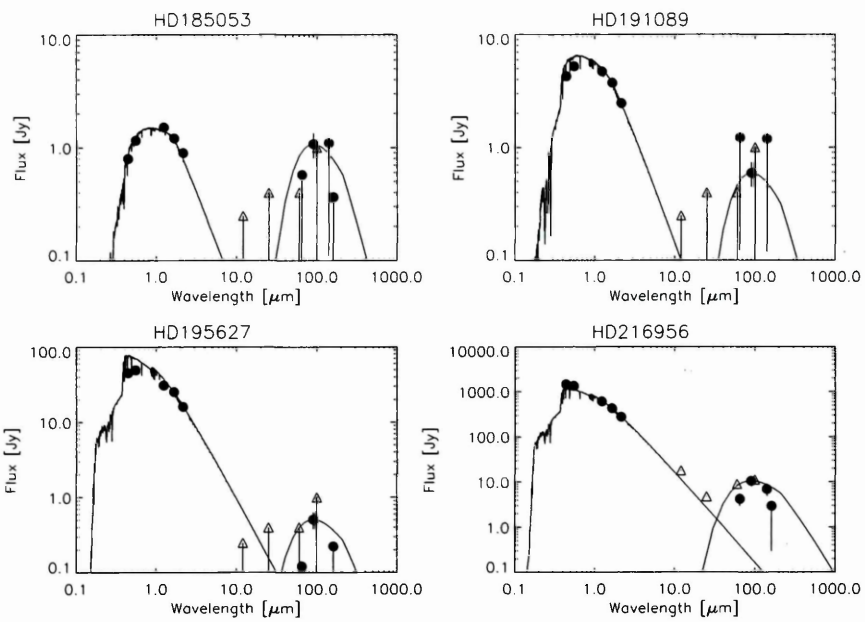


Figure 4.20: SEDs of debris disc candidates picked out from the cross correlation of AKARI and TYCHO-2 catalogues. The stellar SEDs (solid line) have been fitted to the JHK colours. *IRAS* fluxes and upper limits are denoted by triangles, AKARI fluxes and upper limits are denoted by filled circles. Error bars are $1\sigma$.

## 4.5 Discussion

The total source counts from the debris disc survey presented here are much lower than expected, even allowing for the expected reduction in source detection due to reduced sensitivity and longer wavelength of the AKARI WIDE-S versus *IRAS* 60 bands. Only 100 reliable sources were recovered from the all sky survey. Over half of the debris discs are known, bright *IRAS* sources, including the 'fab four' (of which one, $\epsilon$ Eri, does not appear in the BSC) and several very young PMS stars.

Not all of the *IRAS* debris discs have been recovered in the AKARI all sky survey. Several *IRAS* debris discs were observed in the targeted search, but had $\chi_{90}$ values less than 2, for example $\tau$ Ceti with $\chi_{90}$ =1.47. To quantify the relative loss in sensitivity between the two surveys, we have compared the Debris Disc Database[1], a sample of 221 mostly *IRAS* discovered infrared excess stars, assembled by Mark Wyatt and Stephen McGill at the Royal Observatory Edinburgh, with the results from this study.

Of the 221 stars in the ROE DDD, 158 are classified as having a stellar spectral type A–M and a 'debris disc' like excess. We find 55 matches between the ROE DDD and AKARI samples, of which 14 are *IRAS* debris discs.

[1] http://www.roe.ac.uk/ddd/

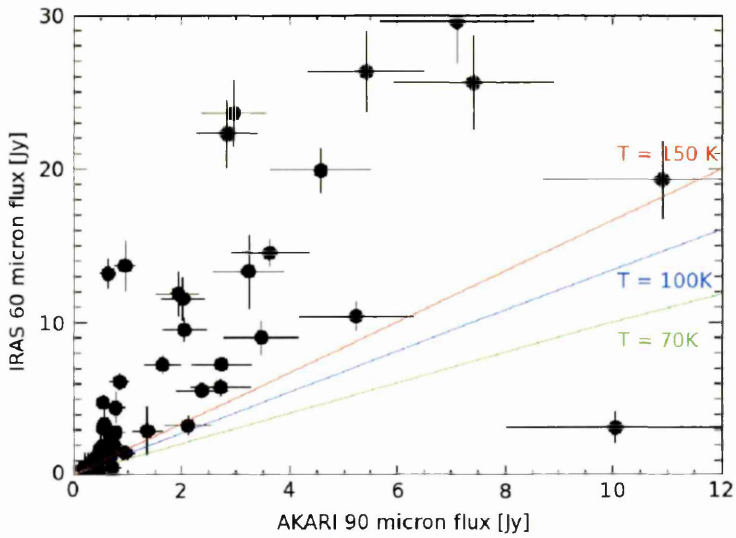


Figure 4.21: Plot of the AKARI 90 $\mu$m flux vs *IRAS* 60 $\mu$m flux for the debris discs from the ROE DDD that were detected by AKARI. The red, green and blue lines represent the $F_{AKARI\ 90}/F_{IRAS\ 60}$ ratio for black body temperatures of 150, 70 and 100 K, respectively. This illustrates that all of the discs found by AKARI are, comparatively, warm.

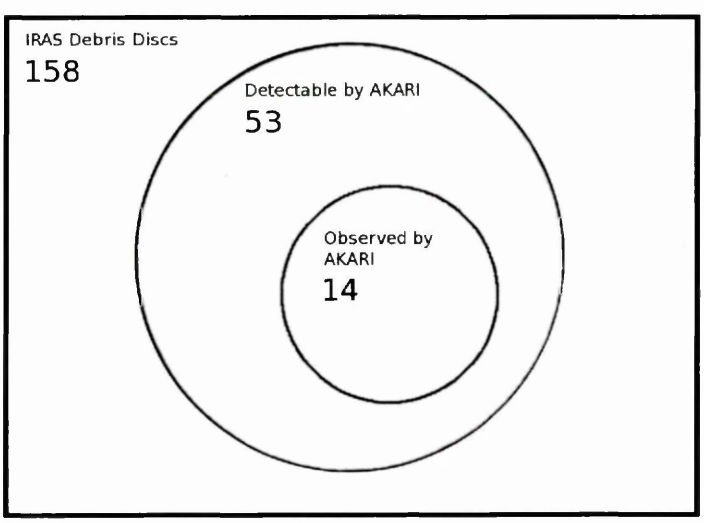


Figure 4.22: There are 158 stars of spectral type A – M described as debris discs in the ROE DDD. In this Venn diagram, we have illustrated the effectiveness of the AKARI all sky survey by comparing the total number of debris discs in the sample with the number that should be detectable by AKARI at 90 $\mu$m, extrapolating from the *IRAS* 60 $\mu$m flux, and those that are seen in the results.

All of the new discs presented in this Chapter were detected in only one waveband (90 $\mu$m), so source confirmation must be required from other instruments, or await improvements to the all sky survey data reduction. The current BSC properties match the pre-launch expected survey sensitivities, with a flux limit of 0.56 Jy at 90 $\mu$m. The completeness of the BSC, estimated from a log($N$)-log($S$) plot, is 90% at 0.6 Jy (see BSC release notes document[1]). This does not therefore explain the discrepancy between the expected and observed number of *IRAS* discs. It is expected that there are more improvements to be made to the catalogue by better understanding of the instrument calibration and time-dependent response of the detectors, leading to further gains in the completeness and depth of the survey catalogue.

## 4.6 Conclusions

A comprehensive, flux-limited survey of nearby stars has yielded several new debris disc stars, expanding the known pool of objects from which we can draw conclusions on the origin and evolution of planetary systems. Previously known debris discs, particularly those discovered by *IRAS*, have had their SEDs extended further into the far infrared wavelength regime, allowing better constraint of the dust disc properties in those systems. The number of debris disc detections falls off as a function of spectral type, consistent with the previous *IRAS* all sky survey. The handful of newly discovered debris discs are all low significance objects, with detection SNR < 3, and are only observed at one wavelength (90 $\mu$m). However, a number of well known debris discs (e.g. $\epsilon$ Eridani, HD 207129) also fall into the same low-significance regime, implying they are strong candidates for follow-up observations. None of the M spectral type stars had a detectable infrared excess, which implies that the frequency of such stars with cold dust discs is less than that of earlier spectral types, consistent with recent results from both *Spitzer* far infrared and sub-mm surveys (Beichman et al., 2006b; Lestrade et al., 2009; Trilling et al., 2008).

Comparison with debris discs from the *IRAS* all sky survey has yielded fewer matches in

[1] www.ir.isas.jaxa.jp/ASTRO-F/Observation/

the AKARI all sky survey than expected from a simple extrapolation of the *IRAS* flux between the two wavelengths. The reasons for the lack of far infrared detections from this sample are partly technical, but are also a result of the typical dust excess peaking around 60 $\mu$m, giving a characteristic size of 30–100 AU to the disc (dependent on the spectral type of the star) and in most cases declining shortward of 100 $\mu$m, implying the dust to be distributed in a narrow annulus. We have therefore ruled out the presence of very cold, bright debris discs (or equivalently extended, massive debris discs) in the solar neighbourhood. Their existence elsewhere is still a subject of study – see Chapter 5 for details.

# 5

# A Search for Warm Infrared Excess From DUNES Targets

## 5.1 Introduction

In this Chapter we present an analysis of mid infrared data from the AKARI 9/18 $\mu$m all sky survey specifically looking for warm dust excesses around stars in the DUNES target list. The superior sensitivity and spatial resolution of the IRC All Sky Survey compared to the *IRAS* 12 and 25 $\mu$m bands makes it a powerful tool to detect excess emission at mid infrared wavelengths, increasing the number of known examples of these rare objects. The data analysis presented here takes the techniques developed in Chapters 3 and 4 and applies them to objects in a similar situation to those identified with cold excess in Chapter 4, being dusty, second generation discs rather than the YSOs examined in Chapter 2.

## 5.2 DUst around NEarby Stars

DUst around NEarby Stars (DUNES[1]) is one of several *Herschel* Open Time Key Programs looking at the far infrared/sub-mm emission from circumstellar dust discs (other programs include DEBRIS, DIGIT and GASPS, see: Augereau et al., 2008). The DUNES program will observe a volume limited sample of 133 Sun-like main-sequence stars of spectral type F,G and K (28 F stars, 53 G stars and 52 K stars) in the Solar neighbourhood ($d < 20$ pc) using the PACS instrument (Poglitsch et al., 2006) at 100 and 160 $\mu$m, with complementary observations for interesting/bright targets at 70 $\mu$m and also using SPIRE (at 250, 350 and 500 $\mu$m, Griffin et al., 2007). The DUNES observations are planned so as to detect the star at 100 $\mu$m with a signal to noise ratio ~7–10, allowing the detection of excess emission at a comparable flux level to that of the predicted stellar photosphere. It is expected that the DUNES survey will detect dust excesses around 20–30% of nearby Sun-like stars (see Fig. 5.1 adapted from Bryden et al., 2006), approaching fractional excesses ($L_{ir}/L_{\star}$) a few times that of the Edgeworth-Kuiper belt in the Solar System.

The sample already has one well known and bright cold debris disc, HIP 7978 (see Liseau et al., 2010, 2008, for details), which was the only one amongst the DUNES sample to be detected in the far infrared all sky survey (see Chapter 4 for futher details of the AKARI observations). In the remainder of the sample there are 15 stars with MIPS 70 $\mu$m excesses, of which six have evidence of rising emission in their IRS spectra (see Table 5.1). The presence of a rising IRS spectrum cannot be taken as a likely indication of IRC excess, since the longest wavelength of the IRS (33 $\mu$m) is beyond that of the filter cut off for the IRC L18W band (28 $\mu$m, see Fig. 5.2 for relative spectral response functions).

[1] www.mpia-hd.mpg.de/DUNES/

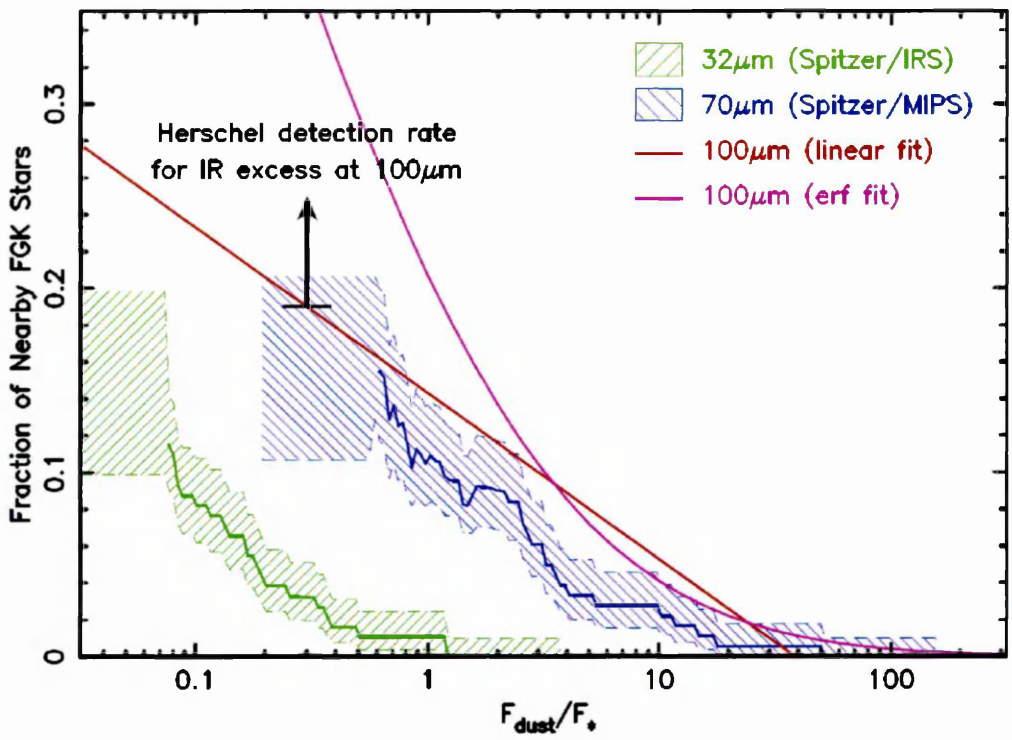


Figure 5.1: Plot illustrating the predicted increase in the incidence of debris discs for ratio of dust to stellar flux. The blue and green hatched areas represent the uncertainties in fractional excess as observed by the *Spitzer* MIPS and IRS instruments (blue and green lines). The red and purple lines represent attempted extrapolations of disc incidence to 100 $\mu$m using log-linear and log-normal disc flux distributions. Taken from DUNES *Herschel* proposal (available from the consortium website).

## 5.3 Mid Infrared All Sky Survey

The AKARI satellite and the FIS all sky survey were described in the previous Chapter. In this Section, the properties of the mid infrared AKARI instrument, the IRC (Onaka et al., 2007), are summarised. Most of the information presented here is taken from the IRC Data Users Manual v1.4 (Lorente et al., 2008) and IRC PSC v1 release notes (Kataza et al., 2010).

The mid infrared IRC all sky survey (Ishihara et al., 2010) was carried out concurrently with the FIS survey, with the FIS survey taking priority during operations. The IRC survey covered 96/97% of the sky at 9/18 $\mu$m with two pointings, similar to the FIS survey (94%). The completeness limit of the IRC survey, determined from the break point of a power law fitted to the distrbution of flux vs. source counts, log($N$)-log($S$), is 0.2 Jy at 9 $\mu$m and 0.3 Jy at 18 $\mu$m (see Figs 5.3 and 5.4). Alternatively, for a limit in source S/N of 5, the flux values quoted above can be divided by three. The uncertainties for the IRC PSC are flux dependent, but an absolute calibration uncertainty of 7% and 15% has been determined for the 9 and 18 $\mu$m bands, respectively. In total, 844,649 sources at 9 $\mu$m and 194,551 sources at 18 $\mu$m were detected in the all sky survey, the majority of these (over 75% in both bands) at fluxes between 0.1–1 Jy. The source catalogues in both bands were compiled separately, and therefore there are some sources which have information in only one of the two bands.

Very few stars exhibit excess emission from warm circumstellar dust (around 2±2% Beichman et al., 2006a). The IRC PSC is deeper in flux by an order of magnitude compared to the *IRAS* 12 and 25 $\mu$m bands (see Figs 5.3 and 5.4). The better sensitivity, and smaller uncertainties, of the IRC compared to *IRAS* enables the detection of warm dust excess around nearby stars at a level of fractional luminosity around $10^{-3}$–$10^{-4}$, comparable to that of *Spitzer*. As an additional benefit of this work to DUNES, the detection of the star in the IRC wavelengths is useful when modelling the stellar photosphere, due to the proximity of the stars in this sample (< 20 pc) and their brightness ($K_s$ < 5.5 mag) introducing large uncertainties if the photosphere is extrapolated solely from the 2MASS $K_s$ band flux. Provision of accurate mid infrared

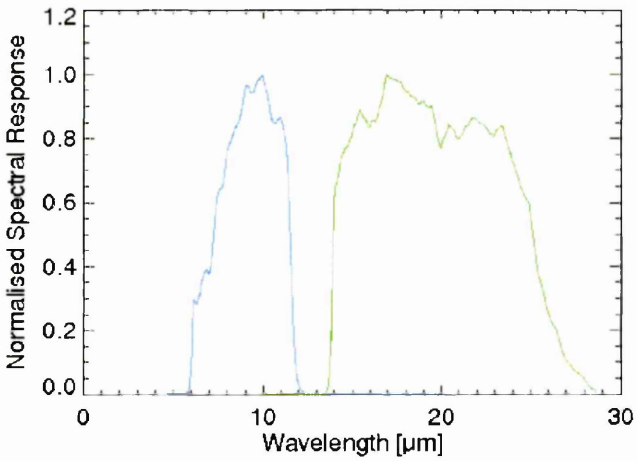


Figure 5.2: Relative spectral response functions of the S9W (blue) and L18W (green) bands, used in the AKARI IRC all sky survey. Both curves have been scaled to the response at the nominal filter wavelengths (9 and 18 $\mu$m, respectively). Taken from Lorente et al. (2008)

photometry (particularly in lieu of IRS spectra) is beneficial to the accurate estimation of the stellar photospheric emission at far infrared wavelengths.

### 5.3.1 Instrumentation

The IRC was originally designed to make wide field, deep survey observations, having a large field of view ($10' \times 10'$), but was also used to take mid infrared all sky observations. There are three focal plane detectors, each with three separate photometric bands: NIR, a near infrared InSb detector operating in three bands equivalent to K,L and M between 1.9–5.3$\mu$m; MIR-S, a Si:As detector which shares its field of view with the NIR detector (see Fig. 4.2(a) for focal plane layout) operating between 6–13 $\mu$m including the S9W band used in the all sky survey; MIR-L, also made from Si:As, operating between 12.6–26.5 $\mu$m and including the L18W band used in the all sky survey. The two MIR Si:As arrays are similar to those used on *Spitzer*'s IRAC instrument (Fazio et al., 2004).

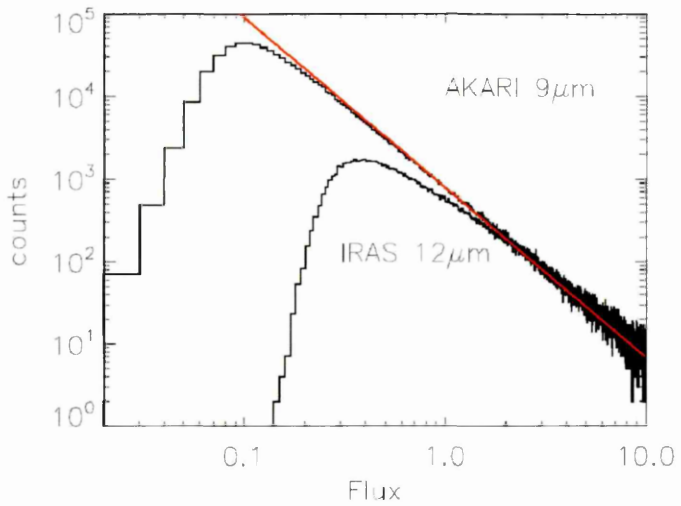


Figure 5.3: Plot of log($N$) vs log($S$) for all the sources detected at 9 $\mu$m in the IRC all sky survey, compared to the same for 12 $\mu$m. The completeness limit of the survey is estimated from the point at which the detected number of source counts (solid black lines) deviates from a fitted power-law (red line), which in this band at 0.2 Jy. Taken from Kataza et al. (2010)

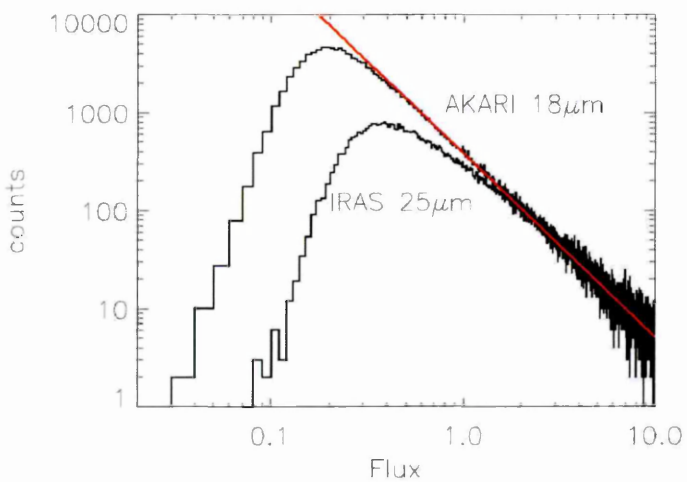


Figure 5.4: Plot of log($N$) vs log($S$) for all the sources detected at 18 $\mu$m in the IRC all sky survey, compared to the same for *IRAS* 25 $\mu$m. The completeness limit of the survey is estimated from the point at which the detected number of source counts (solid black lines) deviates from a fitted power law (red line), which in this band is 0.3 Jy. Taken from Kataza et al. (2010)

### 5.3.2 Observations and Data Reduction

The IRC all sky survey scanned the sky at a rate of 3′25″ per second. A special survey observing mode for the IRC camera (IRC11 and IRC51) was developed, whereby the pixels in the 256 x 256 image array were grouped by row in sets of four giving a cross scan resolution of 9.4″, which had the benefit of reducing the burden on the data down-link. The readout was continuous, so allowing for drift during the readout time (44ms), the separation between readouts of the same row was similarly 9.4″. Details of the data reduction process can be found in the PSC release note (see Section 2, Kataza et al., 2010), but will not be expanded upon here as I was not directly involved in the reduction of raw IRC data or the creation of the PSC.

### 5.3.3 Calibration

IRC colour correction values assume a $\nu F_\nu$ = const spectrum, consistent with *IRAS*, *ISO* and IRAC on *Spitzer*. In the Rayleigh-Jeans limit, a stellar spectrum falls off as a function of $\nu^2$, requiring the calculation of new colour correction factors based on the new input spectral energy distribution. These correction factors were calculated using Eqn. 2.14, given in Chapter 2 and applied before plotting the colour-colour and colour-magnitude diagrams.

Using the model photosphere fits provided by B. Montesinos, the expected photospheric $K_s$–[18] colour is ~0.03 for F and G spectral type stars. For the K type stars, there is some spread towards larger values (up to 0.44) in the predicted values.

### 5.3.4 Cross Correlation

The absolute positional accuracy of the IRC catalogue has been estimated to be 5″ (Ishihara et al., 2009). In this work, matches between the optical (TYC-2) stellar positions and IRC source positions were accepted if the radial offset was less than 10″ in order to maintain consistency with the accepted correlation radius from the FIS analysis in the previous Chapter (the positional accuracy of which was based on the pointing of the IRC). Using a large correlation radius leaves the possibility of false association. The probability of such an occurrence, based

on the source density of the mid infrared all sky survey, is calculated to be less than 1%, and therefore negligible in this sample, of which all are bright, nearby stars with expected photospheric fluxes greater than $5\sigma$ in both IRC bands. Additionally, the sample under analysis is based on a search for cold dust, therefore background contamination (from e.g. cirrus, galactic or extragalactic sources) was a prime concern when choosing the targets.

### 5.3.5 Results

In total we find that 114 stars have matches between the IRC PSC and DUNES source lists. Of these, 110 have matches at 9 $\mu$m and 102 have matches at 18 $\mu$m. Three of the stars have matches at 18 $\mu$m, but no 9 $\mu$m photometry, and therefore we use the predicted photospheric flux provided by B. Montesinos to calculate the mid infrared colour for these targets and their position on the colour-colour plot (see Figs 5.7–5.9).

We use two complementary colour-magnitude and colour-colour plots to aid identification of excess sources, following the method of Fujiwara et al. (2009). We have binned the stars by spectral type and have plotted histograms of the source $K_s$–[18] vs $K_s$ values and use fitted Gaussian to estimate the spread in photospheric values, identifying mid infrared excess candidates based on their position in the colour-magnitude diagram. We then plot the $V$–$K_s$ vs $K_s$–[18] colour-colour diagram to illustrate more clearly those sources that are suspected of excess based on $K_s$–[18] colour.

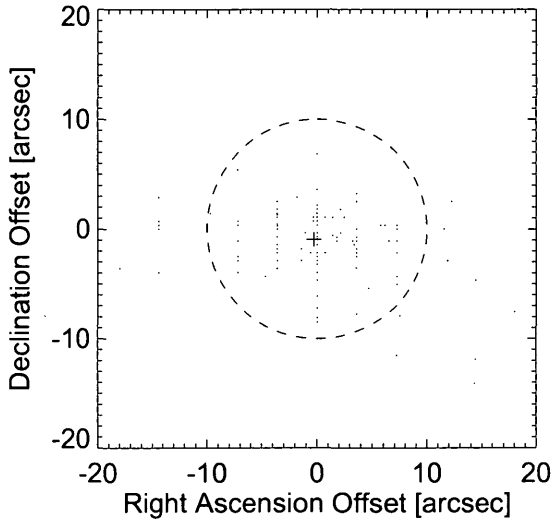


Figure 5.5: Scatter in closest match positions between the IRC PSC and DUNES stars. The mean offset position, -0.29″ in R.A. and -0.95″ in Dec., is denoted by a + symbol. Source matches beyond 10″ (dashed circle) were rejected as candidates for this work.

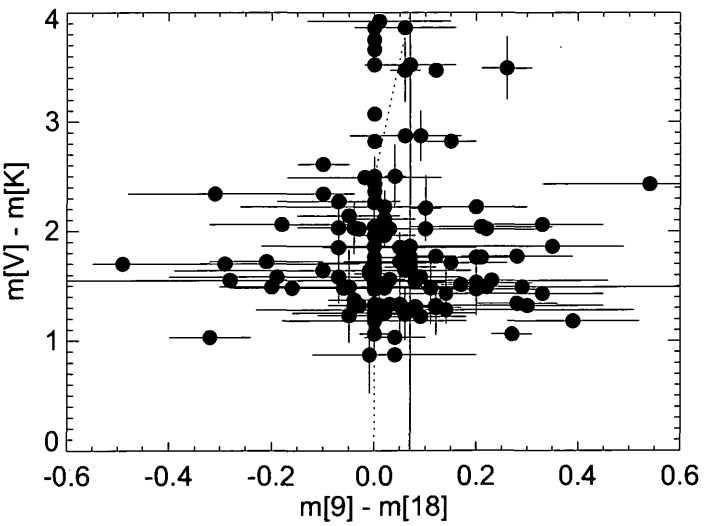


Figure 5.6: IRC mid infrared vs. optical/near infrared Colour-Colour plot for the 102 DUNES targets with 18 $\mu$m fluxes (three sources with 18 $\mu$m fluxes but no 9 $\mu$m fluxes used the predicted photosphere values provided by B. Montesinos). Error bars are $1\sigma$. 14 stars are identified with mid infrared colours inconsistent with photospheric emission. The dashed line represents the locus of expected infrared colour for stars derived from PHOENIX/GAIA stellar photosphere models, provided by B. Montesinos.

Table 5.1: Summary of the cross matches between the DUNES and IRC source lists. Not all DUNES stars were observed, and not all detected stars were observed in both wavebands.

| Source ID | Right Ascension (IRCS, J2000) | Declination (IRCS, J2000) | F[9] [Jy] | $\sigma$F[9] [Jy] | F[18] [Jy] | $\sigma$F[18] [Jy] | Offset[a] [arcsec] |
|---|---|---|---|---|---|---|---|
| HIP171 | 0.54439 | 27.08010 | | | | | 10.14 |
| HIP544 | 1.65421 | 29.02110 | 1.054 | 0.006 | 0.273 | 0.029 | 3.24 |
| HIP910 | 2.81590 | -15.46860 | 2.005 | 0.032 | 0.454 | 0.047 | 2.24 |
| HIP2941 | 9.33946 | -24.76730 | | | | | 10.49 |
| HIP3093 | 9.83987 | 21.24970 | 1.511 | 0.016 | 0.349 | 0.012 | 4.27 |
| HIP3497 | 11.16490 | -65.65100 | 0.612 | 0.018 | 0.168 | 0.012 | 5.74 |
| HIP3821 | 12.27950 | 57.81440 | 10.334 | 0.061 | 2.237 | 0.035 | 6.96 |
| HIP3909 | 12.53120 | -10.64480 | 1.527 | 0.025 | 0.323 | 0.023 | 2.29 |
| HIP4148[b] | 13.25630 | -30.35680 | 0.664 | 0.007 | | | 4.99 |
| HIP7513 | 24.19900 | 41.40470 | 4.147 | 0.013 | 0.926 | 0.032 | 2.93 |
| HIP7978[b] | 25.62270 | -53.74110 | 1.151 | 0.019 | 0.312 | 0.039 | 1.45 |
| HIP8768[b] | 28.20660 | -22.43480 | 0.543 | 0.020 | 0.125 | 0.022 | 5.83 |
| HIP10138 | 32.61710 | -50.82260 | | | | | 21.02 |
| HIP10798 | 34.74330 | -25.94490 | 0.847 | 0.013 | 0.179 | 0.020 | 3.26 |
| HIP11452 | 36.94150 | 4.43245 | 0.573 | 0.007 | | | 1.94 |
| HIP11964 | 38.59420 | -43.79690 | 0.751 | 0.007 | 0.223 | 0.034 | 2.08 |
| HIP12777 | 41.05050 | 49.22840 | 4.197 | 0.040 | 0.991 | 0.038 | 1.32 |
| HIP13402[b] | 43.13480 | -12.77000 | 1.416 | 0.020 | 0.321 | 0.017 | 3.57 |
| HIP14954 | 48.19390 | -1.19625 | 1.942 | 0.022 | 0.423 | 0.014 | 1.47 |
| HIP15330 | 49.44790 | -62.57410 | | | | | 10.2 |
| HIP15371 | 49.55910 | -62.50510 | | | | | 10.5 |
| HIP15799 | 50.89740 | -40.07660 | 0.746 | 0.010 | 0.204 | 0.027 | 1.37 |
| HIP16134 | 51.96940 | -19.80380 | 0.564 | 0.006 | | | 4.42 |
| HIP17420 | 55.98130 | -19.11060 | 0.641 | 0.014 | 0.155 | 0.046 | 2.52 |
| HIP17439[b] | 56.03880 | -38.28130 | 0.587 | 0.008 | | | 2.44 |
| HIP19849 | 63.81340 | -7.65984 | | | | | 30.06 |
| HIP19884 | 63.99050 | -53.30910 | 0.626 | 0.008 | 0.150 | 0.014 | 7.9 |
| HIP22263[b] | 71.90140 | -16.93420 | 1.460 | 0.008 | | | 1.02 |
| HIP23311 | 75.20520 | -5.75584 | 1.746 | 0.023 | | | 8.66 |
| HIP25110 | 80.63700 | 79.23150 | 1.500 | 0.016 | 0.370 | 0.036 | 2.18 |
| HIP27887 | 88.51740 | -60.02360 | 0.683 | 0.007 | 0.159 | 0.009 | 0.72 |
| HIP28103 | 89.10110 | -14.16740 | 3.886 | 0.011 | 0.975 | 0.046 | 1.25 |
| HIP28442 | 90.08010 | -31.02990 | 0.648 | 0.017 | 0.164 | 0.005 | 5.88 |
| HIP29271 | 92.56210 | -74.75340 | 2.418 | 0.007 | 0.539 | 0.013 | 2.21 |
| HIP29568 | 93.43860 | -23.86170 | 0.776 | 0.016 | | | 1.05 |

Table continues on next page...

| Source ID | Right Ascension (IRCS, J2000) | Declination (IRCS, J2000) | F[9] [Jy] | $\sigma$F[9] [Jy] | F[18] [Jy] | $\sigma$F[18] [Jy] | Offset[a] [arcsec] |
|---|---|---|---|---|---|---|---|
| HIP32439[b,c] | 101.55500 | 79.56370 | 1.201 | 0.011 | 0.259 | 0.024 | 4.9 |
| HIP32480 | 101.68500 | 43.57780 | 1.597 | 0.053 | 0.458 | 0.017 | 1.34 |
| HIP33277 | 103.82800 | 25.37600 | 1.090 | 0.005 | 0.251 | 0.074 | 0.94 |
| HIP34017 | 105.87700 | 29.33540 | 0.923 | 0.026 | 0.251 | 0.011 | 6.01 |
| HIP34065 | 105.98800 | -43.60730 | 1.395 | 0.024 | 0.425 | 0.048 | 2.72 |
| HIP35136 | 108.95900 | 47.23960 | 1.329 | 0.016 | 0.255 | 0.035 | 1.39 |
| HIP36439 | 112.48400 | 49.67230 | 1.254 | 0.007 | 0.299 | 0.032 | 1.27 |
| HIP38382 | 117.94300 | -13.89870 | 1.886 | 0.038 | 0.462 | 0.026 | 2.48 |
| HIP38784 | 119.06600 | 80.26560 | 0.631 | 0.010 | 0.153 | 0.008 | 3.42 |
| HIP40693 | 124.60000 | -12.63390 | 1.304 | 0.013 | 0.484 | 0.102 | 6.73 |
| HIP40843 | 125.01600 | 27.21690 | | | 0.530 | 0.036 | 2.95 |
| HIP42430 | 129.78300 | -22.66090 | 2.381 | 0.019 | 0.514 | 0.027 | 3.72 |
| HIP42438 | 129.79900 | 65.02120 | 1.235 | 0.013 | 0.302 | 0.027 | 1.04 |
| HIP43587 | 133.14800 | 28.33040 | 1.408 | 0.022 | 0.290 | 0.016 | 3.79 |
| HIP43726[b,c] | 133.57400 | -5.43438 | 0.903 | 0.012 | 0.154 | 0.026 | 2.67 |
| HIP44897 | 137.21200 | 33.88200 | 0.867 | 0.011 | 0.204 | 0.032 | 1.25 |
| HIP45333 | 138.58500 | 61.42340 | 1.846 | 0.008 | 0.412 | 0.037 | 0.42 |
| HIP45617 | 139.47300 | 28.55940 | 0.750 | 0.015 | 0.130 | 0.035 | 3.89 |
| HIP46580 | 142.47700 | 5.65526 | 0.733 | 0.014 | 0.106 | 0.001 | 3.48 |
| HIP47592 | 145.55900 | -23.91510 | 1.958 | 0.017 | 0.470 | 0.021 | 2.98 |
| HIP49081 | 150.25100 | 31.92290 | 1.634 | 0.019 | 0.398 | 0.018 | 4.73 |
| HIP49908 | 152.83700 | 49.45320 | | | | | 12.21 |
| HIP51459 | 157.65600 | 55.98060 | 2.122 | 0.013 | 0.480 | 0.012 | 1.47 |
| HIP51502 | 157.76500 | 82.55880 | 1.156 | 0.007 | 0.334 | 0.014 | 2.12 |
| HIP53721 | 164.86600 | 40.43040 | 2.070 | 0.019 | 0.446 | 0.038 | 2.76 |
| HIP54646 | 167.77300 | 30.44570 | 0.627 | 0.018 | 0.173 | 0.094 | 4.53 |
| HIP56452 | 173.62100 | -32.82980 | 1.440 | 0.007 | 0.424 | 0.045 | 7.05 |
| HIP57507 | 176.81500 | -30.28690 | 0.691 | 0.017 | 0.129 | 0.012 | 2.18 |
| HIP57939 | 178.25500 | 37.70740 | | | | | 50.47 |
| HIP58345 | 179.48200 | -27.70810 | 1.100 | 0.015 | 0.297 | 0.030 | 8.8 |
| HIP62145 | 191.05900 | 51.75900 | 0.705 | 0.011 | 0.150 | 0.024 | 4.2 |
| HIP62207 | 191.24700 | 39.27920 | 0.917 | 0.023 | 0.178 | 0.021 | 2.84 |
| HIP62523 | 192.19500 | 24.84000 | 0.790 | 0.018 | | | 2.65 |
| HIP64792 | 199.19300 | 9.42452 | 1.667 | 0.023 | 0.396 | 0.016 | 2.88 |
| HIP64797 | 199.21400 | 17.01650 | 1.379 | 0.023 | 0.365 | 0.012 | 5.55 |
| HIP65026 | 199.94100 | 47.77800 | 1.115 | 0.017 | 0.325 | 0.035 | 1.65 |
| HIP65721 | 202.10700 | 13.77780 | 2.907 | 0.037 | 0.730 | 0.024 | 3.93 |
| HIP67275 | 206.81500 | 17.45690 | 2.633 | 0.012 | 0.559 | 0.014 | 3.41 |
| HIP67422[b] | 207.26600 | 26.97930 | 1.118 | 0.014 | 0.265 | 0.039 | 4.32 |
| HIP67620 | 207.83300 | -24.39110 | 0.842 | 0.022 | 0.216 | 0.086 | 4.81 |
| HIP68184 | 209.38300 | 61.49330 | 1.329 | 0.016 | 0.319 | 0.034 | 1.81 |
| HIP68682 | 210.88500 | 10.78610 | 0.968 | 0.023 | 0.262 | 0.021 | 2.34 |

Table continues on next page...

| Source ID | Right Ascension (IRCS, J2000) | Declination (IRCS, J2000) | F[9] [Jy] | $\sigma$F[9] [Jy] | F[18] [Jy] | $\sigma$F[18] [Jy] | Offset[a] [arcsec] |
|---|---|---|---|---|---|---|---|
| HIP69965 | 214.75300 | -25.81470 | | | 0.269 | 0.042 | 3.42 |
| HIP70319 | 215.81400 | 1.24068 | 0.744 | 0.012 | 0.129 | 0.046 | 3.69 |
| HIP70857 | 217.33900 | 80.80990 | 0.591 | 0.009 | 0.165 | 0.040 | 1.99 |
| HIP71181 | 218.37000 | 52.90930 | 0.692 | 0.009 | 0.159 | 0.009 | 2.37 |
| HIP71681 | 219.88400 | -60.83340 | | | | | 25.14 |
| HIP71683 | 219.88400 | -60.83340 | | | | | 31.5 |
| HIP71908 | 220.62600 | -64.97560 | 5.078 | 0.019 | 1.180 | 0.033 | 2.28 |
| HIP72567 | 222.56600 | 23.91190 | 0.919 | 0.011 | 0.280 | 0.032 | 1.35 |
| HIP72603[b] | 222.67100 | -15.99740 | 1.291 | 0.016 | 0.332 | 0.028 | 0.81 |
| HIP72848 | 223.34800 | 19.15320 | 1.533 | 0.011 | 0.384 | 0.019 | 3.22 |
| HIP73100 | 224.09600 | 49.62810 | 0.987 | 0.006 | 0.203 | 0.010 | 1.82 |
| HIP73182 | 224.36300 | -21.41470 | | | | | 14.05 |
| HIP73184 | 224.36300 | -21.41470 | | | | | 12.53 |
| HIP73996 | 226.82600 | 24.86890 | 1.561 | 0.010 | 0.344 | 0.019 | 1.67 |
| HIP77052 | 236.00800 | 2.51493 | 1.208 | 0.011 | 0.306 | 0.024 | 0.86 |
| HIP78459 | 240.26100 | 33.30220 | 1.566 | 0.005 | 0.385 | 0.029 | 4.93 |
| HIP78775 | 241.23500 | 39.15660 | 0.711 | 0.010 | 0.135 | 0.029 | 4.82 |
| HIP79248 | 242.60200 | 43.81710 | 0.727 | 0.029 | 0.175 | 0.013 | 2.27 |
| HIP80725 | 247.21900 | 18.41460 | 0.640 | 0.014 | | | 2.35 |
| HIP82860 | 254.00900 | 65.13490 | 2.057 | 0.009 | 0.484 | 0.007 | 2.86 |
| HIP83389 | 255.65200 | 47.08380 | 0.573 | 0.005 | 0.096 | 0.007 | 6.93 |
| HIP84862 | 260.16500 | 32.46570 | 1.678 | 0.007 | 0.393 | 0.024 | 7.36 |
| HIP85235[b,c] | 261.24600 | 67.30680 | 0.869 | 0.004 | 0.199 | 0.007 | 5.46 |
| HIP85295 | 261.43800 | 2.10917 | | | 0.322 | 0.022 | 8.81 |
| HIP86036 | 263.75000 | 61.87390 | 1.931 | 0.007 | 0.462 | 0.012 | 3.2 |
| HIP86796 | 266.03600 | -51.83440 | 2.081 | 0.022 | 0.524 | 0.005 | 1.4 |
| HIP88601 | 271.36400 | 2.49774 | 10.329 | 0.116 | 2.267 | 0.036 | 8.54 |
| HIP88972 | 272.40500 | 38.45700 | 1.144 | 0.013 | 0.315 | 0.035 | 3.51 |
| HIP89042 | 272.60900 | -62.00190 | 1.365 | 0.011 | 0.322 | 0.034 | 1.4 |
| HIP91009 | 278.48300 | 51.71850 | 0.707 | 0.011 | 0.132 | 0.013 | 2.95 |
| HIP92043 | 281.41500 | 20.54570 | 3.339 | 0.008 | 0.770 | 0.044 | 2.19 |
| HIP95995 | 292.78100 | 58.58520 | 0.883 | 0.008 | 0.228 | 0.010 | 5.46 |
| HIP96100 | 293.09400 | 69.65790 | | | | | 12.59 |
| HIP96441 | 294.11100 | 50.22160 | 2.203 | 0.015 | 0.544 | 0.013 | 1.82 |
| HIP97944 | 298.57400 | -23.94190 | | | 0.345 | 0.023 | 3.12 |
| HIP98959 | 301.39100 | -67.32220 | 0.898 | 0.015 | | | 7.48 |
| HIP99240 | 302.18700 | -66.18420 | | | | | 11.18 |
| HIP99461 | 302.54200 | -35.88910 | | | | | 1071.48 |
| HIP101955 | 309.90900 | 4.97211 | 0.786 | 0.013 | 0.229 | 0.017 | 6.54 |
| HIP101997 | 310.05000 | -23.77300 | 0.839 | 0.005 | | | 4.73 |
| HIP103389[b,c] | 314.19700 | -26.29650 | 0.916 | 0.007 | 0.209 | 0.029 | 0.65 |
| HIP104214 | 316.73500 | 38.75560 | | | | | 36.8 |

Table continues on next page...

| Source ID | Right Ascension (IRCS, J2000) | Declination (IRCS, J2000) | F[9] [Jy] | $\sigma$F[9] [Jy] | F[18] [Jy] | $\sigma$F[18] [Jy] | Offset[a] [arcsec] |
|---|---|---|---|---|---|---|---|
| HIP104217 | 316.74000 | 38.74820 | | | | | 36.17 |
| HIP105312 | 319.93900 | -26.35340 | 0.893 | 0.011 | 0.201 | 0.035 | 4.28 |
| HIP106696 | 324.17400 | -50.84570 | 0.588 | 0.013 | 0.190 | 0.024 | 4.12 |
| HIP107350 | 326.13100 | 14.77170 | 0.870 | 0.010 | 0.193 | 0.029 | 1.79 |
| HIP107649[b,c] | 327.06600 | -47.30420 | 1.237 | 0.017 | 0.262 | 0.031 | 2.54 |
| HIP108870 | 330.85400 | -56.79080 | | | | | 32.05 |
| HIP109378 | 332.37500 | -7.54963 | 0.655 | 0.003 | | | 3.64 |
| HIP109422 | 332.53800 | -32.54840 | 1.691 | 0.034 | 0.395 | 0.002 | 3.07 |
| HIP110109 | 334.56700 | -53.62830 | 1.739 | 0.014 | 0.417 | 0.026 | 5.31 |
| HIP113357 | 344.36700 | 20.76900 | 1.488 | 0.005 | 0.323 | 0.015 | 1.62 |
| HIP113576 | 345.06500 | -22.52410 | 1.022 | 0.007 | 0.209 | 0.063 | 6.46 |
| HIP114948[b,c] | 349.24200 | -62.00120 | 0.952 | 0.008 | 0.227 | 0.027 | 2.03 |
| HIP116745 | 354.90800 | -72.72360 | 0.822 | 0.012 | 0.256 | 0.034 | 5.69 |

[a]Nearest positional match between DUNES stars and IRC PSC, sources with an offset of greater than 10″ were rejected.

[b] Cold excess identified from *Spitzer* MIPS70

[c] Rising *Spitzer* IRS spectrum

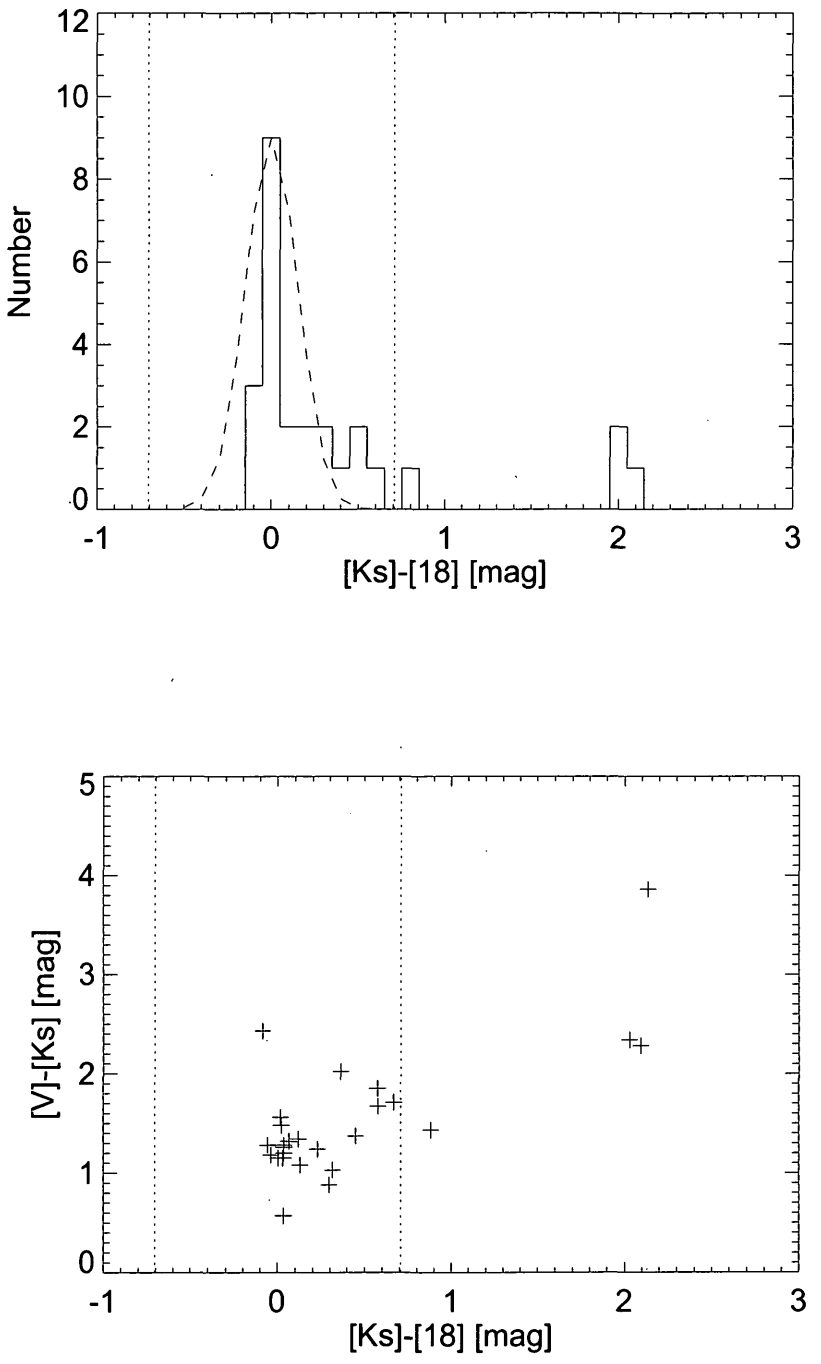


Figure 5.7: Colour-magnitude histogram (t) and colour-colour plot (b) of the 28 F spectral type stars in the DUNES sample. The fitted Gaussian (dashed line) has a mean $K_s$-[18] colour of 0.0, and FWHM of 0.15. The vertical dotted line denotes the $2\sigma$ spread from the mean $K_s$-[18] value.

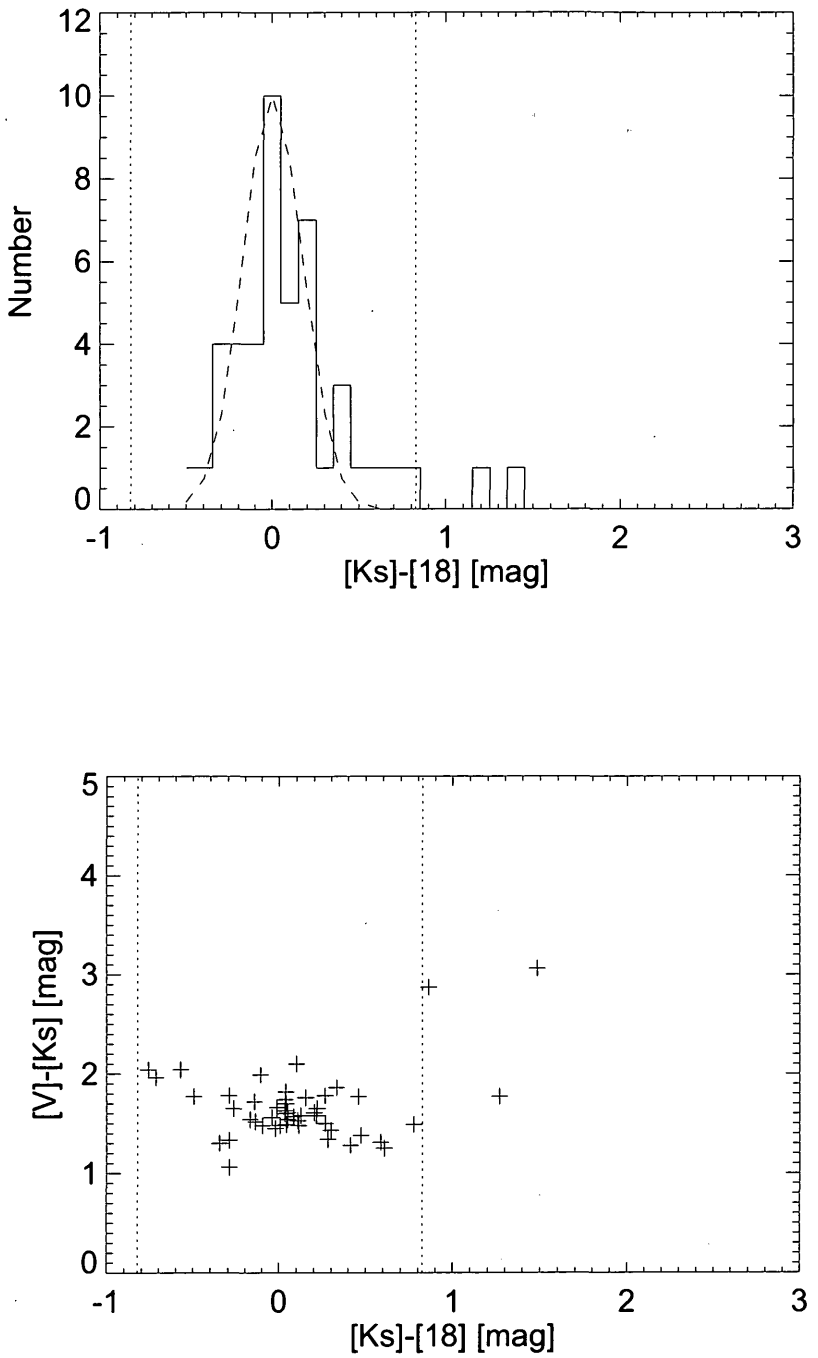


Figure 5.8: Colour-magnitude histogram (t) and colour-colour plot (b) of the 53 G spectral type stars in the DUNES sample. The fitted Gaussian (dashed line) has a mean $K_s$-[18] colour of 0.2, and FWHM of 0.18. The vertical dotted line denotes the $2\sigma$ spread from the mean $K_s$-[18] value.

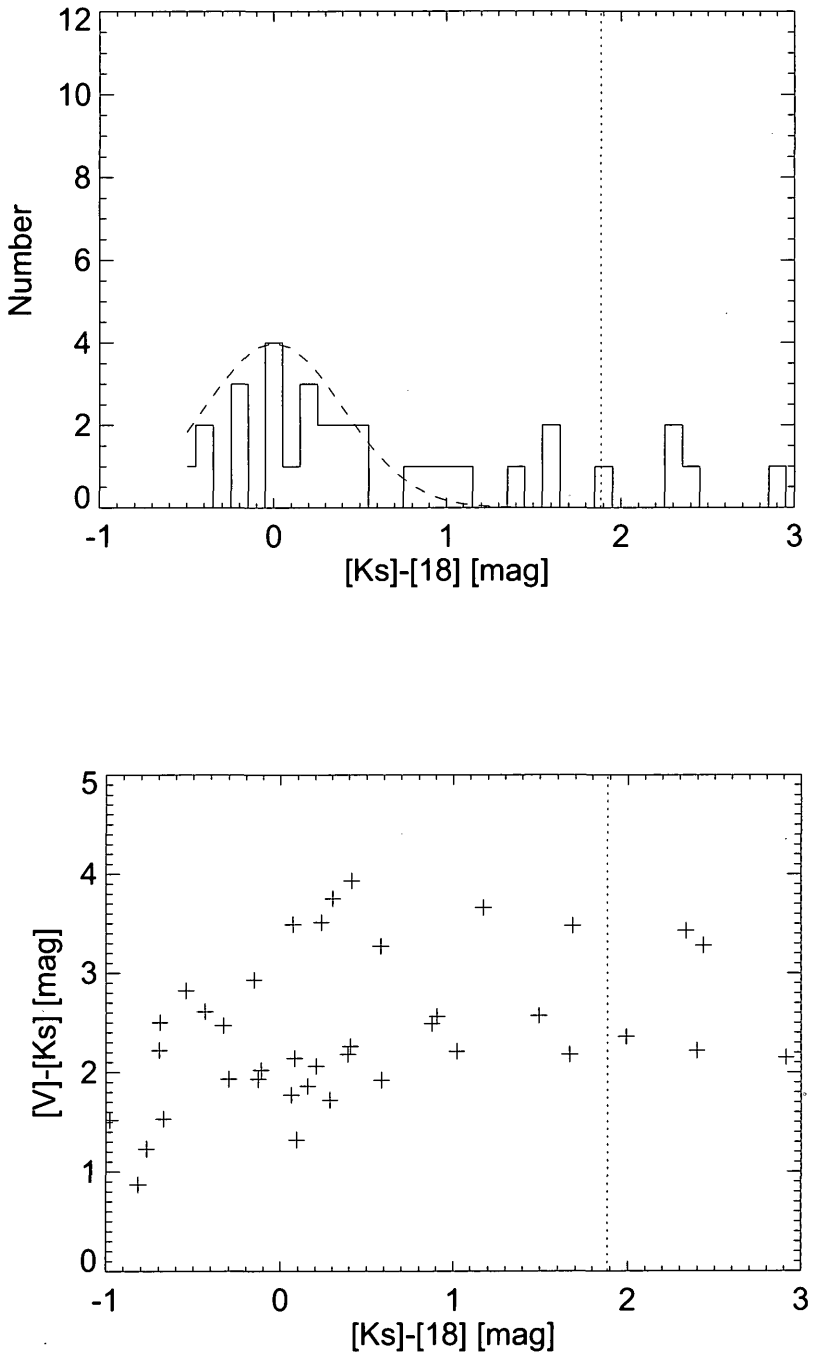


Figure 5.9: Colour-magnitude histogram (t) and colour-colour plot (b) of the 52 K spectral type stars in the DUNES sample. The fitted Gaussian (dashed line) has a mean $K_s$-[18] colour of 0.2, and FWHM of 0.4. The vertical dotted line denotes the $2\sigma$ spread from the mean $K_s$-[18] value.

## 5.4 Discussion

We have identified eight warm debris disc candidates, from a sample of 133, around nearby main sequence solar type stars. This is a slightly higher number of candidates than would be expected from *Spitzer* studies of warm debris discs (Beichman et al., 2006a), from which we would expect at most 6 targets to exhibit an excess at 24 $\mu$m (within the range of the L18W band). It should be stressed that these are warm disc candidates, not debris disc detections, selected as lying more than two standard deviations beyond the measured $K_S$ - 18 colour. Increasing the strictness of our threshold to 3-$\sigma$ beyond the mean would reduce the number of plausible warm excess candidates to three, all of which are F stars. The only known warm disc star, HIP 40693, is of spectral type G8 V. The results presented here should therefore be treated with caution, and further confirmation of these excesses obtained.

All of the discs detected here have not been identified in previous AKARI studies (e.g. Fujiwara et al., 2009). None of the candidates have evidence of a rising IRS spectrum or cold 70 $\mu$m excess from *Spitzer* MIPS measurements. One of the candidates, HIP 28103 is a possible MIPS 70 excess candidate, however. The only K star candidate, HIP 88601 may not be a warm excess due to the uncertainties associated with the stellar photosphere model (B. Montesinos, priv. comm.). The remaining discs are HIP 7531, HIP 12777, HIP 45333, HIP 3821, HIP 29271 and HIP 40693 (see Table 5.2). The last of these targets, HIP 40693, is also known as HD 69830, and possesses three Neptune-mass planets interior to a tightly constrained dust ring at $\sim$ 1 AU from the star, but has no identified cold debris disc (from *Spitzer* MIPS70 measurements).

We explain the lack of detected mid infrared excess detections around stars with a rising IRS spectrum as a function of the L18W spectral response function (see Fig. 5.2), which falls off sharply beyond 25 $\mu$m and is cut off at 28 $\mu$m, whilst most of the rising IRS spectral only begin to deviate strongly from the photosphere beyond 30 $\mu$m.

The frequency of disc candidates decreases as a function of spectral type with lower disc

Table 5.2: Table of the properties of the warm debris discs identified in this work.

| Target ID | Spectral Type | $K_s$-[18] [mag] | F[18] [mJy] | $\tau$ $\times 10^3$ |
|---|---|---|---|---|
| HIP 3821 | G0V | 2.09 | 926.5 | 0.44 |
| HIP 7531 | F8V | 2.13 | 990.6 | 0.32 |
| HIP 12777 | F7V | 2.03 | 975.1 | 0.37 |
| HIP 28103[a] | F2V | 0.88 | 411.8 | 0.28 |
| HIP 29271 | G7V | 3.07 | 2237.2 | 0.49 |
| HIP 45333 | F9V | 1.48 | 538.9 | 0.41 |
| HIP 40693[b] | G8V | 1.27 | 484.2 | 0.96 |
| HIP 88601 | K0V | 2.33 | 2266.6 | 0.77 |

[a]possible cold (70 $\mu$m) excess.
[b]known warm (24 $\mu$m) excess.

frequency around later type stars (14:6:2% around F:G:K stars). The total incidence of warm debris in the DUNES sample is 6 ± 1.5% (the K star and one of the F stars are only possible candidates). The fall off in disc incidence with spectral type is expected, as later type stars are cooler and less luminous so any circumstellar dust around them will be harder to detect if it is at the same radial location from the star.

The mean $K_s$–[18] colours and their dispersion for main sequence stars are in good agreement with the larger samples of Fujiwara et al. (2009) for G and K type stars. For the F stars, the results presented here are consistent with Fujiwara et al. (2009), but are much bluer ($\mu_{Ks}$–[18] ~ 0±0.18, c.f. 0.19±0.15 in their paper). We take this to be a result of the low number statistics, with only 28 F stars in the DUNES sample.

## 5.5 Conclusions

We have performed a search for warm dusty debris around of a sample of 133 nearby stars. Assuming a total incidence of 2±2%, we expected 0–6 discs in the sample. We have identified eight debris disc candidates, though not all of these candidates are certain detections. The frequency of discs decreases with spectral type from four of 28 F stars, three of 53 G stars and one of 52 K stars. The disc fractional luminosities are much brighter than that of the solar

system's zodiacal cloud ($\tau \sim 10^{-4}$, cf. $\tau_{zodi} \sim 10^{-6}$ Vitense et al., 2010). Only one of the stars with detected mid infrared excess has (marginal) evidence for cold dust excess (HIP 28103). The long wavelength observations (100 and 160 $\mu$m) of these stars by *Herschel* will be able to detect the photospheres of the remaining stars and determine if they have cold excesses as well or, like HIP 40963, possess tightly constrained warm dust belts. Confirmation of these warm discs will come from *WISE* (Wide-field Infrared Survey Explorer, Eisenhardt et al., 2009), an all sky survey satellite with superior sensitivity to that of the IRC.

# 6

# A Search for Debris Disc Candidates in a *Herschel* ATLAS Field

## 6.1 Introduction

The *Herschel* Astrophysical Tera-hertz Large Area Survey (H-ATLAS, Eales et al., 2009) is the largest open time program to be undertaken, having been allocated 600 hrs of observing time to survey 510 square degrees of the extragalactic sky around the galactic poles. It will survey the targeted regions at five wavelengths: simultaneously at 110 and 170 $\mu$m using PACS (Poglitsch et al., 2006) and at 250, 350 and 500 $\mu$m using SPIRE (Griffin et al., 2007). The shallow, wide area coverage of the H-ATLAS survey make it complementary to the dedicated debris disc science programs being carried out with *Herschel*. In this chapter, Science Demonstration Phase (SDP) SPIRE observations of an H-ATLAS field are analysed to search for candidate debris discs around foreground stars in the extragalactic field.

## 6.2 Method

### 6.2.1 Cross Correlation

A search for 2MASS (Skrutskie et al., 2006) sources within the ATLAS field was made using the IRSA GATOR tool[1] (specifically, a polygon search with the vertexes slightly outside the ATLAS field). There were 53,657 sources within the area bounded by the polygon. These sources were then cross-correlated with the Tycho-2 catalogue (Høg et al., 2000), using a radius of 2″, to identify stellar sources in the field - it was assumed that only those 2MASS sources with counterparts in the Tycho-2 catalogue were stars. A total of 784 sources were matched between the two catalogues.

The 784 targets with optical and near infrared data were then correlated against the catalogue of sources in the H-ATLAS field of view. Larger correlation radii of 5 and 10″ were used to identify matches between the near-infrared and sub-mm source lists due to the unknown astrometric precision of the *Herschel* catalogue.

### 6.2.2 Estimation of Photosphere

The $B_T$ and $V_T$ magnitudes from the Tycho-2 catalogue were converted into Johnson $B$ and $V$ magnitudes before plotting the SEDs using the relations:

$$V = V_T - 0.090(B_T - V_T) \tag{6.1}$$

$$B - V = 0.850(B_T - V_T) \tag{6.2}$$

The expected photospheric emission of each of the 784 stars in the three *Herschel* bands (250, 350 and 500 $\mu$m) were estimated by extrapolation from the 2MASS $K_s$ flux, assuming the $K_s$ flux is photospheric and that the stellar photosphere falls off $\propto 1/\lambda^2$ in the Rayleigh-Jeans

[1] http://irsa.ipac.caltech.edu/applications/Gator/

tail. A correction was made for interstellar reddening, which was assumed to be small in this field (< 0.1 mag). A comparison between the sources with observed AKARI 9/18 $\mu$m fluxes and the extrapolated photospheric emission shows good agreement (within uncertainties) for those sources, following:

$$F_\lambda = F_{K_s}\left(\frac{2.159}{\lambda}\right)^2 \tag{6.3}$$

The predicted photospheric fluxes were of the order ~ a few $\mu$Jy and we did not expect to detect the stellar photosphere of any of the targets in the field. See tables of cross correlated sources (in the results section) for estimated and observed fluxes of the detected sources.

### 6.2.3 Stellar Spectral Type

The photospheric contribution of each source to the spectral energy distribution (SED) was estimated by least squares minimisation of the stellar *V-K*, *J-H*, *H-K* and *J-K* colours with those of infrared spectral standards (values from Bessell & Brett, 1988). Once the stellar spectral type was determined, a suitable Castelli-Kurucz model (Castelli & Kurucz, 2004) was scaled to the *H* band flux of the star. In order to account for the impact of interstellar reddening the extinction law from Fitzpatrick & Massa (2009) was used to estimate the optical extinction, $A_V$, and thereby calculate the corrections required for the near infrared bands. The observed optical and near infrared magnitudes were scaled by the extinction values calculated by the equation:

$$\frac{A_\lambda}{A_V} = \left(\frac{0.349 + 2.087R_V}{1 + (\lambda/\lambda_0)^\alpha}\right)\frac{1}{R_V} \tag{6.4}$$

The parameters of the extinction curve, $R_V$ and $\alpha$, were defined as 3.11 and 2.05 respectively, in agreement with both previous literature $R_V$ values and the mean extinction curve from Fitzpatrick & Massa (2009), appropriate for the diffuse ISM. The critical wavelength, $\lambda_0$, was 0.507 $\mu$m.

None of the stars in the sample have age, distance (parallax) or metallicity information. A distance estimate for each star was made by using the distance modulus equation (see Eqn. 6.5) with the estimated extinction from the photosphere fitting and that the stellar absolute magnitudes, $M_V$, calculated from the scaled photosphere model.

$$m_V - M_V = 5log_{10}(d_\star) - 5 + A_V \tag{6.5}$$

An estimate of the uncertainty in the distances obtained through this fitting process was made by fitting the optical and near infrared magnitudes of a number of stars with known spectral types and distances. With the caveat of accurate (within three spectral bands) spectral typing, the distances to the TYCHO sources can be considered accurate to within 50%, from the standard deviation of photometry derived distances compared to the parallax derived measurements. If the spectral type is incorrectly determined from the optical/near infrared photometry, as may be the case for stars with shallow BVJ slopes (e.g. late A, F and early G stars), the ascribed distance may be even worse.

### 6.2.4 SED Fitting

The SPIRE photometry was fitted using two different excess models - a single black body and a grey body with the flux reduced by a factor $(210/\lambda)$ beyond 210 $\mu$m. The parameters of the disc model were the fractional luminosity ($\tau$) and temperature ($T$). The best fit of the two parameters was determined through least-squares fitting. Combining the derived best-fit disc temperature and stellar spectral type, the radial location for the dust was determined (see Eqn. 6.6).

$$r_{dust} = (278/T_{dust})^2 L_\star^{0.5} \tag{6.6}$$

The mass of the dust disc was calculated using the equation below using the 500 $\mu$m flux and adjusting the value of $\kappa_{abs}$ by a factor of $210/\lambda_{\mu m}$ from the literature value of 1.7 $cm^2g^{-1}$ at

850 $\mu$m (Eqn. 6.7 Zuckerman, 2001), and then using:

$$M_{dust} = \frac{S_\nu d^2}{B(\nu, T_{dust})\kappa_{abs}} \tag{6.7}$$

### 6.2.5 Contamination

The H-ATLAS field studied here covers an area of 16 square degrees. There are 14,900 sources in the catalogue used to identify debris discs, equivalent to 1 source every 4 square arcminutes. Most of these sources are expected to be galaxies. The probability that a false-positive correlation could be made between a star and a galaxy that lies along the same line of sight is therefore estimated from the density of sub-mm sources in the field, using the prescription from Condon et al. (1998) (their Eqn. 4).

$$P(< r) = 1 - e^{-\pi\rho r^2} \tag{6.8}$$

In the above equation, the probability $P$ that a source within a distance $r$ of an optical counterpart is a false positive is a function of the source density$\rho$ and the critical radius, $r$. For the H-ATLAS field studied here, the number density of sources is 931 sources per square degree. For critical radii of 5 and 10″, the probabilities of a false positive are therefore estimated as 0.17% and 2.2%, respectively.

A Monte Carlo study of the correlation probability undertaken by Mark Thompson (priv. comm.) compared a randomised version of the Tycho-2 sources in the region with the SPIRE catalogue looking for associations. His study showed that the number of direct correlations within 10″ were overestimating the likely true number of star-submm associations (10 in the data, compared to 5.7±2.4 expected from the MC study), and that beyond a correlation radius of 6″ the rate of increase of associations between the optical and submm became flat (see Fig. 6.2.5.

We interpreted this as illustrating the best correlation radius is 6″ for sources in this study,

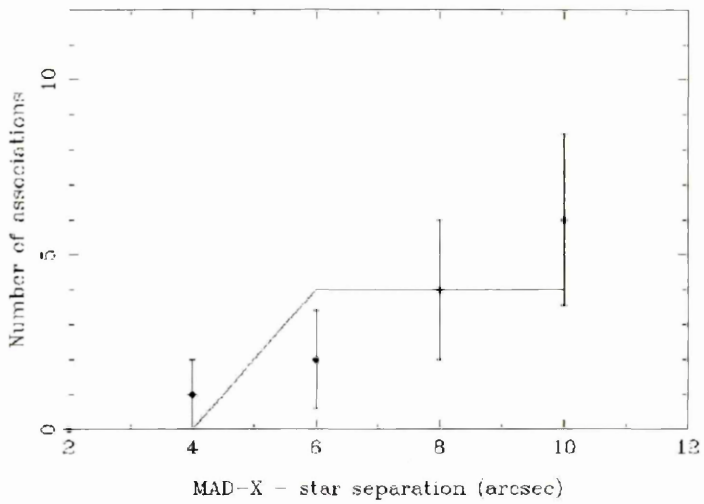


Figure 6.1: Plot of the separation between Tycho-2 catalogue stars and a randomised field of background sources. The increase in the number of associations falls off outside of a radius of 6″, implying that real associations are more likely to lie within that correlation radius (figure provided by M. Thompson). The solid line shows the result of Monte Carlo simulations of the source correlation radius.

leaving us with 4 out of 6 discs from the entire sample.

## 6.3 AKARI IRC Sources

The AKARI IRC (and FIS) all sky survey catalogues were matched with the 784 Tycho-2 sources to identifiy any with mid-infrared excess. We obtained 88 matches between the Tycho-2 and IRC catalogues (using a 2″ correlation radius, from the instrument pointing accuracy), one of which, TYC213-329-1, had a mid-infrared excess at 18 $\mu$m determined (see Fig. 6.2). The positional offset between the star and IRC position is 1.3″, within the AKARI 1$\sigma$ uncertainties (see also Chapter 4). None of the FIS sources in the field were found to have IRC or 2MASS counterparts (using a 10″ correlation radius). A correlation between the 2MASS/IRC stars and the H-ATLAS catalogue did not turn up any matches. The AKARI stars had photospheres that were typically 10× brighter than those of the stars associated with sub-mm sources in the H-ATLAS SPIRE catalogue.

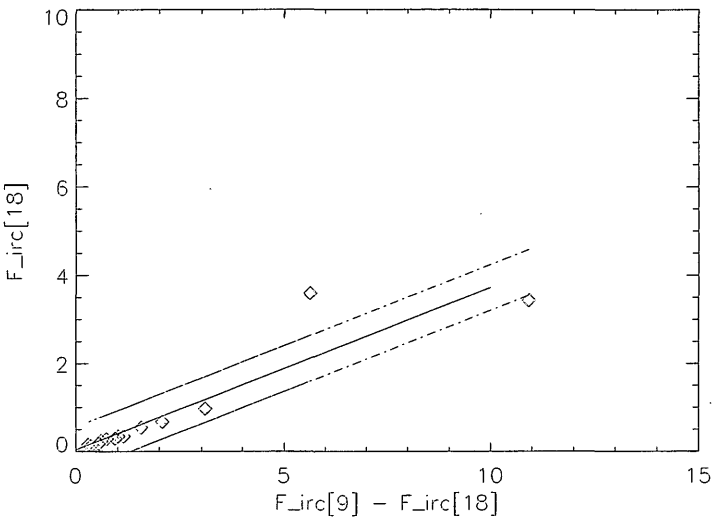


Figure 6.2: Colour vs Flux (in mJy) plot to determine the presence of mid infrared excess for the 13 AKARI IRC sources in the *Herschel* field of view. The solid line shows the straight line fit to the data points, whilst the dashed lines show the $3\sigma$ scatter. One source, TYC213-329-1, shows a significant excess.

The detection of a single 18 $\mu$m excess in a sample of 88 stars is consistent with previous *Spitzer* studies of warm debris disc incidence. However, the star in question, TYC213-329-1, is identified as a giant star in Vizier and we find that the optical to mid infrared stellar SED is marginally better fitted by a late K giant spectrum (K7III reduced $\chi^2$ = 1.56, cf K5V reduced $\chi^2$ = 1.69), ruling out the possibility of a warm debris disc in the field.

## 6.4 SPIRE Sources

We identify five SPIRE sources within 5″ of a Tycho-2 stellar position, namely: TYC213-689-1, TYC226-1569-1, TYC4879-168-1, TYC4878-263-1 and TYC4879-744-1, and a further 14 with sources with 10″ (see Table 6.1).

Most of the candidate discs are well approximated by one of the single temperature models. The $\chi^2$ of the model fit to the data is typically improved by a factor of 2 – 4 by adopting the grey body over the black body model. Five of the disc candidates have very poor fits to the data

(those discs with $\chi^2 > 0.5$, see Table 6.2). Amongst the poorly fitted discs is one of the five high quality candidates (see Table 6.2 for summary).

Four systems have discs with sizes ~100 AU, comparable to the size of the Solar System (ignoring TYC4879-744-1, for which the fitting process selected the maximum permissible temperature in the model, see Fig. 6.7). The remainder have sizes of several hundred AU, expected from the cold temperature of dust detected in the sub-mm.

The disc masses derived from the model are much greater (in range $0.1 - 100 M_{\oplus}$) than that of typical debris disc stars (0.01–0.1 $M_{\oplus}$, Sheret et al., 2004). The masses of the discs are derived using the distances provided from fitting to the stellar photometry. The accuracy of such distances are only ~50% (Davenport et al., 2006). This uncertainty therefore dominates the mass estimate. The mass values place almost all of the discs found here in the range of pre-main sequence discs, much larger than typical debris discs. The large disc masses could imply that many of these candidates (particularly the most massive) are actually background galaxies superimposed upon the line of sight. The PACS photometry will be an invaluable too to aid discrimination between SEDs of galaxies and discs in the far infrared because the typical dust temperature of debris discs is in the region 50–150 K, whilst the temperature of galactic dust emission is ~ 20 K, such that debris disc emission will peak in the PACS bands, whilst galaxy emission will peak in the SPIRE bands. Alternatively, there may exist a class of very cold, very massive debris discs, previously undiscovered due to the poor resolution and low sensitivity of ground based searches, in which case the other *Herschel* debris discs programs should also uncover massive, cold debris discs around some of their targets (around 1% of stars, having discovered 6 likely candidates in a field with 549 TYC-2 stars).

Table 6.1: Table of the photometry for the 5 targets with matches within 5″ between the Tycho-2 and ATLAS catalogues (above the line) and the 14 further targets with positional matches within 10″ (below the line). Estimated photospheric fluxes are included for reference.

| Tycho-2 ID | Right Ascension [deg] | Declination [deg] | Offset [″] | SNR | $F_{ph}$[250] [mJy] | $F_{ph}$[350] [mJy] | $F_{ph}$[500] [mJy] | $F_{obs}$[250] [mJy] | $F_{obs}$[350] [mJy] | $F_{obs}$[500] [mJy] |
|---|---|---|---|---|---|---|---|---|---|---|
| TYC213-689-1 | 134.96527 | 0.07138 | 4.4 | 8.0 | 0.045 | 0.023 | 0.011 | 33.0 | 25.4 | 16.3 |
| TYC226-1569-1 | 136.18172 | 1.67984 | 3.1 | 6.0 | 0.0015 | 0.0008 | 0.0003 | 20.2 | 24.5 | 17.8 |
| TYC4879-168-1 | 137.74043 | -0.25206 | 0.6 | 8.6 | 0.007 | 0.003 | 0.002 | 35.3 | 32.0 | 25.0 |
| TYC4878-263-1 | 136.75604 | -0.37949 | 3.7 | 7.0 | 0.0010 | 0.0005 | 0.0002 | 29.0 | 31.9 | 14.7 |
| TYC4879-744-1 | 138.14085 | -0.76410 | 2.2 | 6.8 | 0.017 | 0.009 | 0.004 | 32.4 | 24.8 | 2.7 |
| TYC226-978-1 | 135.76667 | 0.18659 | 8.5 | 7.6 | 0.002 | 0.001 | 0.0006 | 20.9 | 29.6 | 22.5 |
| TYC226-1698-1 | 137.11893 | 0.90184 | 7.6 | 6.3 | 0.036 | 0.018 | 0.009 | 20.2 | 24.0 | 13.1 |
| TYC226-1788-1 | 137.00262 | 0.83386 | 8.8 | 6.5 | 0.005 | 0.003 | 0.001 | 14.0 | 21.2 | 20.8 |
| TYC226-1697-1 | 137.38967 | 1.62849 | 5.9 | 8.7 | 0.019 | 0.010 | 0.005 | 43.0 | 31.6 | 9.8 |
| TYC226-2344-1 | 136.31403 | 0.51431 | 5.3 | 16.3 | 0.004 | 0.002 | 0.001 | 96.7 | 60.6 | 23.3 |
| TYC227-1794-1 | 138.20949 | 0.32216 | 5.1 | 6.2 | 0.031 | 0.016 | 0.008 | 18.2 | 27.1 | 12.8 |
| TYC227-2347-1 | 138.74873 | 0.27601 | 9.3 | 7.4 | 0.008 | 0.004 | 0.002 | 54.2 | 37.3 | 17.5 |
| TYC213-867-1 | 134.49875 | 0.65735 | 8.1 | 6.4 | 0.002 | 0.001 | 0.0004 | 27.1 | 26.1 | 17.8 |
| TYC213-582-1 | 134.53686 | 1.12214 | 5.9 | 10.1 | 0.005 | 0.003 | 0.001 | 48.2 | 45.9 | 25.9 |
| TYC226-433-1 | 136.18646 | 1.88319 | 5.3 | 11.1 | 0.002 | 0.001 | 0.0006 | 42.3 | 49.0 | 28.5 |
| TYC226-597-1 | 135.81626 | 1.96693 | 8.5 | 7.7 | 0.007 | 0.003 | 0.002 | 31.3 | 29.6 | 18.9 |
| TYC226-1661-1 | 135.82157 | 1.87504 | 6.5 | 7.5 | 0.006 | 0.003 | 0.001 | 35.4 | 34.3 | 9.4 |
| TYC213-245-1 | 134.90621 | 1.76649 | 8.4 | 8.4 | 0.019 | 0.010 | 0.005 | 34.5 | 33.7 | 25.7 |
| TYC4878-548-1 | 135.89881 | -1.58174 | 9.6 | 7.8 | 0.006 | 0.003 | 0.002 | 37.5 | 28.4 | 16.0 |

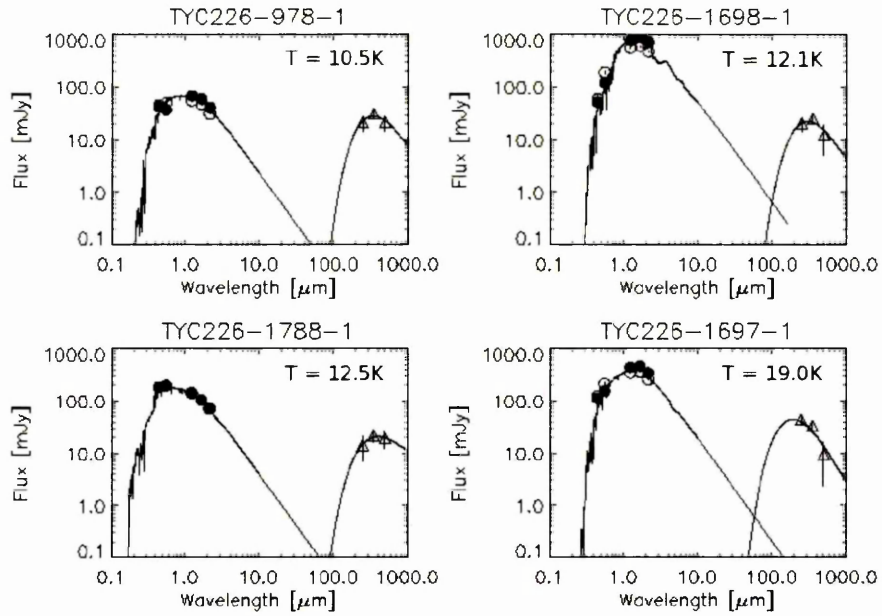


Figure 6.3: SEDs of the debris disc candidate stars from sources in the HATLAS field. The model stellar photosphere, fitted to the *JHK* photometry, has been scaled to the *H* band flux. Error bars are $1\sigma$.

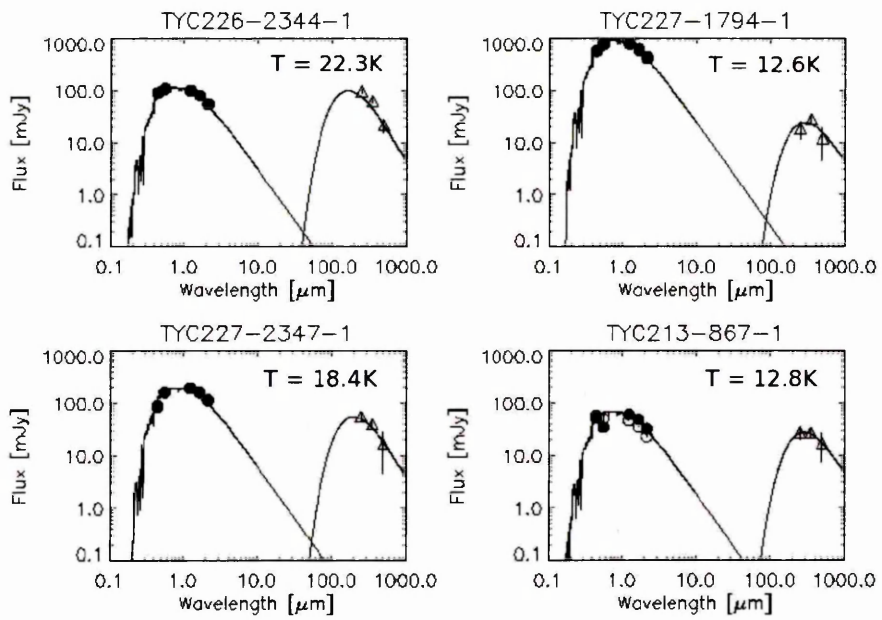


Figure 6.4: SEDs of the debris disc candidate stars from sources in the HATLAS field. The model stellar photosphere, fitted to the *JHK* photometry, has been scaled to the *H* band flux. Error bars are $1\sigma$.

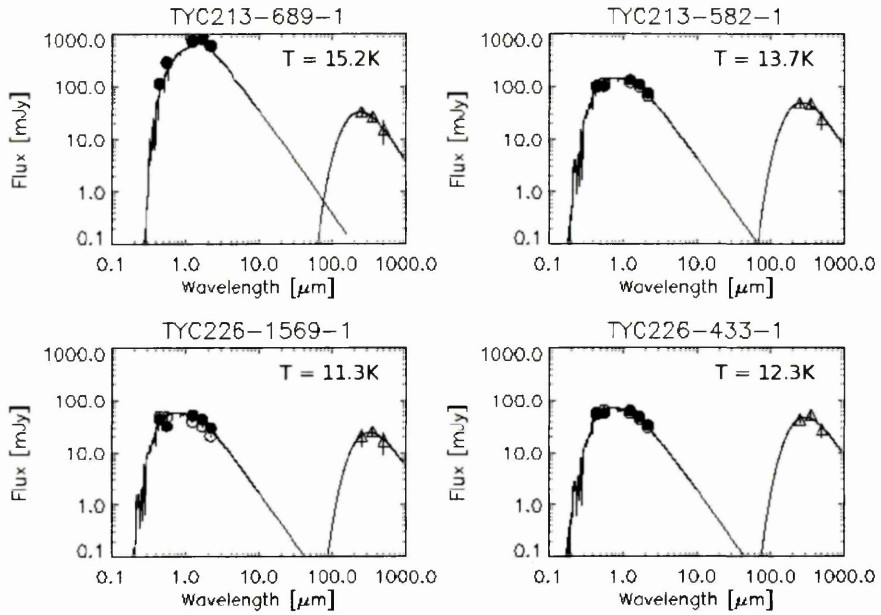


Figure 6.5: SEDs of the debris disc candidate stars from sources in the HATLAS field. The model stellar photosphere, fitted to the *JHK* photometry, has been scaled to the *H* band flux. Error bars are $1\sigma$.

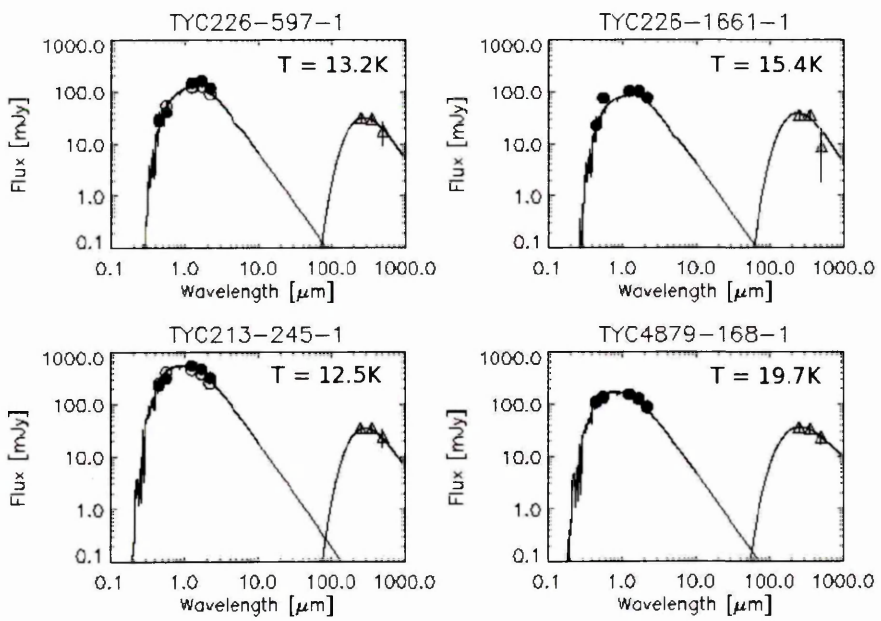


Figure 6.6: SEDs of the debris disc candidate stars from sources in the HATLAS field. The model stellar photosphere, fitted to the *JHK* photometry, has been scaled to the *H* band flux. Error bars are $1\sigma$.

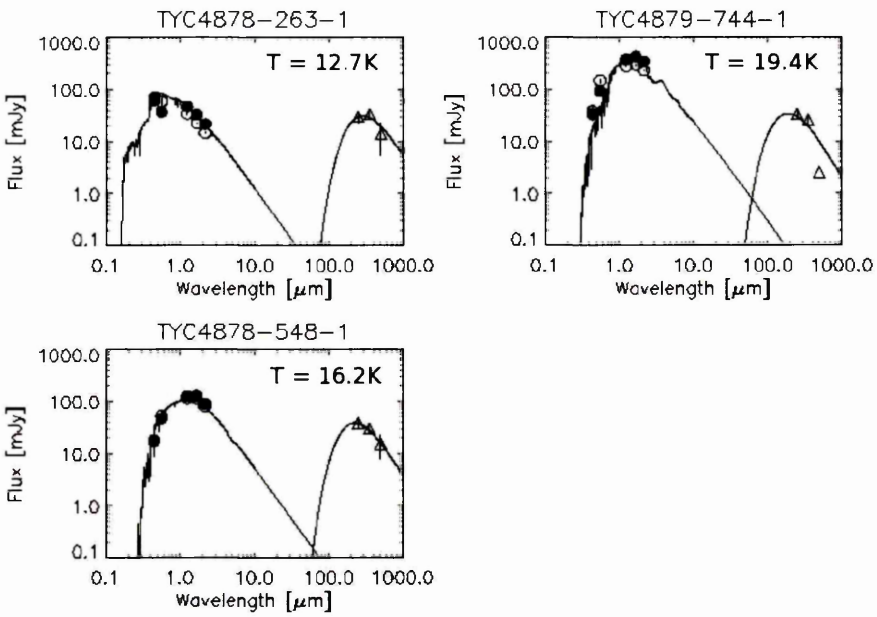


Figure 6.7: SEDs of the debris disc candidate stars from sources in the HATLAS field. The model stellar photosphere, fitted to the *JHK* photometry, has been scaled to the *H* band flux. Error bars are $1\sigma$.

Table 6.2: Table of the model parameters derived from fitting a single temperature black body model to the SPIRE photometry of the debris disc candidates. The best disc candidates from this work, based on the source separation, disc mass, stellar distance and fractional luminosity, are identified with their names in bold type.

| Tycho-2 ID | SpType | Right Ascension [°] | Declination [°] | Distance [pc] | Temperature [K] | $\tau$ [$\times 10^{-4}$] | Radius [AU] | Mass [$M_{\oplus}$] | $\chi^2$ | Model |
|---|---|---|---|---|---|---|---|---|---|---|
| TYC226-978-1 | G5V | 135.76667 | 0.18659 | 228 | 10.5 | 4.3 | 669 | 27.5 | 0.4 | grey |
| TYC226-1698-1 | M4V | 137.11893 | 0.90184 | 7 | 12.1 | 0.5 | 265 | 0.01 | 0.5 | grey |
| TYC226-1788-1 | F2V | 137.00262 | 0.83386 | 316 | 12.5 | 0.7 | 595 | 30.4 | 0.1 | black |
| **TYC226-1697-1** | K4V | 137.38967 | 1.62850 | 46 | 19.0 | 3.0 | 174 | 0.1 | 1.3 | grey |
| TYC226-2344-1 | F5V | 136.31403 | 0.51432 | 335 | 22.3 | 11.4 | 176 | 11.2 | 1.7 | grey |
| **TYC227-1794-1** | F5V | 138.20949 | 0.32216 | 120 | 12.6 | 0.2 | 553 | 2.7 | 1.7 | grey |
| TYC227-2347-1 | G0V | 138.74873 | 0.27602 | 198 | 18.4 | 5.1 | 234 | 4.2 | 0.1 | grey |
| TYC213-867-1 | F5V | 134.49875 | 0.65735 | 412 | 12.8 | 3.0 | 535 | 41.7 | 0.03 | grey |
| **TYC213-689-1** | K5V | 134.96527 | 0.07138 | 36 | 15.2 | 1.0 | 266 | 0.2 | 0.01 | grey |
| TYC213-582-1 | F8V | 134.53686 | 1.12215 | 254 | 13.7 | 3.4 | 446 | 19.4 | 0.5 | grey |
| TYC226-1569-1 | F8V | 136.18172 | 1.67984 | 353 | 11.3 | 3.5 | 656 | 42.5 | 0.1 | grey |
| TYC226-433-1 | F5V | 136.18646 | 1.88319 | 411 | 12.3 | 4.8 | 580 | 73.5 | 1.5 | grey |
| **TYC226-597-1** | K4V | 135.81626 | 1.96693 | 93 | 13.2 | 4.4 | 361 | 2.1 | 0.1 | grey |
| TYC226-1661-1 | K2V | 135.82157 | 1.87505 | 115 | 15.4 | 9.5 | 274 | 1.1 | 2.9 | grey |
| TYC213-245-1 | G2V | 134.90621 | 1.76649 | 90 | 12.5 | 0.8 | 495 | 3.0 | 0.01 | grey |
| TYC4879-168-1 | F8V | 137.74043 | -0.25206 | 248 | 19.7 | 3.1 | 216 | 8.3 | 0.02 | black |
| TYC4878-263-1 | A8V | 136.75604 | -0.37949 | 692 | 12.7 | 1.5 | 639 | 12.3 | 1.0 | grey |
| TYC4879-744-1 | M2V | 138.14085 | -0.76410 | 13 | 19.4 | 2.5 | 130 | 0.003 | 1.7 | grey |
| **TYC4878-548-1** | K2V | 135.89881 | -1.58174 | 129 | 16.2 | 7.9 | 248 | 2.1 | 0.1 | grey |

## 6.5 Conclusions

We have fitted 19 debris disc candidates with simple single temperature emission models, from which the disc fractional luminosity, dust temperature, dust radial location and dust mass have been derived. All of the candidates have fractional luminosities within the expected range for debris discs.

The discs of three of the candidates are well modelled by the single temperature disc model used here: TYC213-867-1 and TYC4878-548-1 (grey body) and TYC4879-168-1 (black body) all have $\chi^2 < 0.02$, a significance of $\sim 3\sigma$ for a $\chi^2$ test with 2 degrees of freedom. Of the targets identified as high quality candidates, three are poorly fitted by the single temperature model. A model using a simple power law particle size distribution will be part of the follow up to this initial search.

Those discs with model dust temperatures > 20 K require PACS 100 and 160 $\mu$m photometry in order to constrain the peak of the disc SED, since the fitted disc SED peaks shortward of the region covered by the SPIRE photometry. If, as expected, warmer temperatures are derived for the discs with the addition of the far infrared data, the disc masses will be reduced, bringing them more in line with the expected masses of debris discs.

If the field analysed here proves typical, It is possible that the H-ATLAS program may observe >100 debris discs, similar to the number expected from the DEBRIS OTKP (one of several *Herschel* key programs devoted to debris disc science, see Augereau et al., 2008), providing a complementary data set of fainter and more distant objects to the bright, nearby stars that are the focus of e.g. DEBRIS and DUNES.

The disc candidates presented here have properties (mass, fractional luminosity) that are consistent with known discs, e.g. $q^1$ Eridani, $\beta$ Pictoris, but with lower temperatures, implying absence of smaller dust grains in these discs or much larger orbital radii than typical debris discs. An example of a dust disc with large grains might be found in the rings of Saturn, which are stable over Gyr timescales and have very few small dust grains (Esposito, 2002). Such

a system has been identified as a possible debris disc configuration by Heng and Tremaine (Heng & Tremaine, 2010). The disc formation history, and the clearing mechanism that keeps grains from the inner area of the system (and therefore producing warmer emission) remain unknown, however. Preliminary results from DUNES imply the existence of debris discs with cold excesses, but at much lower fractional luminosities ($\sim 10^{-6}$) and peaking at 160 $\mu$m rather than 250 or 350 $\mu$m as is the case here (Marshall et al., in prep.). We have not observed any cold discs similar to the ones presented here amongst the sample of nearby stars in DUNES (having observed 70 of 133 targets), implying that these discs are extremely rare objects. We note however that these cold, massive discs occupy the region of discovery space that was to be exploited by *Herschel*, being previously unobservable due to sensitivity or resolution requirements.

We note that none of the debris disc candidates identified in this work are presented in the published paper discovering these cold, massive discs: Thompson et al. (2010). The methodology applied in their paper is slightly different to our own, basing their identification of stars in the SPIRE field on a cross-correlation between point sources in the SDSS DR7 (Smith D., 2010 submitted) and the SPIRE catalogue, and applying a distance cut based on the near infrared colours to identified matches. Having quantified the chance alignment probability as a function of source separation using a Monte Carlo method, the probability of true matches between the wavelengths of sources identified in their paper lie at $\sim 0.8$, whilst the ones identified in this work lie around $\sim 0.5$. Further analysis of a larger sample of stars is required to understand at what level the cut-off between reliable association and background contamination can be made, which will be the subject of follow-up work on the other HATLAS fields. The three (two published, one subsequently identified) cold disc candidates from this field are the subject of shorter wavelength follow-up observations by *Herschel*/PACS to better constrain their SEDs and look for resolved emission to constrain the size of these discs.

# 7

# Dynamical Simulations of HR8799

## 7.1 Introduction

Since the discovery of 51 Pegasi b, the first exoplanet orbiting a main sequence star (Mayor & Queloz, 1995), an ever-growing menagerie of planets has been found beyond our Solar System. Initially, the great bulk of these were discovered using the Radial Velocity method (Jones, 2008), which preferentially finds massive planets orbiting close to their parent stars. As time has passed and technology improved, new methods have been developed which allow the employment of more efficient search strategies, such as Gravitational Micro-lensing (Sumi, 2009) and Transits detection, for instance by the Wide Angle Search for Planets (Pollacco et al., 2006, WASP, ). These methods allow for millions of potential host stars to be surveyed simultaneously.

The number of known exoplanets now exceeds 400, but each detection technique has observational biases which limit the usefulness of this sample in aiding our understanding of the true population of extrasolar planets. Both the Radial Velocity and Transit Detection methods favour the detection of massive planets located close to their parent stars, while Gravitational Micro-lensing preferentially detects planets with larger orbital radii. In addition, Micro-lensing planets are detected by means of only a single series of observations (or "lensing event"),

which severely limits the information that can be gathered on such systems, since follow-up observations are impossible (Sumi, 2009).

The first confirmed discoveries of directly imaged exoplanets were announced in late 2008 (Kalas et al., 2008; Marois et al., 2008). Whilst the techniques detailed above often favour the discovery of planets with small semi-major axes, direct imaging favours the observation of planets that orbit much further from their parent stars. As such, this method provides a new window on the formation and evolution of planetary systems, and may, in the coming years, provide the first unbiased statistics of the exoplanetary population.

Of the two directly imaged systems announced in late 2008, the planets of HR8799 evoked the most excitement. Extensive discussion on both the observed planet properties (Fabrycky & Murray-Clay, 2010; Goździewski & Migaszewski, 2009) and the accompanying dust disc (Reidemeister et al., 2009; Su et al., 2009) was to follow.

HR8799 is believed to be a young star with an estimated age of 20–160 Myr (Moór et al., 2006). Significantly more luminous and more massive than our Sun (spectral type A5V), it lies at a distance of 39.9 pc (van Leeuwen, 2007). Identified as having an infra-red excess by *IRAS* (Chen et al., 2009), the star seemed an obvious candidate for young exoplanets. In 2008, near-infrared imaging of the system revealed a family of three giant planets, each believed to be significantly more massive than Jupiter (Marois et al., 2008, hereafter M08). Following the discovery, archived observations from both the Hubble Space Telescope (Lafrenière et al., 2009) and Subaru (Fukagawa et al., 2009) were analysed, yielding images which allowed the orbital motion of the planets to be extrapolated back to 1998; thereby providing confirmation of the orbital parameters over longer timescales than those derived in M08.

The stability of the HR8799 planetary system has since been subjected to a significant amount of scrutiny. Observations carried out by *Spitzer* (Su et al., 2009) identified three discrete components of the system's debris disc - a broad region of warm dust ($T \sim 150\ K$) orbiting closer to the parent star than the innermost planet; a broad disk of cold dust ($T \sim 45\ K$) with a sharp inner edge beyond the orbit of the outermost planet; and a marked halo of small dust

grains thought to originate within the cold dust belt. The large amounts of short lived dust in the system has been presented as evidence that the planetary system could be experiencing significant dynamical instability: such instability would cause rapid stirring within the circumstellar disc (particularly by the outermost planet) and the resultant depletion is a likely explanation of the observed structure. This scenario resembles models put forward to explain the "Late-Heavy Bombardment" (LHB) of the terrestrial planets in our own Solar System, which is postulated to have occured some ~700 Myr after formation (Gomes et al., 2005; Morbidelli & Levison, 2006).

It is clear, therefore, that HR8799 is a particularly interesting system, much deserving of significant further study. Dynamical studies carried out by other authors (Fabrycky & Murray-Clay, 2010; Goździewski & Migaszewski, 2009) have suggested that the system may be highly unstable. The most long lived configuration of planets found in those works requires that both the inner- and outer-most pairs of planets each lie close to their mutual 2:1 mean-motion resonances (hereafter MMR), raising the intriguing possibility that the system is actually trapped in a Laplace resonance (1:2:4), much like the orbits of Io, Europa and Ganymede about Jupiter. Even when the planets are placed in such a configuration, the authors still find the system to be unstable on timescales shorter than that of the estimated stellar lifetime for a broad range of planetary masses and orbital inclinations. If such a resonant scenario is verified, this would make HR8799 the first known exoplanetary system containing two pairs of planets in a mutually resonant configuration.

Previous work has concentrated on investigating the impact of the planetary masses and their orbital separations on their dynamical stability and has studied variations in the individual planetary masses and the inclination of the system. Here, we take an alternative approach, assuming that the HR8799 system is presented face-on and taking the planetary masses to be those derived photometrically in M08. We then investigate the stability of the system as a function of the eccentricity and semi-major axes of the planetary orbits.

## 7.2 Description of Dynamical Model

The N-body dynamics package *MERCURY* (Chambers, 1999) has been successfully employed in fields such as the accretion and hydration of terrestrial planets (e.g. Chambers, 2001; Fogg & Nelson, 2005), the detailed dynamics of small bodies in the outer Solar system (e.g. Horner et al., 2004; Lykawka et al., 2009) and even the dynamics of exoplanets in multiple star systems (e.g. Ford et al., 2005; Raymond et al., 2008). The Hybrid integrator within the package offers an ideal compromise between accurate dynamical integration and simulation time. This is the result of a clever switching algorithm which allows the integration to be carried out by a symplectic integrator (which is very fast, but can become inaccurate during close encounters between test particles) when objects are widely separated, but calculates all close encounters using a much more accurate (but slower) Bulrisch-Stoer integrator. In this work, we use *MERCURY*'s hybrid integrator to simulate the dynamical evolution of the three planet HR8799 system over a 1 Myr period.

Using the observed orbital radii and photometric masses from M08 as a starting point for our calculations (as detailed in Table 1), we created 119,070 independent dynamical integrations, each following the evolution of one particular planetary architecture for a period of one million years. The orbital radius of the middle planet (HR8799c, 38 AU) was held constant throughout, while the radii of the inner (HR8799d, 24 AU) and outer (HR8799b, 68 AU) planets were systematically varied in 0.15 AU steps over a range spanning ± 1.5 AU from the nominal orbit, giving a total of 21 possible initial radial locations for the inner and outer planets. All combinations of these parameters were tested, giving a total of $21^2 = 441$ initial semi-major axis architectures. On top of this, the eccentricity of each planet was varied to simulate initial orbits of low (0.01), moderate (0.08) and high (0.2) eccentricity. Employing all possible combinations of semi-major axis and eccentricity produced a total of 11,907 different architectures of the system for consideration. For each architecture, ten independent integrations were performed, in which the initial location of the each planet upon its orbit, as determined by their

mean anomaly, $M$, was randomly assigned in the range 0 - 360°, to produce ten independent trials of each scenario. In each integration the fate of the planet was followed: whether it survived until completion of the run; collided with another planet; or was ejected from the system. Regardless of collisions/ejections, each integration ran for a period of 1 Myr.

The ensemble of simulations was set up and run sequentially using an IDL script written by Andrew James Carter, and formatted to run on the OU IMPACT cluster with the assistance of Geoff Bradshaw.

The output from the dynamical simulations were first processed from compressed binary format into ASCII tables of planetary orbital elements ($a$,$e$,$i$) using specific FORTRAN code written by Jonathan Horner. These raw tables of orbital elements for each simulation were then collated and indexed to create plots of stability, planetary survival and estimated system lifetime. The output stability plots and histograms were produced using an IDL pipeline written by the author.

The planetary lifetimes in each simulation were extracted from the events log of each simulation, recording the fate (survival; collision with star/planet; or ejection) and when that fate occurred. An exponential decay curve fitted to the ten iterations of each set of initial conditions was used to calculate a "stability lifetime" for that set of conditions. Some of the eccentricity combinations produced architectures where all ten iterations were stable for the full period of integration. In these cases the simulations were tested for stability by comparing the initial and final orbital radii and eccentricities.

## 7.3 Results

The following figures (Fig. 7.1 – 7.27 inclusive) illustrate the mean lifetime for each combination of initial $a$ and $e$ averaged over all ten iterations. From these figures it is clear that our dynamical simulations show several clear trends. As would be expected, an increase in eccentricity results in a decrease in system stability; resulting from the heightened frequency of close

Table 7.1: A summary of HR8799's properties and system parameters used in the model grid, as estimated by M08.

| Object | Parameter | Value |
|---|---|---|
| HR8799 | Mass | $1.5 \pm 0.3$ $M_{\odot}$ |
| | Radius | $1.5$ $R_{\odot}$ |
| | Spectral Type | A5V |
| | Age | $60 \pm {}^{100}_{30}$ Myr |
| Planet | | |
| d | Mass | $7 \pm {}^{4}_{2}$ $M_{jup}$ |
| | Orbital Radius | $24 \pm 3$ AU |
| c | Mass | $10 \pm 3$ $M_{jup}$ |
| | Orbital Radius | 38 AU |
| b | Mass | $10 \pm 3$ $M_{jup}$ |
| | Orbital Radius | $68 \pm 3$ AU |

approach events between two planets at high eccentricities. At low eccentricities, the system is typically stable for the full duration of our simulation over the entire dynamical phase space. This is an interesting result, as previous studies (Fabrycky & Murray-Clay, 2010; Marois et al., 2008) showed that the system was dynamically unstable with circular orbits on the timescale of $< 150{,}000$ yrs for planets with the observed masses and orbital radii. This implies that a small amount of initial eccentricity in the planetary orbits has a stabilising effect on the system.

We find that the stability of the system to be dominated by the inner pair of planets, as evidenced from the strong vertical structure in the stability plots (see particularly Fig. 7.3 and Fig. 7.19). This would be expected, since the timescale for dynamical evolution is shorter for these planets, as their smaller orbital periods cause them to undergo more encounters than the outer pair. The inner pair of planets are more stable for all combinations of eccentricity when the initial orbital radius of the inner planet is located inside the MMR, implying that the 1:2 MMR has a stabilising effect on the orbit of the inner-most planet. The 1:2 MMR between the inner planets is therefore the region of greatest stability for the system.

There is no strong indication that the outer pair of planets have an appreciable effect on system stability. This may be a result of the short (compared to the system lifetime) duration of the integrations we have run here, or a reflection of the relatively weak influence of the

outer-most planet on the much closer inner two (orbiting at 24, 38 and 68 AU, respectively).

In several cases (see e.g. Fig. 7.1 and 7.14) the stability plots are broadly featureless, implying that the system appears, at first glance, to be stable for the full 1 Myr run time of the simulation. To test this result, we compared the initial and final orbital radii and eccentricity of the three planets for each simulation that was stable for the full 1 Myr. From plots of the ratio of the initial to final orbital radii (see Fig. 7.3 – 7.3), we find that there is a general trend for the eccentricities to increase over the period of the simulation, but that is to be expected as the planets perturb each other. The distribution of the fractional change in orbital radius in systems where none of the planets have a high initial eccentricity are distributed closely around the initial value. This is consistent with the planets occupying stable orbits within the orbital range expected from the planet's eccentricity, implying that these system architectures are stable on timescales much longer than 1 Myr (see Figs 7.4 and 7.4).

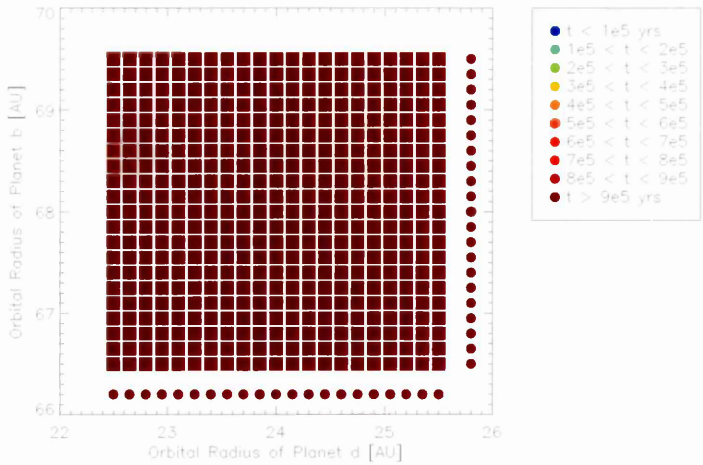


Figure 7.1: Plot of the HR8799 parameter space with all three planets with low initial eccentricities. The outlying circles represent the mean survival time for the configurations on each row/column as appropriate.

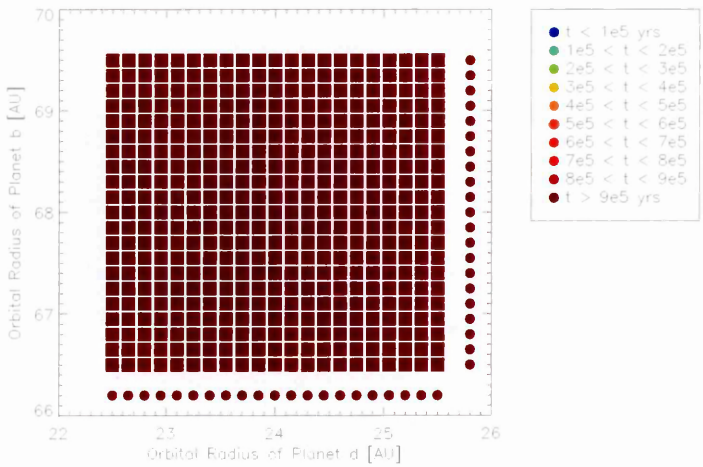


Figure 7.2: Plot of the HR8799 parameter space with the inner two planets with low initial eccentricity and the outer planet with medium initial eccentricity. The outlying circles represent the mean survival time for the configurations on each row/column as appropriate.

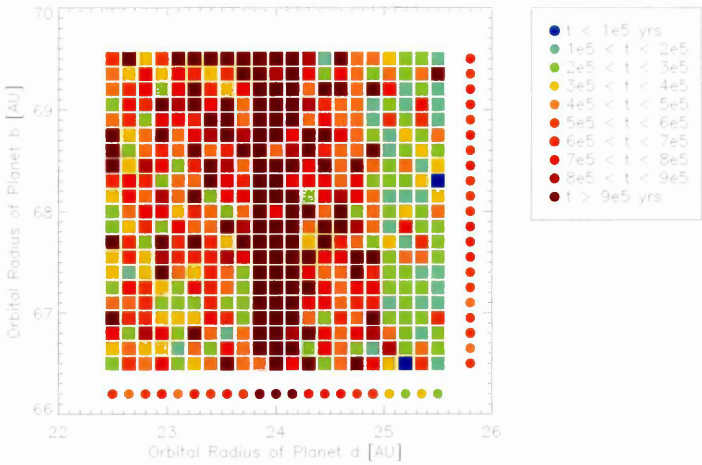


Figure 7.3: Plot of the HR8799 parameter space with the outer two planets with low initial eccentricity and the inner planet with high initial eccentricity. The outlying circles represent the mean survival time for the configurations on each row/column as appropriate.

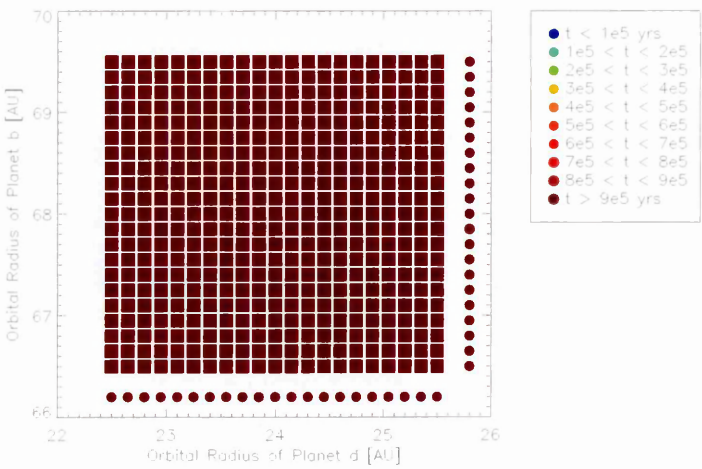


Figure 7.4: Plot of the HR8799 parameter space with the inner and outer planets with low initial eccentricities, and the middle planet with medium initial eccentricity. The outlying circles represent the mean survival time for the configurations on each row/column as appropriate.

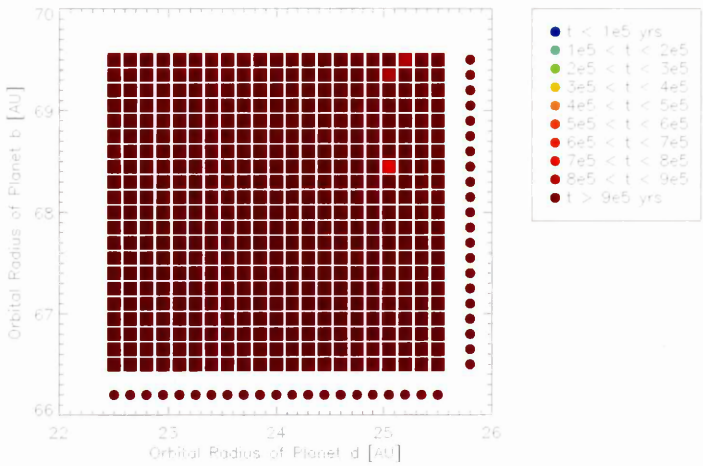


Figure 7.5: Plot of the HR8799 parameter space with the outer planet with low initial eccentricity and the inner two planets with medium initial eccentricity. The outlying circles represent the mean survival time for the configurations on each row/column as appropriate.

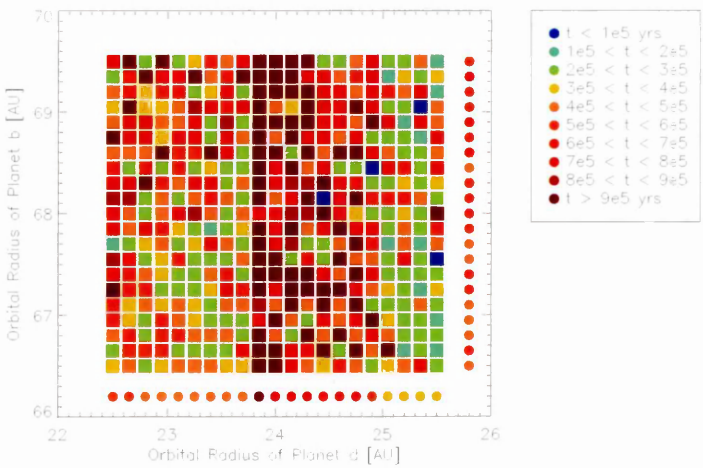


Figure 7.6: Plot of the HR8799 parameter space with the inner, middle and outer planets with high, medium and low initial eccentricity, respectively. The outlying circles represent the mean survival time for the configurations on each row/column as appropriate.

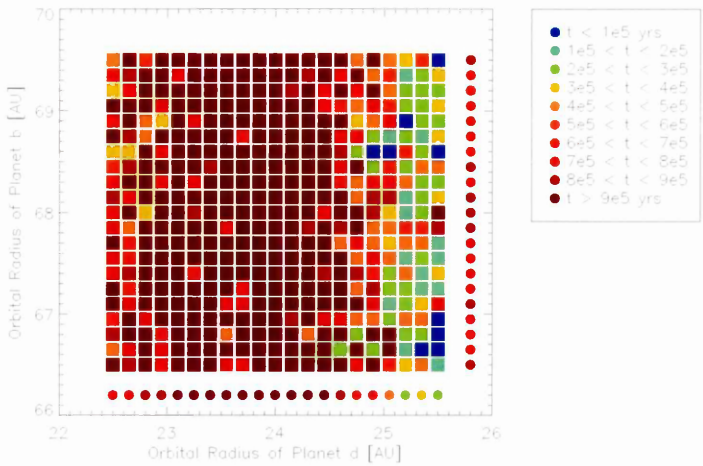


Figure 7.7: Plot of the HR8799 parameter space with the inner and outer planets with low inital eccentricity and the middle planet with high initial eccentricity. The outlying circles represent the mean survival time for the configurations on each row/column as appropriate.

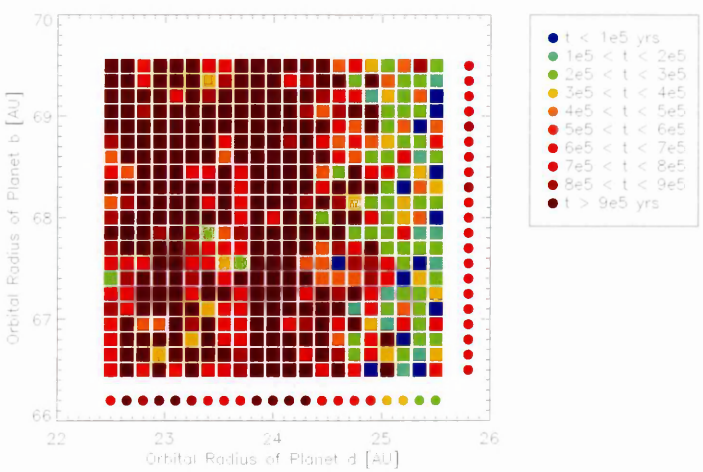


Figure 7.8: Plot of the HR8799 parameter space with the inner, middle and outer planets with medium, high and low initial eccentricity, respectively. The outlying circles represent the mean survival time for the configurations on each row/column as appropriate.

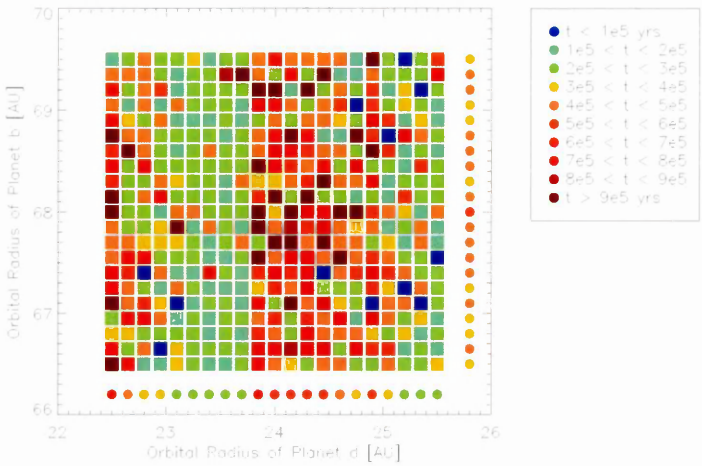


Figure 7.9: Plot of the HR8799 parameter space with the outer planet with low eccentricity and the inner two planets with high initial eccentricities. The outlying circles represent the mean survival time for the configurations on each row/column as appropriate.

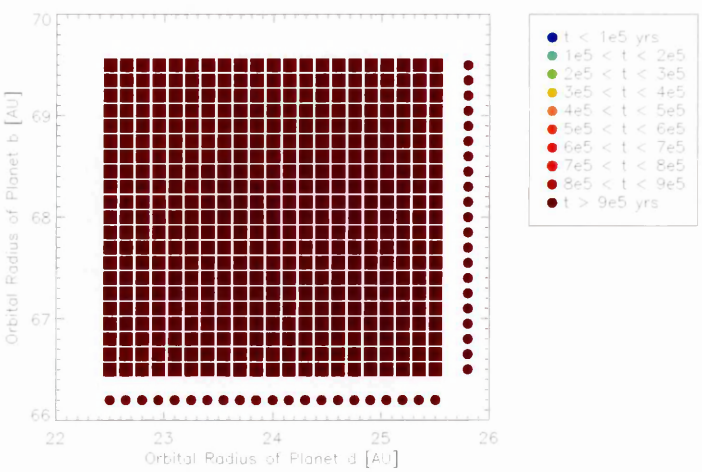


Figure 7.10: Plot of the HR8799 parameter space with the outer planet medium eccentric and the inner two planets with low initial eccentricities. The outlying circles represent the mean survival time for the configurations on each row/column as appropriate.

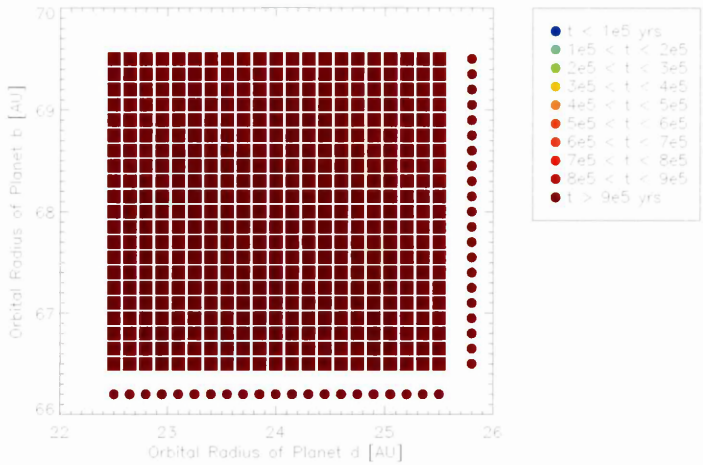


Figure 7.11: Plot of the HR8799 parameter space with the inner and outer planets with medium initial eccentricities and the middle planet with low initial eccentricity. The outlying circles represent the mean survival time for the configurations on each row/column as appropriate.

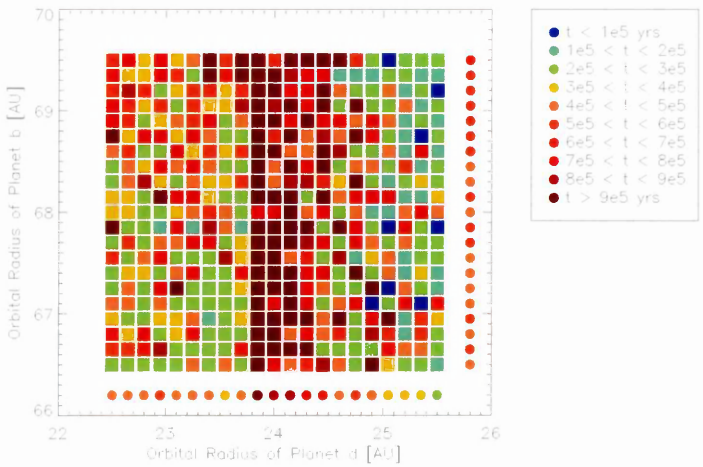


Figure 7.12: Plot of the HR8799 parameter space with the inner, middle and outer planets with high, low and medium initial eccentricities, respectively. The outlying circles represent the mean survival time for the configurations on each row/column as appropriate.

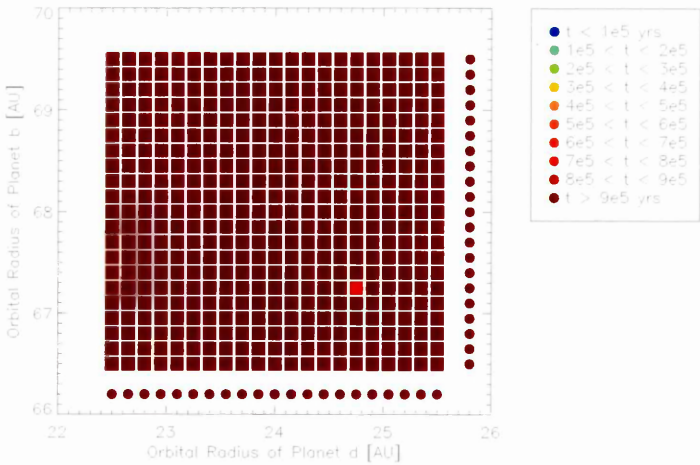


Figure 7.13: Plot of the HR8799 parameter space with the outer and middle planet with medium initial eccentricity and the inner planet with low initial eccentricity. The outlying circles represent the mean survival time for the configurations on each row/column as appropriate.

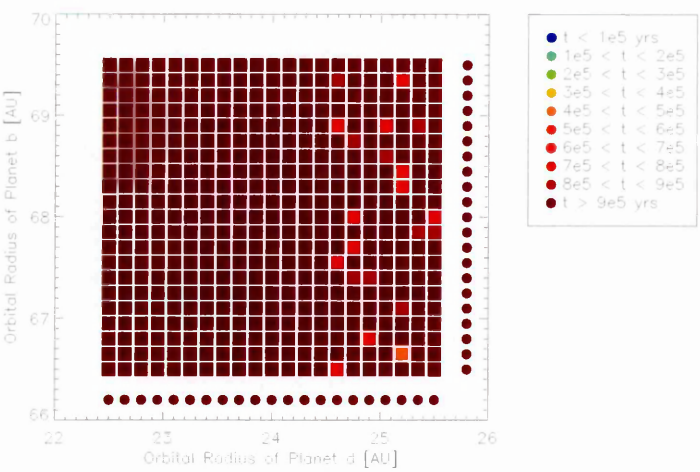


Figure 7.14: Plot of the HR8799 parameter space with all three planets with medium initial eccentricity. The outlying circles represent the mean survival time for the configurations on each row/column as appropriate.

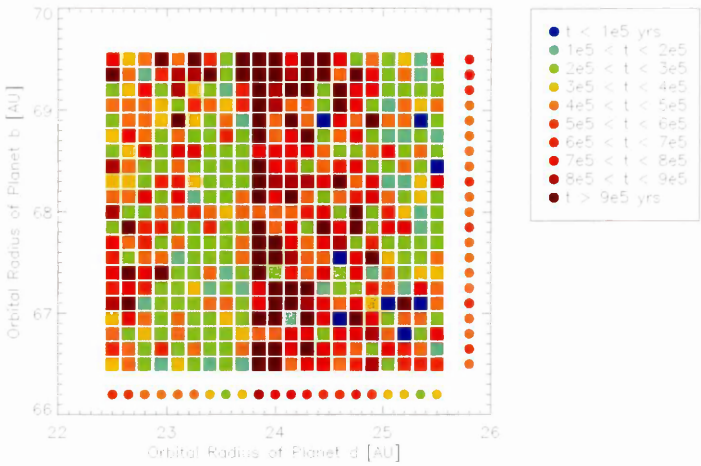


Figure 7.15: Plot of the HR8799 parameter space with the outer and middle planets with medium initial eccentricity and the inner planet with high initial eccentricity. The outlying circles represent the mean survival time for the configurations on each row/column as appropriate.

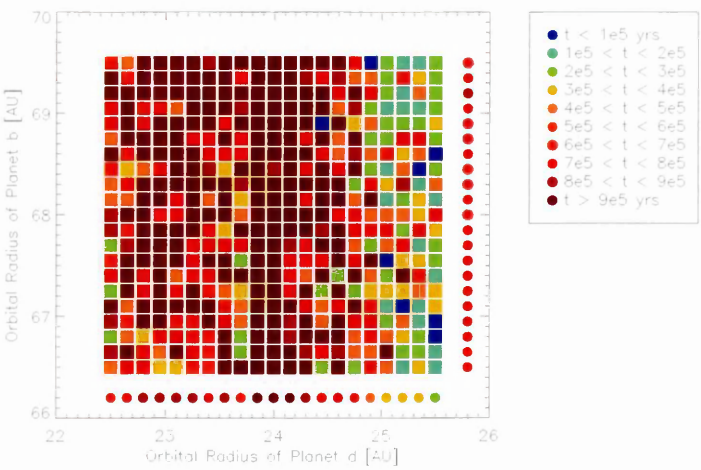


Figure 7.16: Plot of the HR8799 parameter space with the inner, middle and outer planets with low, high and medium initial eccentricity, respectively. The outlying circles represent the mean survival time for the configurations on each row/column as appropriate.

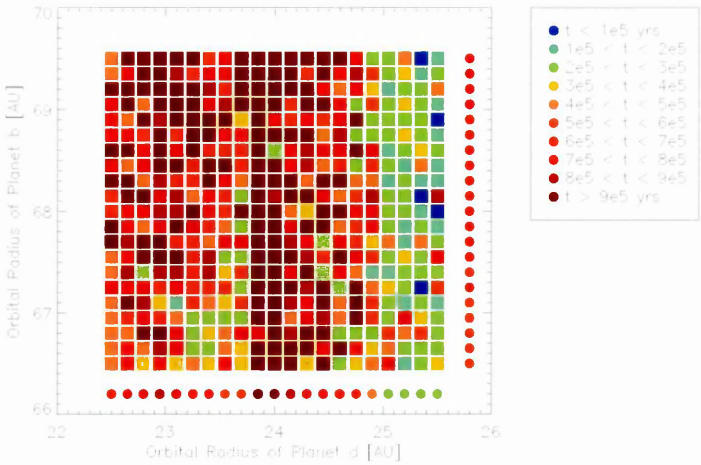


Figure 7.17: Plot of the HR8799 parameter space with the inner and outer planet with medium initial eccentricity and the middle planet with high initial eccentricity. The outlying circles represent the mean survival time for the configurations on each row/column as appropriate.

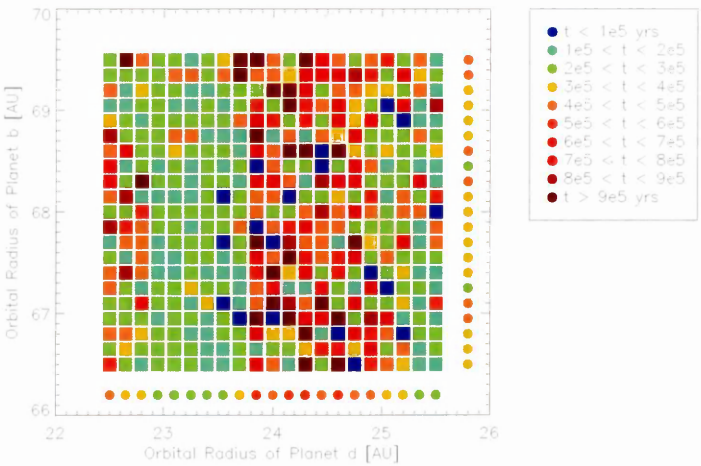


Figure 7.18: Plot of the HR8799 parameter space with the outer planet with medium initial eccentricity and the inner two planets with high initial eccentricities. The outlying circles represent the mean survival time for the configurations on each row/column as appropriate.

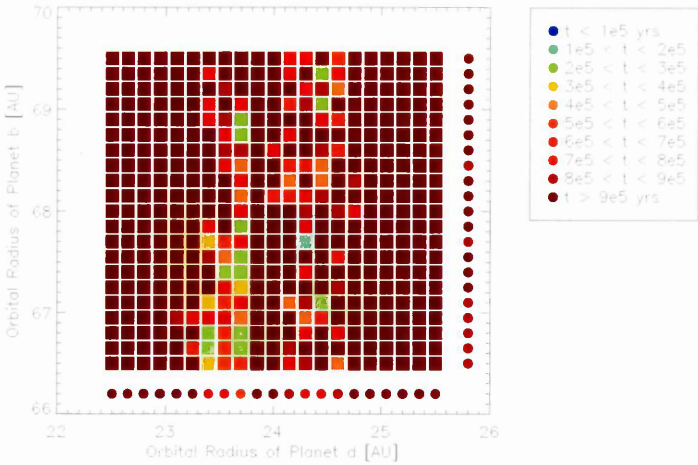


Figure 7.19: Plot of the HR8799 parameter space with the outer planet highly eccentric and the inner two planets with low initial eccentricities. The outlying circles represent the mean survival time for the configurations on each row/column as appropriate.

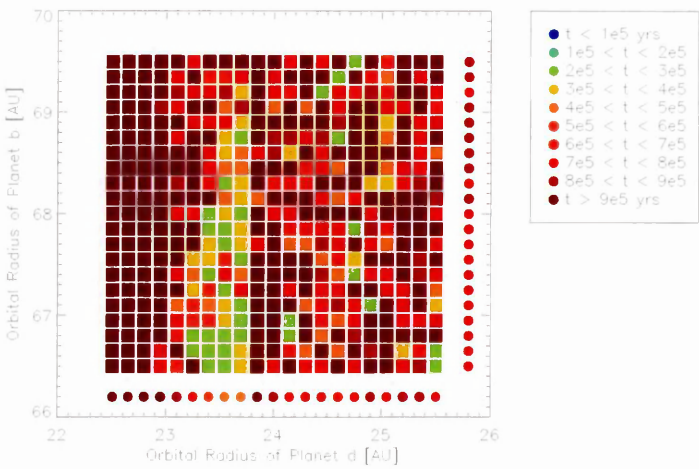


Figure 7.20: Plot of the HR8799 parameter space with the inner, middle and outer planets with medium, low and high initial eccentricity, respectively. The outlying circles represent the mean survival time for the configurations on each row/column as appropriate.

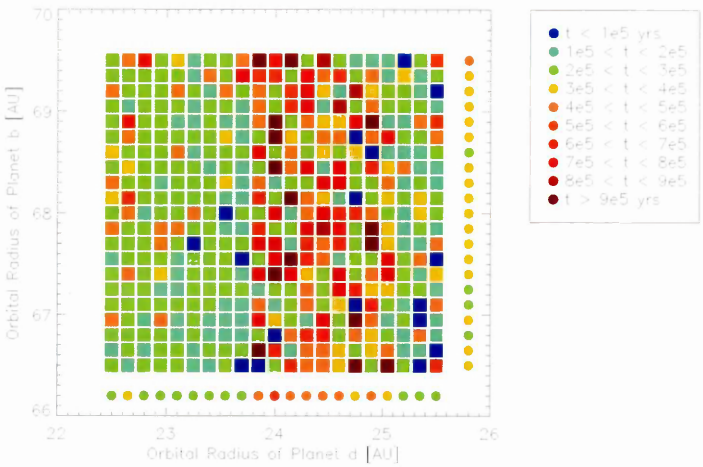


Figure 7.21: Plot of the HR8799 parameter space with the inner and outer planets with high initial eccentricities and the middle planet with low initial eccentricity
. The outlying circles represent the mean survival time for the configurations on each row/column as appropriate.

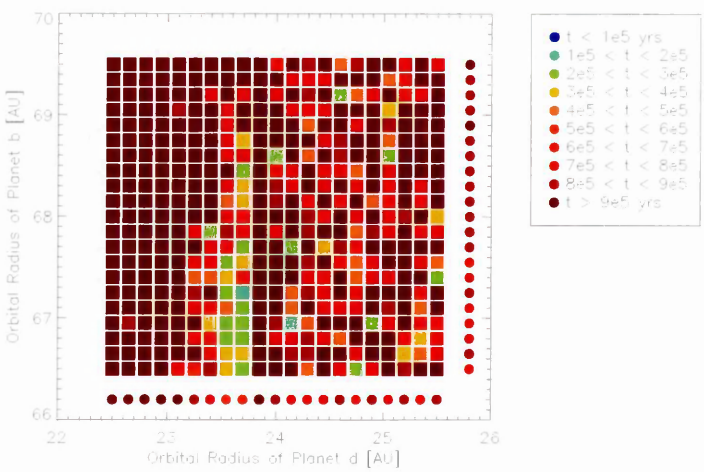


Figure 7.22: Plot of the HR8799 parameter space with the inner, middle and outer planets with low, medium and high eccentricities, respectively. The outlying circles represent the mean survival time for the configurations on each row/column as appropriate.

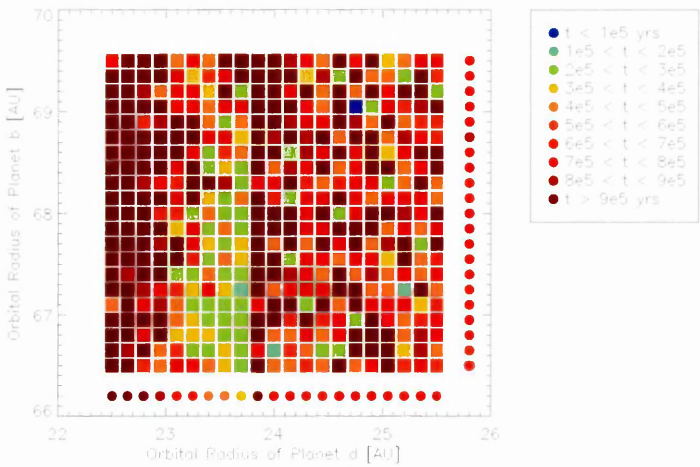


Figure 7.23: Plot of the HR8799 parameter space with the outer planet with high eccentricity and the inner two planets with medium eccentricity. The outlying circles represent the mean survival time for the configurations on each row/column as appropriate.

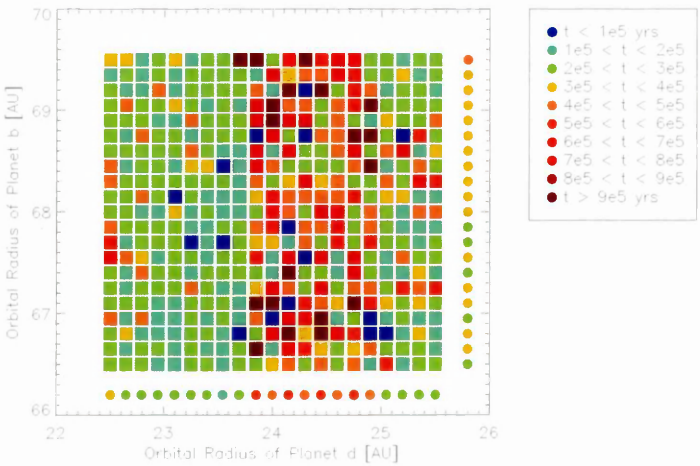


Figure 7.24: Plot of the HR8799 parameter space with the inner and outer planets with high eccentricity and the middle planet with medium eccentricity. The outlying circles represent the mean survival time for the configurations on each row/column as appropriate.

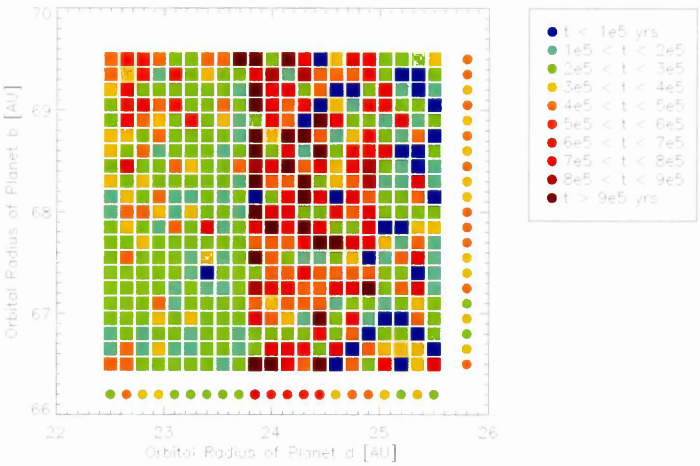


Figure 7.25: Plot of the HR8799 parameter space with the outer and middle planets highly eccentric and the inner planet low initial eccentricity. The outlying circles represent the mean survival time for the configurations on each row/column as appropriate.

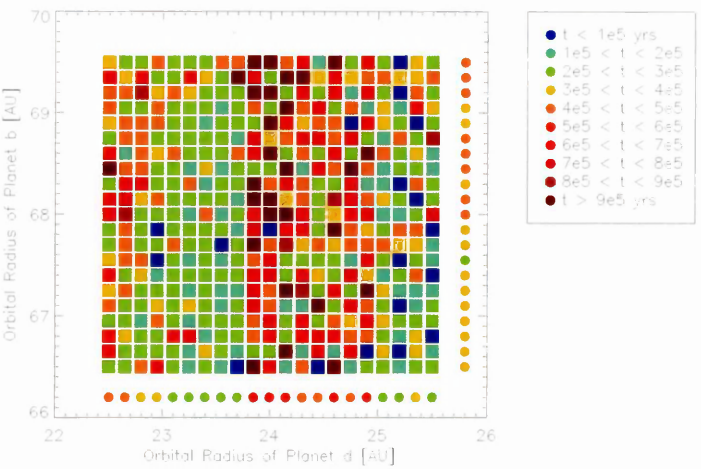


Figure 7.26: Plot of the HR8799 parameter space with outer and middle planets with high initial eccentricity and the inner planet with medium initial eccentricity. The outlying circles represent the mean survival time for the configurations on each row/column as appropriate.

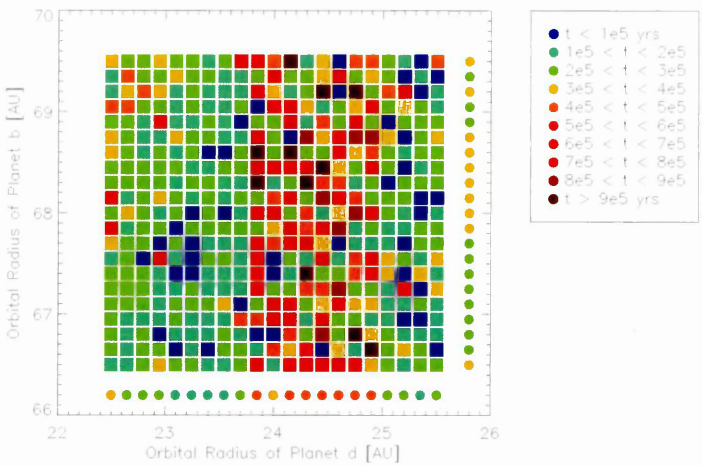


Figure 7.27: Plot of the HR8799 parameter space with all three planets with high initial eccentricities. The outlying circles represent the mean survival time for the configurations on each row/column as appropriate.

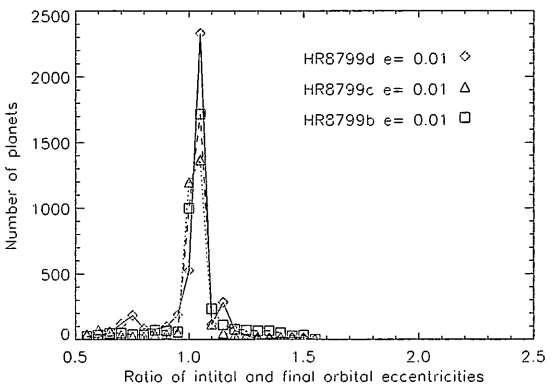
HR8799d e= 0.01
HR8799c e= 0.01
HR8799b e= 0.01
Number of planets
Ratio of intital and final orbital eccentricities

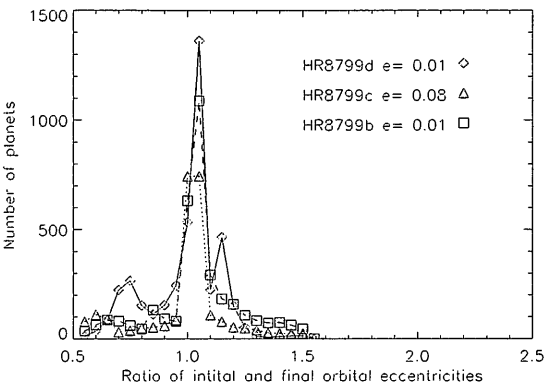
HR8799d e= 0.01
HR8799c e= 0.08
HR8799b e= 0.01
Number of planets
Ratio of intital and final orbital eccentricities

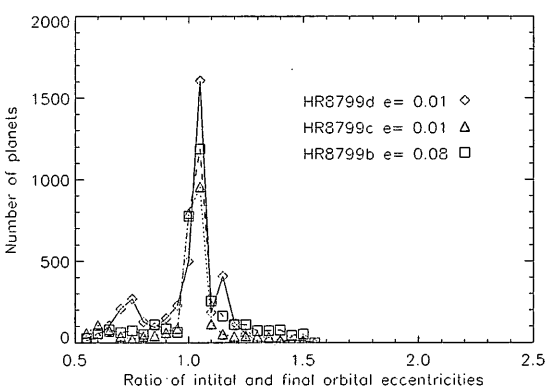
HR8799d e= 0.01
HR8799c e= 0.01
HR8799b e= 0.08
Number of planets
Ratio of intital and final orbital eccentricities

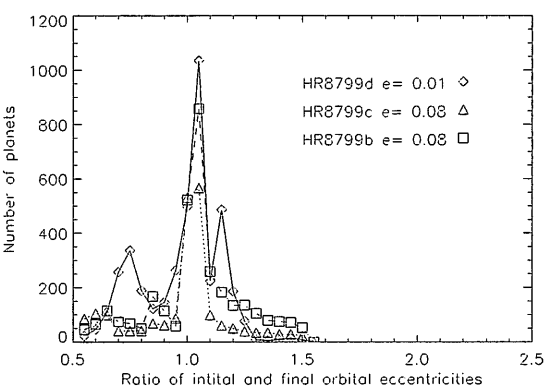
HR8799d e= 0.01
HR8799c e= 0.08
HR8799b e= 0.08
Number of planets
Ratio of intital and final orbital eccentricities

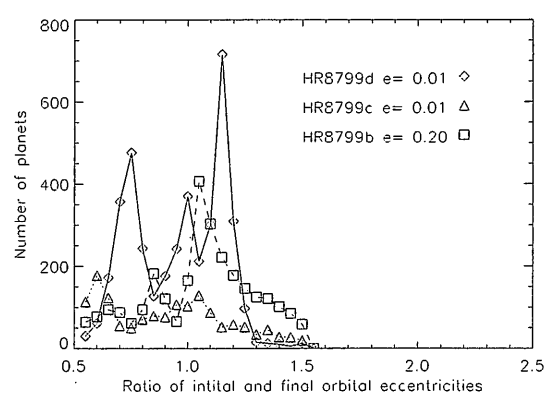
HR8799d e= 0.01
HR8799c e= 0.01
HR8799b e= 0.20
Number of planets
Ratio of intital and final orbital eccentricities

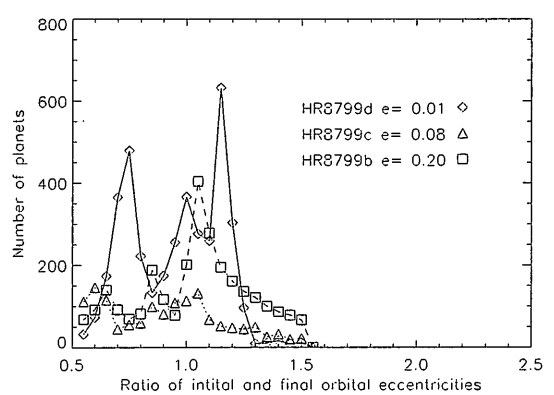
HR8799d e= 0.01
HR8799c e= 0.08
HR8799b e= 0.20
Number of planets
Ratio of intital and final orbital eccentricities

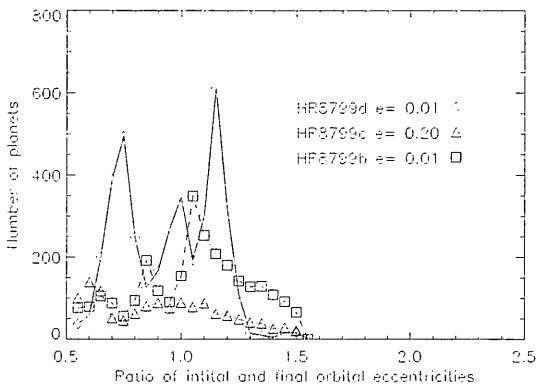
HR8799d e= 0.01
HR8799c e= 0.20
HR8799b e= 0.01
Number of planets
Ratio of intital and final orbital eccentricities

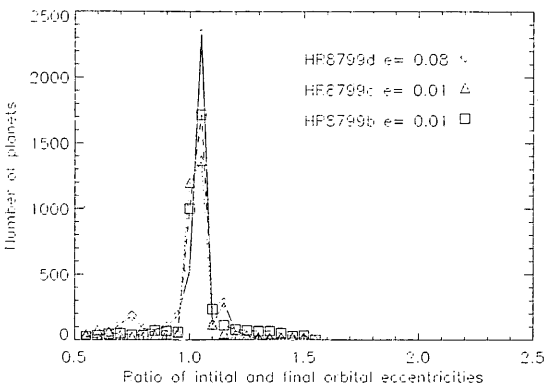
HR8799d e= 0.08
HR8799c e= 0.01
HR8799b e= 0.01
Number of planets
Ratio of intital and final orbital eccentricities

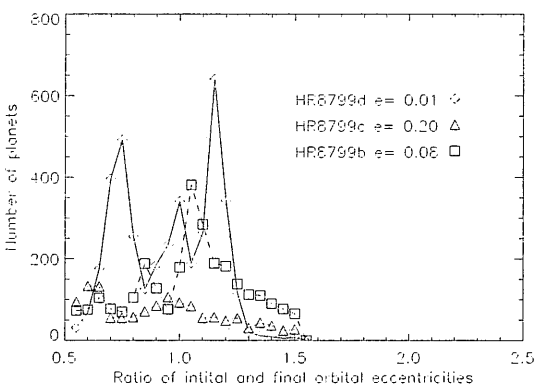
HR8799d e= 0.01
HR8799c e= 0.20
HR8799b e= 0.08
Number of planets
Ratio of intital and final orbital eccentricities

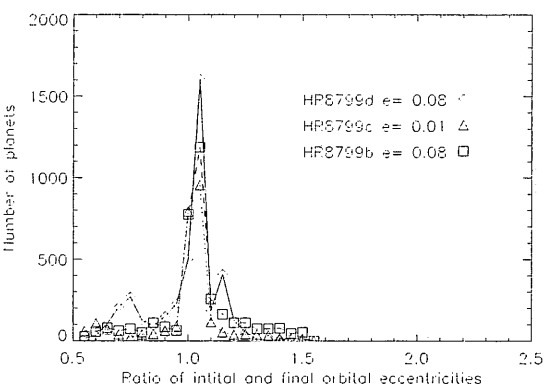
HR8799d e= 0.08
HR8799c e= 0.01
HR8799b e= 0.08
Number of planets
Ratio of intital and final orbital eccentricities

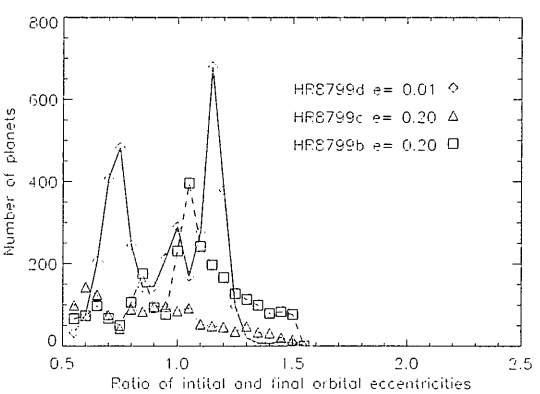
HR8799d e= 0.01
HR8799c e= 0.20
HR8799b e= 0.20
Number of planets
Ratio of intital and final orbital eccentricities

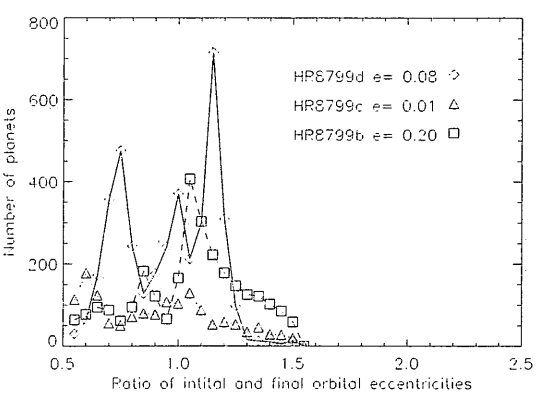
HR8799d e= 0.08
HR8799c e= 0.01
HR8799b e= 0.20
Number of planets
Ratio of intital and final orbital eccentricities

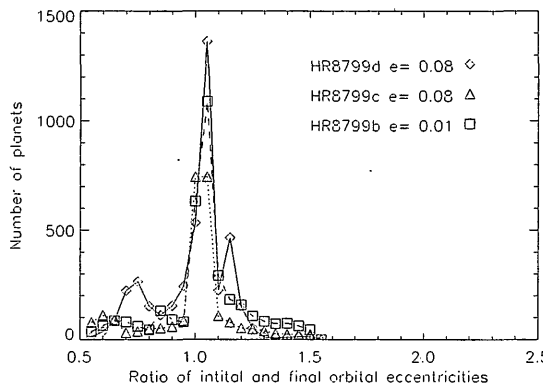
HR8799d e= 0.08 ◇
HR8799c e= 0.08 △
HR8799b e= 0.01 □
Number of planets
Ratio of intital and final orbital eccentricities

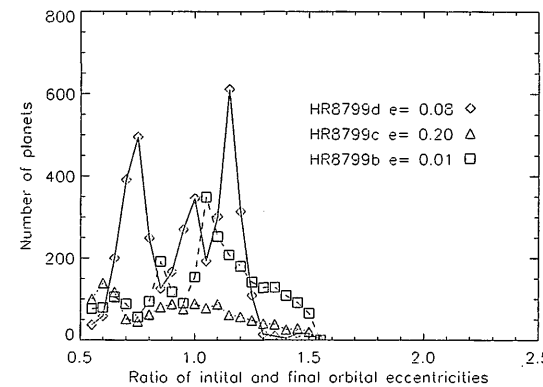
HR8799d e= 0.08 ◇
HR8799c e= 0.20 △
HR8799b e= 0.01 □
Number of planets
Ratio of intital and final orbital eccentricities

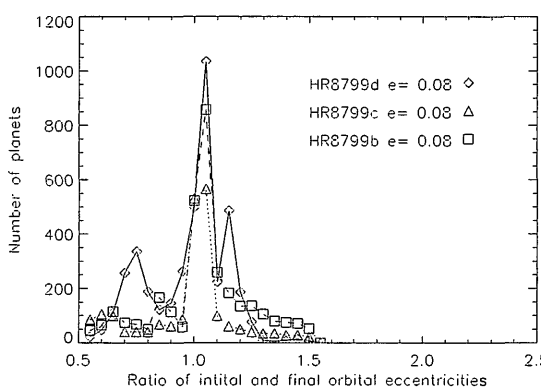
HR8799d e= 0.08 ◇
HR8799c e= 0.08 △
HR8799b e= 0.08 □
Number of planets
Ratio of intital and final orbital eccentricities

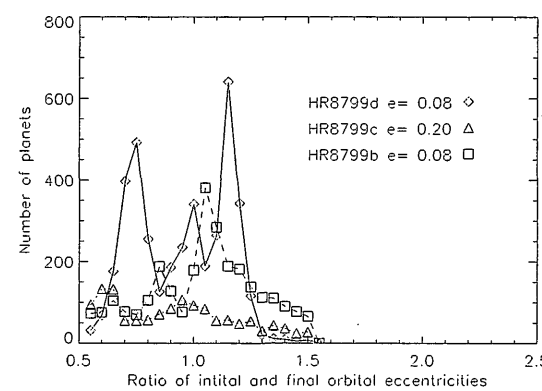
HR8799d e= 0.08 ◇
HR8799c e= 0.20 △
HR8799b e= 0.08 □
Number of planets
Ratio of intital and final orbital eccentricities

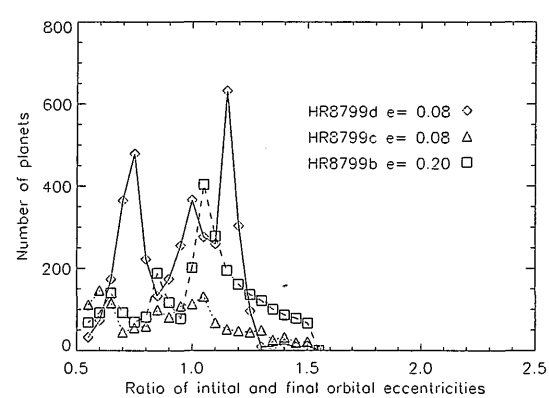
HR8799d e= 0.08 ◇
HR8799c e= 0.08 △
HR8799b e= 0.20 □
Number of planets
Ratio of intital and final orbital eccentricities

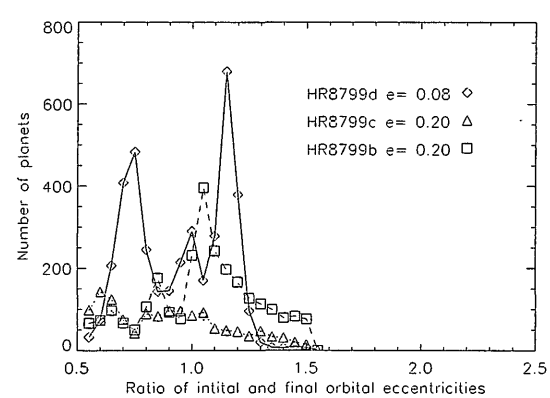
HR8799d e= 0.08 ◇
HR8799c e= 0.20 △
HR8799b e= 0.20 □
Number of planets
Ratio of intital and final orbital eccentricities

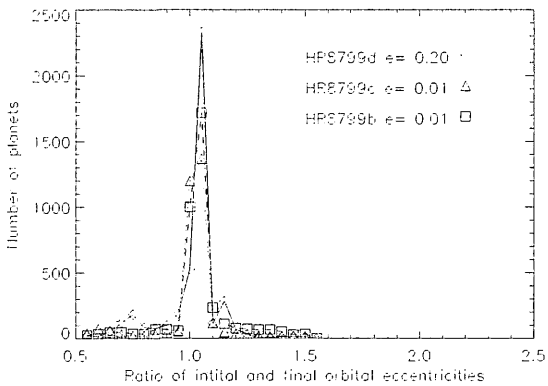
HR8799d e= 0.20
HR8799c e= 0.01
HR8799b e= 0.01
Number of planets
Ratio of intital and final orbital eccentricities

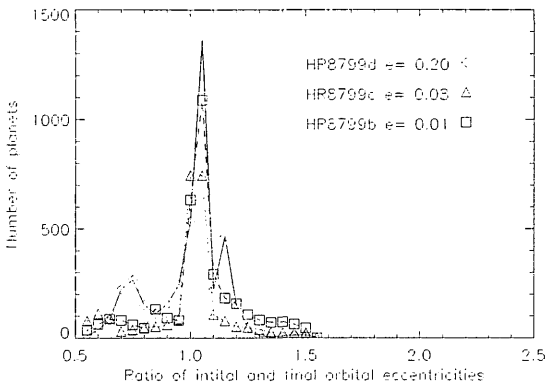
HR8799d e= 0.20
HR8799c e= 0.08
HR8799b e= 0.01
Number of planets
Ratio of intital and final orbital eccentricities

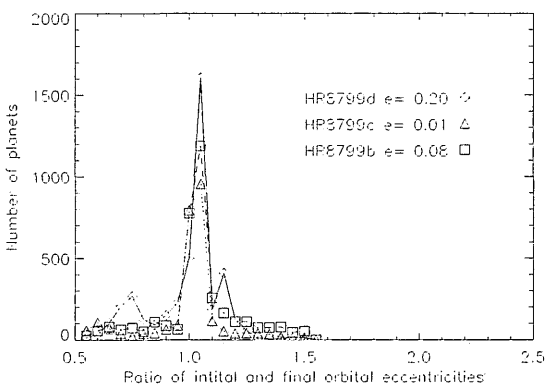
HR8799d e= 0.20
HR8799c e= 0.01
HR8799b e= 0.08
Number of planets
Ratio of intital and final orbital eccentricities

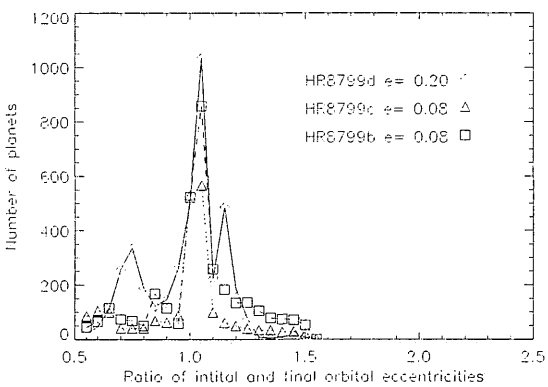
HR8799d e= 0.20
HR8799c e= 0.08
HR8799b e= 0.08
Number of planets
Ratio of intital and final orbital eccentricities

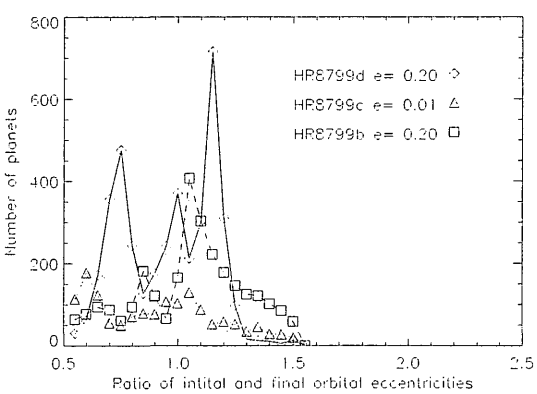
HR8799d e= 0.20
HR8799c e= 0.01
HR8799b e= 0.20
Number of planets
Ratio of intital and final orbital eccentricities

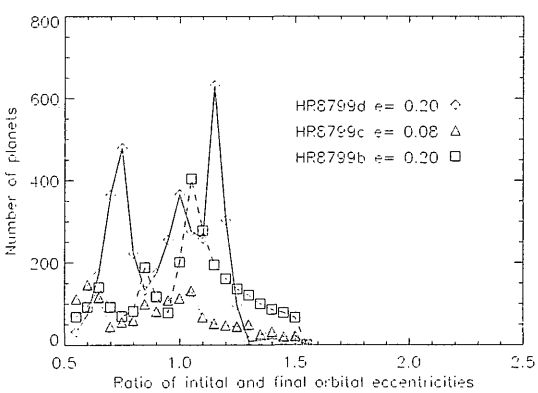
HR8799d e= 0.20
HR8799c e= 0.08
HR8799b e= 0.20
Number of planets
Ratio of intital and final orbital eccentricities

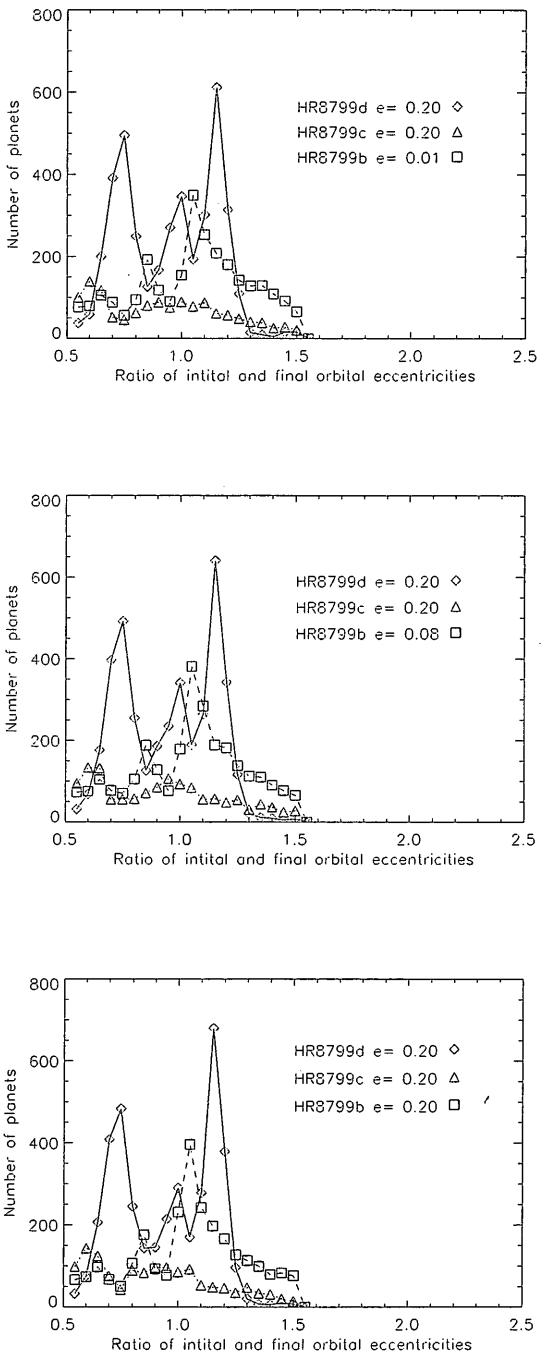


Figure 7.28: Survival plots of the number of systems vs. the ratio of initial to final orbital eccentricity for the the three planets in systems where all three survived until the end of the 1 Myr integration.

## 7.4 Discussion

In our simulations of HR8799, we have assumed that the planets are orientated face-on to us ($i_{sys}$=0°) in a coplanar system (such that the orbital inclination of the planets is always 0°) and that the masses and orbital radii of the planets are those derived from astrometry and photometry by M08. In Fabrycky & Murray-Clay (2010), no stable solutions are found over the 160 Myr lifetime of the three planet system with these same assumptions. By introducing small eccentricities to the orbits of the planets, we have shown that the lifetime of the system can be directly increased by a factor of ten and would be expected to remain stable over periods of several Gyr (based on extrapolation from the system survival rates).

At low eccentricities, the system is typically stable for the full duration of our simulation over the entire dynamical phase space. This is an interesting result, as previous studies (Fabrycky & Murray-Clay, 2010; Marois et al., 2008) found the system to be dynamically unstable on timescales of a few hundred thousand years for planets on initially circular orbits. This might suggest that a small amount of initial eccentricity in the orbits of the planets could prove a stabilising influence. However, this seems unlikely, since objects on zero-eccentricity orbits would have to become excited through higher eccentricities in order to experience the kind of close encounters needed to cause either ejection or collision. It should be noted that those authors used a smaller ejection distance (500 AU vs. our 1000 AU) and a much larger collision radius (1 Hill Radius vs. our physical collision) to determine the removal of their planets. This, however, does not seem sufficient to explain the differences in our results. We note that we survey the possible separations of the three planets in more detail than that work, and so it might be that they happened to examine the most unstable region of possible planetary orbits. Alternatively, it might be that the initial mean anomalies used (which we randomised, while they kept fixed) played a role in determining the stability of the system. It is easy to envision a scenario in which three bodies in an approximate 1:2:4 orbital period set up could be either highly stable (e.g. Io, Europa and Ganymede in our own Solar system) or highly unstable, depending

on the initial mean anomalies used. In the case of the Galilean satellites, the distribution of the three objects about Jupiter is such that a triple conjunction never occurs - no matter how long you wait, you never have a situation where Io, Europa and Ganymede are all aligned on one side of the planet. Were the initial position of Io moved by, say, 180 degrees, this would no longer be true, and such alignments would happen with great frequency. As such, the effect of the initial mean anomaly of the HR 8799 system should be the subject of further future study.

The study by Goździewski & Migaszewski (2009) varied the planetary masses in addition to the orbital elements to find the most stable solutions. We find agreement between our results and their best-fit model III for a three planet system with moderately eccentric orbits. In their model III, both the inner and middle and middle and outer planets are in 1:2 resonance, i.e. the planetary system, as a whole, is in a 1:2:4 resonance (b:c:d). Only 20% of the systems in their model III survive for the full simulation run (160 Myr), however. The figures below (Fig. 7.4 and 7.4) illustrate the dynamical evolution of the system in this configuration as calculated in our simulations. The fluctuations in planetary eccentricity and orbital radius are both periodic and of small amplitude due to the stabilising influence of the 2:1 MMR.

We have not considered the effect of mass on the stability of the system, using only the given values derived from photometry, which are model dependent and therefore uncertain by a factor of ~25%. We note that increasing the planetary masses would likely act to make the system more unstable, due to the increased mutual gravitational forces. However, the presence of an extended cold dust disc implies the system age to be at the lower end of the current estimates (20 – 1100 Myr), based on the timescale for disc dissipation around A stars (Su et al., 2006; Wyatt et al., 2007). This in turn favours lower mass estimates for the planets since younger planets will be hotter and therefore appear brighter. We have also not considered the impact of inclined orbits on our simulations, though it is expected that any deviation from coplanarity in the system, based on our knowledge of the Solar System, would be small.

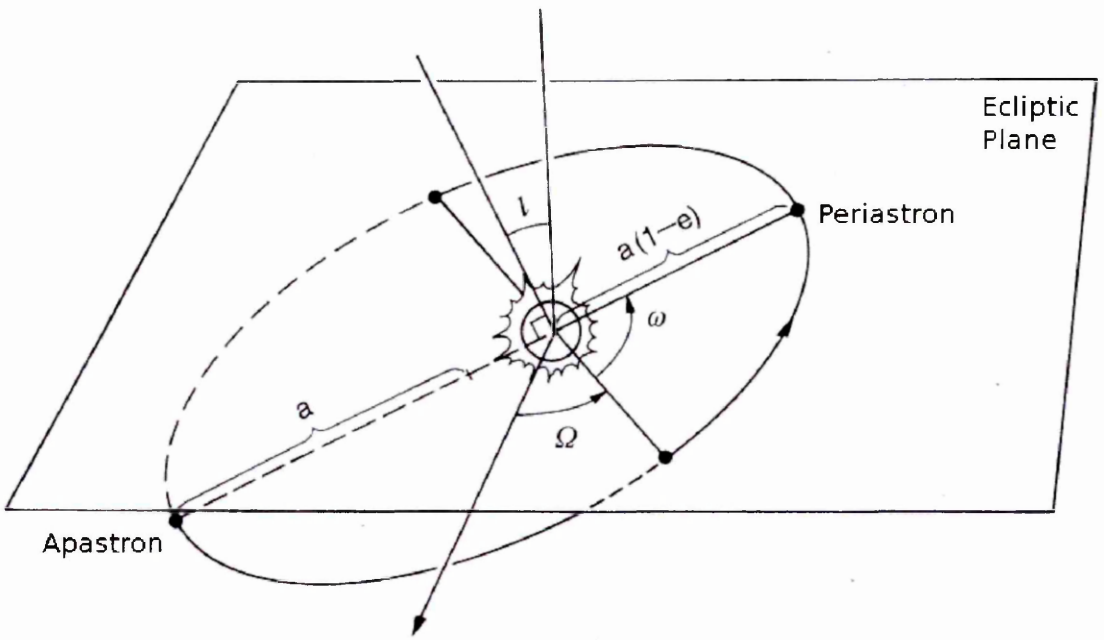


Figure 7.29: Image illustrating the orbital elements for which we have plotted the variations as a function of time in Figs 7.4–7.4. The semi-major axis $a$, and the apastron (Q) and periastron (q) distances, the longitude of the ascending node ($\Omega$) and the argument of periapsis ($\omega$).

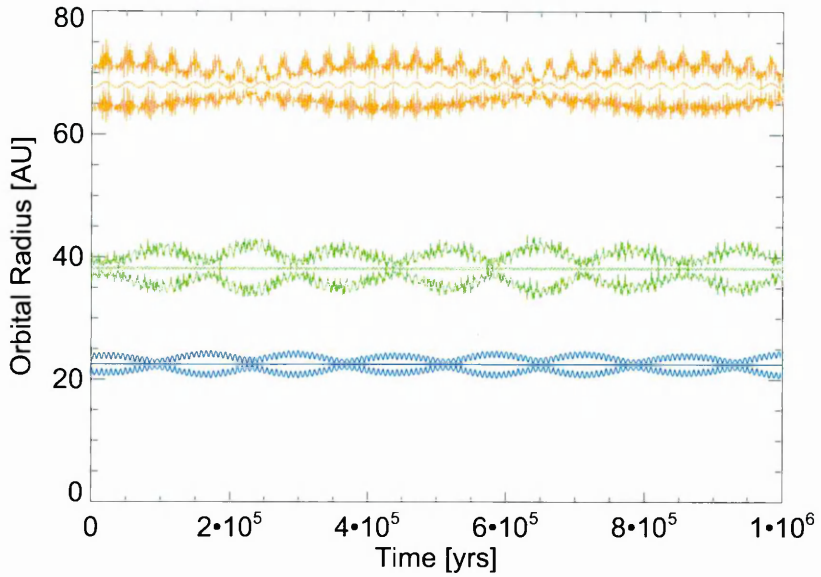


Figure 7.30: Evolution of the radial distances of the three planets over the 1 Myr integration. Initial orbital radii were 24.0, 38.0 and 68.0 AU for planets d,c and b, respectively.

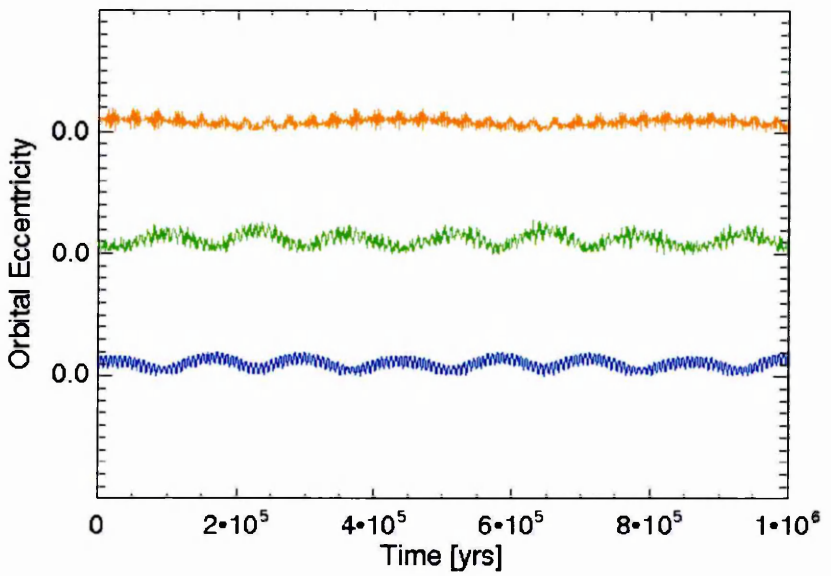


Figure 7.31: Evolution of the eccentricities ($e$) of the three planets over the 1 Myr integration. All three planets had an initial eccentricity of 0.08. The small gradations on the ordinate represent a difference of 0.1.

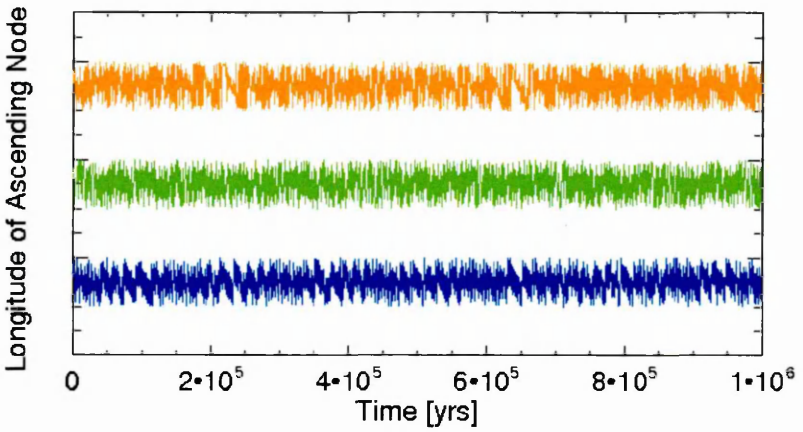


Figure 7.32: Evolution of the longitude of the ascending node ($\Omega$) of the three planets over the 1 Myr integration.

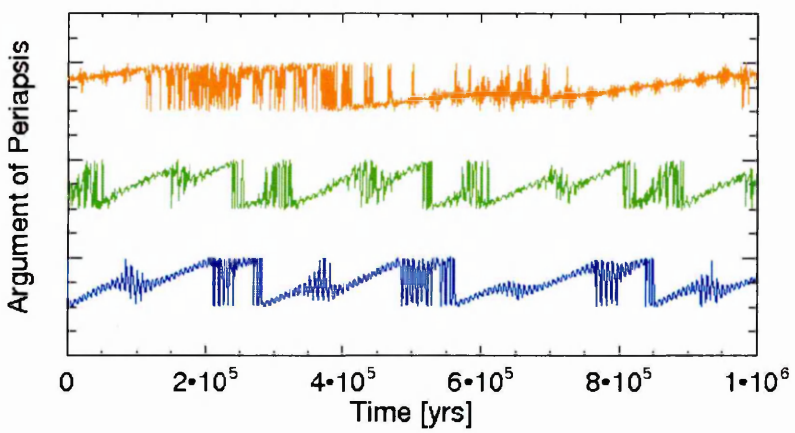


Figure 7.33: Evolution of the argument of periapsis ($\omega$) of the three planets over the 1 Myr integration.

## 7.5 Conclusions

We have performed a detailed dynamical study on the impact of orbital eccentricity in the HR8799 system. Broadly speaking, our analysis is in agreement with similar studies of the system by other authors. For moderate values of eccentricity ($e$ ~0.01 – 0.08), we have shown statistically that the three planet system is dynamically stable over the lifetime of the star, assuming the projected orbital radii are face on to us; that the planetary masses are close to those derived from photometry; and that the planets are coplanar. In contrast to previous results (Fabrycky & Murray-Clay, 2010), we have shown the HR8799 system to be stable for low ($e \sim 0.01$) eccentricities over Myr timescales, and potentially stable for Gyr timescales. We find the dominant limitation on system stability is interaction between the inner two planets (d and c), causing disruption through collision or ejection on timescales of a few $\times 10^4 - 10^5$ yrs for systems with moderate or high ($e \sim 0.08 - 0.20$) initial eccentricities. This result is in agreement with the previous findings of Goździewski & Migaszewski (2009).

As one of only a handful of systems identified with both exoplanet(s) and a debris disc, the rarity of HR8799 makes it an obvious target for further study. Of particular interest is the interaction between the disc and outer exoplanet, and the influence this has on the planet formation process, as it may be analogous to the proposed LHB phase in the early Solar System. The planetary system around HR8799 will be resolvable at sub-mm wavelengths by next generation radio telescopes such as ALMA, making it a tempting target with which to study dust-planet interaction in unprecedented detail.

# 8

# Summary

The primary objective of this thesis was to perform a quantitative study of the frequency of dust around main sequence stars using data from the AKARI FIS all sky survey. In this thesis, the development and structure of a pipeline purpose built to analyse the survey results, is described. Tracing the temporal evolution of circumstellar dust discs, the thesis began with a search for YSOs in the Lynds 1551 Dark Nebula, part of the Taurus star forming region, at mid infrared wavelengths using *Spitzer*/IRAC archival data. The core results of the thesis, an analysis of the AKARI FIS all sky survey, were then presented, describing the reduction and calibration of the data before presenting the results of two searches of the FIS data. The thesis continued with a detailed study of the 49 Ceti debris disc before finishing with preliminary results of work still in progress – a survey for cold debris discs in an *Herschel* ATLAS field, and a dynamical study of HR8799, a debris disc star recently discovered to host three planets. A brief summary of the aims and main results of each of these components is presented here.

## Overview

In the introduction two key questions that could be addressed by this thesis were identified, namely improving the value of the frequency of debris discs (through the use of the AKARI far infra-red all sky survey at 90 $\mu$m) and how the addition of this data to previously detected debris disc SEDs could be used to better constrain the physical properties of those systems. Neither of

these questions could be directly answered by the thesis. In the first case, the small number of debris discs detected by AKARI (fewer than predicted from *IRAS* measurements and possibly an effect of typical dust temperatures), the strong preference toward early spectral type stars biasing the sample (similar to *IRAS*) and the lack of a photospheric flux measurement in the cases of stars with non-detections (cf *Spitzer*, a pointed observatory) meant that the survey was too shallow to provide any additional benefit to the work done by *Spitzer* around the same time. In the second case, the limiting sensitivity of the AKARI 90 $\mu$m band and large calibration uncertainties ($\sim$ 20–30%) led to all of the detected debris disc in the survey being already known and having superior measurement of their SEDs at comparable wavelengths (either MIPS 70 or *IRAS* 100 fluxes) upon which the additional AKARI data made no meaningful constraint.

In the case of the first question of my thesis, it is now being answered by the *Herschel* Open Time Key Program DUNES within which I am responsible for data reduction and analysis of the sample. Early results suggest that the incidence of dust around solar type stars is much greater (25–33%) than deduced from *Spitzer* MIPS results (see Future Work section in Conclusions).

## YSO population of L1551

The L1551 dark nebula is one of the nearest and best studied sites of low mass star forming regions. We took mid infrared 3.6 – 8.0 $\mu$m images from the *Spitzer* archive. This data was combined with previous infrared (*ISO*) and X-ray (*Chandra*) surveys of the region. Sources were associated between the different surveys across X-ray – infrared wavelengths. Identification of the YSOs in the region was made through source X-ray activity, spectral index, colour-magnitude and colour-colour diagrams.

We identified 18 YSO candidate sources in the region, of which 8 had been previously identified. The brightest sources in the field were saturated, due to the use of only long exposure data. This was necessitated by the objective of the survey, namely finding new and faint YSO

candidates to better characterise the total population of YSOs, whilst minimising the contamination due to background noise and transient events. The majority of the YSOs identified in this work were Class II objects, supporting the conclusions of previous studies that the region is very young (1 – 3 Myr). We did not see a significant difference between the small region presented here and the YSO population of the Taurus cloud, either in the frequency of YSO types, the source luminosity function or their spatial distribution. Although the dynamics of the L1551 region are dominated by massive jets from L1551NE and L1551 IRS5, these have not had an impact on the population of YSOs in their vicinity, e.g. by triggering star formation. There was no evidence for a previous generation of stars in the field, though the lack of photometry beyond 10 $\mu$m meant that no constraints could be placed on the presence of cool dust around those stars without any measurable excess (Class III sources).

## AKARI FIS All Sky Survey

The AKARI all sky survey studied the infrared sky at greater resolution, sensitivity and across a broader wavelength range than the previous *IRAS* survey. A list of target stars for a debris disc search was drawn up. The all sky survey data was directly queried, using the SUSSExtractor pipleline to reduce TSD into images and then perform aperture photometry on the fields. Candidate disc sources were identified by cross correlation with optical and near infrared catalogues. Stellar spectral type and photospheric emission was estimated using the source near infrared colours (from 2MASS). The far infrared excess was fitted using a modified black body model and from this the temperature, fractional luminosity and mass of the disc were derived. Those sources that had fractional luminosities ($\tau > 10^{-3}$) and masses ($M_{dust} > 3\ M_{\oplus}$) incompatible with debris discs were rejected.

We have identified 47 stars in the AKARI FIS all sky survey with far infrared excess attributable to circumstellar dust. Half (24) of these discs are previously identified *IRAS* discs. The previously identified sources are all well studied, bright debris discs; the AKARI photometry presented in this thesis provides no new scientific benefit, as they are all well studied by

multiple observatories to greater sensitivity and across a broader wavelength range (providing superior constraints on the nature of the dust) than the AKARI all sky survey. The new discs presented in this thesis are only observed in the (best calibrated) WIDE-S band. The lack of multiple wavelength confirmation of these new sources precludes constraint of the disc temperature and necessitates the modelling assumption that the disc emission peaks at 90 $\mu$m. Several known debris discs were identified in the directly analysed sample of stars, but had significance levels $< 5\sigma$, preventing their inclusion into the point source catalogue. With further improvements to the data reduction it is hoped that these sources will be positively identified in future versions of the catalogue, with the implication that there are many more debris disc candidates in the data, but currently at too low significance to be identified.

## Infrared Excess From DUNES Targets

The AKARI mid infrared all sky survey was a vast improvement in both resolution and sensitivity over the previous *IRAS* survey. Using the publically released IRC PSC we searched for excess emission attributable to hot dust from stars that will be observed by *Herschel* as part of the DUNES open time key program. Over 100 of the 133 target stars had matches in the IRC catalogue. The presence of infrared excess around the targets was determined by the use of a colour-colour plot. Stars with only 18 $\mu$m fluxes were assumed to have photospheric emission at 9 $'mu$m, values of which were taken from photosphere fits by B. Montesinos. Those targets with infrared excess at 9 and/or 18 $\mu$m were fitted with single temperature black body models from which fractional excesses and disc masses were derived.

We identified eight stars from the DUNES target list with warm dust excesses. Of these, one (HIP40693) had previously identified warm excess. Another (HIP28103) of the excess sample have been identified with cold dust excesses from *Spitzer* observations. None of the stars with a rising IRS spectrum or strong 70 $\mu$m excess were identified as possessing a warm dust excess from this work. The incidence of warm excess was greater for earlier spectral types. There was no correlation between warm excess and the presence of exoplanets or previously

identified cold dust excess.

## Resolved Observations of 49 Ceti

A young debris disc star, 49 Ceti is at the end of, or shortly after, its transitional disc phase. Using photometry in all four FIS wavebands, and the images from the two shorter wavelengths, we have modelled the 49 Ceti debris disc looking for signs of a large extended disc, similar to those around Vega and $\beta$ Pictoris. The TSD files were reduced using the FIS slow scan tools and photometry was carried out using IRAF. Modelling and fitting the observed image to both a thermal model and synthetic image was performed using Monte Carlo analysis of the disc parameters.

We have detected extended emission at 65 $\mu$m that we attribute to a resolved disc around 49 Ceti, with an inclination and position angle consistent with previous resolved observations of the disc. The best fit model of the disc, with parameters fitted to both the SED and resolved image, requires a disc over 1000 AU in radius with a dust mass of 0.4 $M_{\oplus}$, comparable to that of $\beta$ Pictoris. The gas-to-dust ratio of 32 (from a sub-mm gas CO gas mass) provides supporting evidence that the star is young.

Although this result is promising, there are still some questions over the PSF analysis of the 90 $\mu$m image, which is required to better constrain the dust properties through resolved imaging at multiple wavelengths.

## H-ATLAS Debris Disc Survey

The *Herschel* ATLAS project covers six major science themes, one of which is galactic objects (e.g. stars). The ATLAS will observe regions near both galactic poles and an area coinciding with the GAMA [Galaxy And Mass Assembly][](Driver et al., 2009) survey, to maximise the amount of ancillary data available. The fields of this survey therefore include a large number of stars in the galactic foreground. Using the SPIRE source catalogue provided by the H-ATLAS data reduction team, we have identified stars from the Tycho-2 and 2MASS catalogues and

matched them with *Herschel* sub-mm sources.

We have identified 19 stars in the H-ATLAS field with close positional associations to sub-mm sources in the SPIRE catalogue. These discs appear to be cold ($T < 30\ K$) and massive (for most, $M_{dust} > 0.1\ M_{\oplus}$). This result is unexpected, since none of the currently known debris discs have comparable masses or a significant cold dust component without emission at shorter (far infrared) wavelengths. Currently, the quality of the PACS photometry is poorer than expected and therefore does little to constrain the shape of the disc SED. The far infrared PACS photometry will be useful to help discern if these associations are real or alignment with background sub-mm source, which is the focus of the ongoing work on these objects. If this first region is typical of the remaining H-ATLAS fields, we can expect to find almost as many debris discs as the DEBRIS key program, providing a complimentary addition at larger distances to the nearby populations sampled by other *Herschel* debris disc programs.

## Dynamical Stability of HR8799

Near infrared imaging of HR8799 identified three planet-mass companions to this (*IRAS* discovered) debris disc star in 2008. This is one of only a handful of systems where exoplanets and a dust disc are known to coexist. The outer planet of the system and cool dust disc (exo-Kuiper belt) are at similar orbital radii, implying that the planet may be perturbing and gravitationally sculpting the belt (similar to Fomalhaut's planet). The dynamical stability of the three planet system has been studied several times after initial simulations implied that the configuration was very unstable for the observed planet masses and orbital radii. We have performed dynamical simulations of the HR8799 system using the *MERCURY* numerical integration code. Simulations of the system were started with each of the three planets in different combinations of eccentricity and orbital radius, each running for a period of 1 Myr with 10 repetitions to obtain statistics on the survival time of the initial configuration.

We find that the HR8799 system has stable architectures for at least 1 Myr with small eccentricity values and positional offsets within the observational uncertainties. This result

contradicts the initial findings of Marois et al., who claimed very few solutions with periods of more than $10^5$ yrs existed. Varying the individual eccentricities of the three planets, we find that the dominant destabilising influence is the interaction between the inner and middle planets, either through collision or scattering. The most stable planetary configuration, regardless of planetary eccentricity, lies with the planets in a 1:2:4 resonance. The results of this study are broadly in agreement with the findings of previous studies of the system.

# 9

# Conclusions

In Chapter 3, a search for YSOs in the Lynds 1551 Dark Nebula observed 18 new YSO candidate sources. The PMS objects, believed to be associated with the nebula, were found to be more closely associated (by median nearest neighbour separation) than main-sequence stars in the same field of view, such that the PMS objects are clustered compared to the main sequence stars. Given that the ages of these PMS objects is small, the star formation in L1551 is clustered rather than isolated.

In Chapter 4, analysis of the AKARI FIS all sky survey turned up fewer debris discs than expected. This result ruled out the existence of previously unknown cold dust populations around nearby *IRAS* debris discs, as extrapolation from 60 $\mu$m fluxes ruled out the possible detection of these discs by AKARI. This in turn implies that most cold debris discs have a single belt of parent planetesimals. In addition to the confirmation of several *IRAS* debris discs, there were a handful of new candidate debris discs observed. These new discs have masses consistent with known debris disc archetypes, but higher fractional luminosities, implying that the discs are dustier and likely younger than the previously known discs in the total sample. Overall, the dust mass of the discs in the sample is seen to decline toward later spectral type (though the sample is strongly biased towards early type stars).

In Chapter 5, we identified eight warm debris disc candidates amongst the sample of stars to be observed for the DUNES *Herschel* open time key program. As rare objects, the identification

of new warm excess sources is of paramount importance in understanding the origins and evolution of these objects. In the sample of eight discs we detect, one is a well known warm debris disc (HIP 40693/HD 69830) with no cold dust excess, and only one other (HIP 28103) has a tentative excess at 70 $\mu$m. The number of warm discs detected is greater than predicted from *Spitzer* studies of similar (FGK) stars, implying that warm dust belts (analogous to the asteroid belt) are more common than is observable with current instrumentation. We see the frequency of excess systems strongly decrease towards later spectral type illustrating that, as expected, the detectability of warm dust is a strong function of the dust temperature at mid infrared wavelengths (where the stellar photosphere is still a major contribution to the total source flux).

In Chapter 6, a study of pointed AKARI observations at 65 $\mu$m of 49 Ceti revealed extended emission from the star along the same axis as the mid infrared and CO disc. The properties of the disc extent and mass required to produce the (marginally) resolved emission imply that the disc around 49 Ceti rivals that of $\beta$ Pictoris in both extent and mass. This result is consistent with the young age of 49 Ceti, derived previously from optical and near infrared photometric measurements.

In Chapter 7, a survey for the serendipitous discovery of debris discs in the H-ATLAS SDP field identified six likely debris disc candidates. These discs were modelled as having properties inconsistent with previously known discs around stars in the solar neighbourhood, being much colder ($T < 30\ K$) and more massive ($M > 1\ M_{\oplus}$) than typical examples. None of the discs identified from SPIRE observations were detected in complimentary observations taken at mid and far infrared wavelengths by the AKARI all sky survey, implying that the dust in these discs is constrained to the outer regions of the system, likely by an exoplanet interior to the disc, and that the size of these discs are much larger (> 100 AU) than typical debris disc systems. In a field of 549 stars, only six of these objects were detected, giving a frequency of ~ 1%, which is much lower than the total incidence of 13% for typical debris discs. The sensitivity limits of both the far infrared and sub-mm data are biased towards more massive

discs (e.g. $\beta$ Pictoris or HR8799 analogues). The absence of any discs (in the far infrared data) and few detections (in the sub-mm data) imply that such massive discs are rare (to a mass limit 0.3 $M_{\oplus}$ at 120 pc). From this it may be inferred that most exo-solar Edgeworth-Kuiper belt analogues are more similar to the Solar System than the examples in the vicinity of the Earth. However, one mid infrared source was observed in the IRC all sky survey to have an 18 $\mu$m excess, out of 88 sources in the field, consistent with an expected detection rate of 2±2% for warm debris discs. This IRC source did not have a detectable far infrared excess, suggesting that it may be an example of a warm-excess disc, similar to HD69830.

In Chapter 8, a comprehensive suite of dynamical simulations studying the three planets around HR8799 revealed that the system architecture was demonstrably stable over the lifetime of the star, even under the constraints of assuming the system was face on and the planetary masses were close to the photometric values. This result totally contradicts initial studies of the system, which suggested the system (as observed) was unstable on periods of > 1 Myr. The most stable planetary configuration found in this work, with the three planets in a 1:2:4 mutual MMR, provides confirmation of the results of other studies identifying this system as unique amongst currently known exoplanet systems having two pairs of planets in mutual orbital resonances.

## Future Work

As previously discussed in both Chapters 4 and 5, the sensitivity of the AKARI All Sky Survey was too poor to provide an improvement to previously derived constraints on the presence of cold dust around other stars. I will continue working on this major theme of my thesis in my research for the *Herschel* DUNES collaboration with Carlos Eiroa in Madrid. The DUNES program will sample over 100 nearby stars and the survey detection capability is limited primarily by the uncertainty in the stellar atmosphere models.

Also leading on from the work presented in Chapter 5, I will be looking at dusty discs in the galactic plane using the better resolution of AKARI over previous surveys, combined with

*Spitzer* GLIMPSE and MIPSGAL results to make robust identifications of debris discs within ±20° of the galactic plane, which has not previously been possible in the far infrared due to source confusion in this bright, complex region of the sky.

Discussed in Chapter 7, the initial results from the *Herschel* ATLAS survey have yielded three strong debris disc candidates. As an extension to these 'proof of concept' results from the SPIRE SDP data, I am working with Mark Thompson and others in the H-ATLAS galactic working group to provide accurate stellar classification of the stars and grey body models of the disc emission, which is vital to obtain an accurate determination of the disc mass. The discs we observe around these stars appear to be colder and more massive than those detected in previous far infrared/sub-mm surveys, so these may be the first objects in a new class of debris discs.

# References


Ardila, D. R., Golimowski, D. A., Krist, J. E., et al. 2004, Astrophys. J., Lett., 617, L147 9

Artymowicz, P. 1997, Annual Review of Earth and Planetary Sciences, 25, 175 13

Augereau, J., Absil, O., Bouvier, J., et al. 2008, in SF2A-2008, ed. C. Charbonnel, F. Combes, & R. Samadi, 443–+ 92, 123

Augereau, J. & Beust, H. 2006, Astron. Astrophys., 455, 987 34

Augereau, J. C., Nelson, R. P., Lagrange, A. M., Papaloizou, J. C. B., & Mouillet, D. 2001, Astron. Astrophys., 370, 447 12, 21

Aumann, H. H., Beichman, C. A., Gillett, F. C., et al. 1984, Astrophys. J., Lett., 278, L23 1

Aumann, H. H. & Good, J. C. 1990, Astrophys. J., 350, 408 15

Backman, D., Marengo, M., Stapelfeldt, K., et al. 2009, Astrophys. J., 690, 1522 8, 9

Backman, D. E., Dasgupta, A., & Stencel, R. E. 1995, apjl, 450, L35+ 15

Backman, D. E. & Paresce, F. 1993, in Protostars and Planets III, ed. E. H. Levy & J. I. Lunine, 1253–1304 1, 13, 31, 32

Backman, D. E., Witteborn, F. C., & Gillett, F. C. 1992, Astrophys. J., 385, 670 32

Beckwith, S. V. W. & Sargent, A. I. 1991, Astrophys. J., 381, 250 34

Beichman, C. A., Bryden, G., Stapelfeldt, K. R., et al. 2006a, Astrophys. J., 652, 1674 1, 18, 94, 107

Beichman, C. A., Tanner, A., Bryden, G., et al. 2006b, Astrophys. J., 639, 1166 7, 69, 89

Bessell, M. S. & Brett, J. M. 1988, Publ. Astron. Soc. Pac., 100, 1134 27, 39, 68, 112

Bohren, C. F. & Huffman, D. R. 1983, Absorption and scattering of light by small particles, ed. Bohren, C. F. & Huffman, D. R. 33

Bouwman, J., Henning, T., Hillenbrand, L. A., et al. 2008, Astrophys. J., 683, 479 36

Bouwman, J., Meeus, G., de Koter, A., et al. 2001, Astron. Astrophys., 375, 950 5

Bregman, J. D., Witteborn, F. C., Allamandola, L. J., et al. 1987, Astron. Astrophys., 187, 616 7

Briceño, C., Hartmann, L., Stauffer, J., & Martín, E. 1998, Astron. J., 115, 2074 36

Bryden, G., Beichman, C. A., Trilling, D. E., et al. 2006, Astrophys. J., 636, 1098 8, 69, 92

Burns, J. A., Lamy, P. L., & Soter, S. 1979, Icarus, 40, 1 14

Burrows, C. J., Krist, J. E., Stapelfeldt, K. R., & WFPC2 Investigation Definition Team. 1995, in Bulletin of the American Astronomical Society, Vol. 27, Bulletin of the American Astronomical Society, 1329–+ 12

Burrows, C. J., Stapelfeldt, K. R., Watson, A. M., et al. 1996, Astrophys. J., 473, 437 37

Butner, H. M., Wooden, D. H., Harker, D. E., & Woodward, C. E. 2003, in Astronomical Society of the Pacific Conference Series, Vol. 294, Scientific Frontiers in Research on Extrasolar Planets, ed. D. Deming & S. Seager, 235–238 7

Cameron, A. G. W. & Truran, J. W. 1977, Icarus, 30, 447 20

Campo Bagatin, A., Farinella, P., & Petit, J. 1994, Planet. Space Sci., 42, 1099 32

Cannon, A. J. & Pickering, E. C. 1993, VizieR Online Data Catalog, 3135, 0 63

Castelli, F. & Kurucz, R. L. 2004, ArXiv Astrophysics e-prints 68, 112

Chambers, J. E. 1999, Mon. Not. R. Astron. Soc., 304, 793 128

Chambers, J. E. 2001, Icarus, 152, 205 128

Chen, C. H., Sargent, B. A., Bohac, C., et al. 2006, apjs, 166, 351 7

Chen, C. H., Sheehan, P., Watson, D. M., Manoj, P., & Najita, J. R. 2009, Astrophys. J., 701, 1367 126

Condon, J. J., Cotton, W. D., Greisen, E. W., et al. 1998, Astron. J., 115, 1693 65, 114

Davenport, J. R. A., West, A. A., Matthiesen, C. K., Schmieding, M., & Kobelski, A. 2006, pasp, 118, 1679 117

Dent, W. R. F., Walker, H. J., Holland, W. S., & Greaves, J. S. 2000, Mon. Not. R. Astron. Soc., 314, 702 26

Dermott, S. F., Kehoe, T. J. J., Durda, D. D., Grogan, K., & Nesvorný, D. 2002, in ESA Special Publication, Vol. 500, Asteroids, Comets, and Meteors: ACM 2002, ed. B. Warmbein, 319–322 20

Devine, D., Reipurth, B., & Bally, J. 1999, Astron. J., 118, 972 36

Di Francesco, J., Johnstone, D., Kirk, H., MacKenzie, T., & Ledwosinska, E. 2008, Astrophys. J., Suppl. Ser., 175, 277 36

Dohnanyi, J. W. 1969, J. Geophys. Res., 74, 2531 32

Dominik, C. & Decin, G. 2003, Astrophys. J., 598, 626 13

Draine, B. T. & Lee, H. M. 1984, Astrophys. J., 285, 89 34, 35

Draine, B. T. & Li, A. 2001, Astrophys. J., 551, 807 35

Driver, S. P., Norberg, P., Baldry, I. K., et al. 2009, Astronomy & Geophysics, 50, 050000 161

Dwek, E. 2005, in American Institute of Physics Conference Series, Vol. 761, The Spectral Energy Distributions of Gas-Rich Galaxies: Confronting Models with Data, ed. C. C. Popescu & R. J. Tuffs, 103–122 5

Eales, S., Dunne, L., Clements, D., et al. 2009, ArXiv e-prints 110

Eisenhardt, P. R., Wright, E. L., Benford, D., et al. 2009, in Bulletin of the American Astronomical Society, Vol. 41, Bulletin of the American Astronomical Society, 363–+ 109

Emerson, J. P., Harris, S., Jennings, R. E., et al. 1984, Astrophys. J., Lett., 278, L49 37

Esposito, L. W. 2002, Reports on Progress in Physics, 65, 1741 123

Fabrycky, D. C. & Murray-Clay, R. A. 2010, Astrophys. J., 710, 1408 126, 127, 130, 151, 156

Favata, F., Giardino, G., Micela, G., Sciortino, S., & Damiani, F. 2003, Astron. Astrophys., 403, 187 36, 37

Fazio, G. G., Hora, J. L., Allen, L. E., et al. 2004, Astrophys. J., Suppl. Ser., 154, 10 38, 95

Fitzpatrick, E. L. & Massa, D. 2009, Astrophys. J., 699, 1209 112

Flaherty, K. M., Pipher, J. L., Megeath, S. T., et al. 2007, Astrophys. J., 663, 1069 39

Fogg, M. J. & Nelson, R. P. 2005, Astron. Astrophys., 441, 791 128

Ford, E. B., Lystad, V., & Rasio, F. A. 2005, Nature, 434, 873 128

Fridlund, C. & Liseau, R. 1994, Astron. Astrophys., 292, 631 36

Fridlund, C. & Liseau, R. 1998, Astrophys. J., Lett., 499, L75+ 36, 37

Fridlund, C., Liseau, R., & Perryman, M. 1993, Astron. Astrophys., 273, 601 36

Fridlund, C., Sandqvist, A., Nordh, H., & Olofsson, G. 1989, Astron. Astrophys., 213, 310 37

Fridlund, C. V. M., Liseau, R., Djupvik, A. A., et al. 2005, Astron. Astrophys., 436, 983 36

Fridlund, C. V. M., Nordh, H. L., van Duinen, R. J., Aalders, J. W. G., & Sargent, A. I. 1980, Astron. Astrophys., 91, L1+ 37

Fridlund, C. V. M. & White, G. J. 1989, Astron. Astrophys., 223, L13 36, 37

Fujiwara, H., Ishihara, D., Yamashita, T., et al. 2009, in American Institute of Physics Conference Series, Vol. 1158, American Institute of Physics Conference Series, ed. T. Usuda, M. Tamura, & M. Ishii, 89–92 98, 107, 108

Fukagawa, M., Itoh, Y., Tamura, M., et al. 2009, Astrophys. J., Lett., 696, L1 126

Gålfalk, M., Olofsson, G., Kaas, A. A., et al. 2004, Astron. Astrophys., 420, 945 37

Gálvez, Ó., Maté, B., Herrero, V. J., & Escribano, R. 2009, Astrophys. J., 703, 2101 34

Ghez, A. M., Neugebauer, G., & Matthews, K. 1993, Publ. Astron. Soc. Pac., 105, 951 37

Glass, I. S. 1999, Handbook of Infrared Astronomy, ed. Glass, I. S. 27

Glauser, A. M., Güdel, M., Watson, D. M., et al. 2009, Astron. Astrophys., 508, 247 7

Gomes, R., Levison, H. F., Tsiganis, K., & Morbidelli, A. 2005, Nature, 435, 466 19, 127

Goździewski, K. & Migaszewski, C. 2009, Mon. Not. R. Astron. Soc., 397, L16 126, 127, 152, 156

Greaves, J. S., Fischer, D. A., & Wyatt, M. C. 2006, Mon. Not. R. Astron. Soc., 366, 283 19

Greaves, J. S., Holland, W. S., Moriarty-Schieven, G., et al. 1998, Astrophys. J., Lett., 506, L133 9

Greaves, J. S., Holland, W. S., Wyatt, M. C., et al. 2005, Astrophys. J., Lett., 619, L187 12

Greaves, J. S., Richards, A. M. S., Rice, W. K. M., & Muxlow, T. W. B. 2008, Mon. Not. R. Astron. Soc., 391, L74 36

Greaves, J. S. & Wyatt, M. C. 2010, Mon. Not. R. Astron. Soc., 404, 1944 14

Greaves, J. S., Wyatt, M. C., Holland, W. S., & Dent, W. R. F. 2004, Mon. Not. R. Astron. Soc., 351, L54 ix, 17, 20

Greenberg, J. M. 1978, in NATO ASIC Proc. 38: Infrared Astronomy, ed. G. Setti & G. G. Fazio, 51–95 31

Greenberg, J. M. & Li, A. 1997, Advances in Space Research, 19, 981 33

Griffin, M., Abergel, A., Ade, P., et al. 2007, Advances in Space Research, 40, 612 92, 110

Grn, E. and Gustafson, B.A.S. and Dermott, S.F. and Fechtig, H., ed. 2001, Properties of Interplanetary Dust: Information from Collected Samples (Springer-Verlag), 253–294 xi, 34

Gutermuth, R. A., Megeath, S. T., Myers, P. C., et al. 2010, apjs, 189, 352 42

Haisch, Jr., K. E., Lada, E. A., & Lada, C. J. 2001, Astron. J., 121, 2065 15

Harvey, P., Merín, B., Huard, T. L., et al. 2007, Astrophys. J., 663, 1149 44

Heng, K. & Tremaine, S. 2010, mnras, 401, 867 124

Henning, T., Il'In, V. B., Krivova, N. A., Michel, B., & Voshchinnikov, N. V. 1999, aaps, 136, 405 34

Henning, T. & Mutschke, H. 1997, Astron. Astrophys., 327, 743 34

Hernández, J., Hartmann, L., Megeath, T., et al. 2007, Astrophys. J., 662, 1067 ix, 15, 16, 17

Høg, E., Fabricius, C., Makarov, V. V., et al. 2000, Astron. Astrophys., 355, L27 63, 111

Holland, W. S., Greaves, J. S., Dent, W. R. F., et al. 2003, Astrophys. J., 582, 1141 9

Holland, W. S., Greaves, J. S., Zuckerman, B., et al. 1998, Nature, 392, 788 9

Horner, J., Evans, N. W., & Bailey, M. E. 2004, Mon. Not. R. Astron. Soc., 354, 798 128

Iatì, M. A., Cecchi-Pestellini, C., Williams, D. A., et al. 2001, Mon. Not. R. Astron. Soc., 322, 749 33

Ishihara, D., Onaka, T., Kataza, H., et al. 2009, in American Institute of Physics Conference Series, Vol. 1158, American Institute of Physics Conference Series, ed. T. Usuda, M. Tamura, & M. Ishii, 127–128 97

Ishihara, D., Onaka, T., Kataza, H., et al. 2010, Astron. Astrophys., 514, A1+ 94

Jayawardhana, R., Holland, W. S., Kalas, P., et al. 2002, Astrophys. J., Lett., 570, L93 65

Jones, A. P. 2005, in ESA Special Publication, Vol. 577, ESA Special Publication, ed. A. Wilson, 239–244 4

Jones, B. W. 2008, International Journal of Astrobiology, 7, 279 125

Jura, M., Chen, C. H., Furlan, E., et al. 2004, Astrophys. J., Suppl. Ser., 154, 453 7

Jurić, M., Ivezić, Ž., Brooks, A., et al. 2008, Astrophys. J., 673, 864 41

Kalas, P., Duchene, G., Fitzgerald, M. P., & Graham, J. R. 2007a, Astrophys. J., Lett., 671, L161 9

Kalas, P., Fitzgerald, M. P., & Graham, J. R. 2007b, Astrophys. J., Lett., 661, L85 9

Kalas, P., Graham, J. R., Chiang, E., et al. 2008, Science, 322, 1345 11, 19, 126

Kalas, P., Liu, M. C., & Matthews, B. C. 2004, Science, 303, 1990 9

Kaltenegger, L., Karlsson, A., & Neger, T. 2004, Advances in Space Research, 34, 618 27

Kasting, J. F., Whitmire, D. P., & Reynolds, R. T. 1993, Icarus, 101, 108 4

Kataza, H., Alfageme, C., Cassatella, A., et al. 2010, AKARI/IRC All-Sky Survey Point Source Catalogue, 1–34 xvi, 94, 96, 97

Kawada, M., Baba, H., Barthel, P. D., et al. 2007, Publ. Astron. Soc. Jpn., 59, 389 50, 53

Kemper, F., Vriend, W. J., & Tielens, A. G. G. M. 2004, Astrophys. J., 609, 826 5

Kenyon, S. J., Dobrzycka, D., & Hartmann, L. 1994, Astron. J., 108, 1872 36

Kessler-Silacci, J. E., Hillenbrand, L. A., Blake, G. A., & Meyer, M. R. 2005, Astrophys. J., 622, 404 7

Knacke, R. F., Fajardo-Acosta, S. B., Telesco, C. M., et al. 1993, Astrophys. J., 418, 440 7

Koerner, D. W., Ressler, M. E., Werner, M. W., & Backman, D. E. 1998, Astrophys. J., Lett., 503, L83+ 9

Krauss, O., Wurm, G., Mousis, O., et al. 2007, Astron. Astrophys., 462, 977 11

Krivov, A. V., Löhne, T., & Sremčević, M. 2006, Astron. Astrophys., 455, 509 x, 30

Kuchner, M. 2008, in New Light on Young Stars: Spitzer's View of Circumstellar Disks, ed. SSC, 5th Spitzer Conference 20

Lada, C. J. 1987, in IAU Symposium, Vol. 115, Star Forming Regions, ed. M. Peimbert & J. Jugaku, 1–17 41

Lada, C. J. & Wilking, B. A. 1984, Astrophys. J., 287, 610 41

Lafrenière, D., Marois, C., Doyon, R., & Barman, T. 2009, Astrophys. J., Lett., 694, L148 126

Lagrange, A., Gratadour, D., Chauvin, G., et al. 2008, ArXiv e-prints 11

Lestrade, J., Wyatt, M. C., Bertoldi, F., Menten, K. M., & Labaigt, G. 2009, aap, 506, 1455 18, 89

Li, A. & Greenberg, J. M. 1998, Astron. Astrophys., 331, 291 21

Liseau, R., Eiroa, C., Fedele, D., et al. 2010, aap, 518, L132+ 92

Liseau, R., Fridlund, C., & Larsson, B. 2005, Astrophys. J., 619, 959 37

Liseau, R., Risacher, C., Brandeker, A., et al. 2008, Astron. Astrophys., 480, L47 92

Lisse, C. M., Beichman, C. A., Bryden, G., & Wyatt, M. C. 2007, Astrophys. J., 658, 584 7, 35

Lorente, R., Onaka, T., Ita, Y., et al. 2008, AKARI IRC Data User Manual, 1–107 xvi, 94, 95

Luhman, K. L., Allen, P. R., Espaillat, C., Hartmann, L., & Calvet, N. 2010, Astrophys. J., Suppl. Ser., 186, 111 xi, 43, 48

Luhman, K. L., Mamajek, E. E., Allen, P. R., & Cruz, K. L. 2009, Astrophys. J., 703, 399 37, 42, 47, 48

Lumme, K. & Rahola, J. 1994, Astrophys. J., 425, 653 33

Lykawka, P. S., Horner, J., Jones, B. W., & Mukai, T. 2009, Mon. Not. R. Astron. Soc., 398, 1715 128

Marois, C., Macintosh, B., Barman, T., et al. 2008, Science, 322, 1348 11, 19, 126, 130, 151

Marsh, K. A., Dowell, C. D., Velusamy, T., Grogan, K., & Beichman, C. A. 2006, Astrophys. J., Lett., 646, L77 12

Mathis, J. S., Rumpl, W., & Nordsieck, K. H. 1977, Astrophys. J., 217, 425 32, 34

Matthews, B. C., Greaves, J. S., Holland, W. S., et al. 2007, Publ. Astron. Soc. Pac., 119, 842 60

Mayor, M. & Queloz, D. 1995, Nature, 378, 355 125

Molster, F. J. 2003, in IAU Symposium, Vol. 209, Planetary Nebulae: Their Evolution and Role in the Universe, ed. S. Kwok, M. Dopita, & R. Sutherland, 291–+ 5

Moór, A., Ábrahám, P., Derekas, A., et al. 2006, Astrophys. J., 644, 525 126

Morbidelli, A. & Levison, H. F. 2006, in European Planetary Science Congress 2006, 108–+ 127

Moriarty-Schieven, G. H., Johnstone, D., Bally, J., & Jenness, T. 2006, Astrophys. J., 645, 357 37

Moriarty-Schieven, G. H., Powers, J. A., Butner, H. M., Wannier, P. G., & Keene, J. 2000, Astrophys. J., Lett., 533, L143 37

Moro-Martín, A., Carpenter, J. M., Meyer, M. R., et al. 2007a, Astrophys. J., 658, 1312 19

Moro-Martín, A., Malhotra, R., Carpenter, J. M., et al. 2007b, Astrophys. J., 668, 1165 19

Murakami, H., Baba, H., Barthel, P., et al. 2007, Publ. Astron. Soc. Jpn., 59, 369 xxiv, 50, 61

Napier, W. M. 2010, ArXiv e-prints 20

Neugebauer, G., Habing, H. J., van Duinen, R., et al. 1984, Astrophys. J., Lett., 278, L1 xxiv, 61

Onaka, T., Matsuhara, H., Wada, T., et al. 2007, Publ. Astron. Soc. Jpn., 59, 401 50, 94

Phillips, J. P., White, G. J., Ade, P. A. R., et al. 1982, Astron. Astrophys., 116, 130 37

Phillips, J. P., White, G. J., Rainey, R., et al. 1988, Astron. Astrophys., 190, 289 37

Poglitsch, A., Waelkens, C., Bauer, O. H., et al. 2006, in Presented at the Society of Photo-Optical Instrumentation Engineers (SPIE) Conference, Vol. 6265, Society of Photo-Optical Instrumentation Engineers (SPIE) Conference Series 92, 110

Pollacco, D. L., Skillen, I., Cameron, A. C., et al. 2006, Publ. Astron. Soc. Pac., 118, 1407 125

Pollack, J. B., Hollenbach, D., Beckwith, S., et al. 1994, Astrophys. J., 421, 615 5

Poulton, C. J., Greaves, J. S., & Cameron, A. C. 2006, Mon. Not. R. Astron. Soc., 372, 53 9

Przygodda, F., van Boekel, R., Àbrahàm, P., et al. 2003, Astron. Astrophys., 412, L43 8

Quillen, A. C., Trilling, D. E., & Blackman, E. G. 2004, ArXiv Astrophysics e-prints 20

Rainey, R., White, G. J., Richardson, K. J., et al. 1987, Astron. Astrophys., 179, 237 37

Raymond, S. N., Barnes, R., & Gorelick, N. 2008, Astrophys. J., 689, 478 128

Reche, R., Beust, H., Augereau, J., & Absil, O. 2008, Astron. Astrophys., 480, 551 11

Reidemeister, M., Krivov, A. V., Schmidt, T. O. B., et al. 2009, Astron. Astrophys., 503, 247 126

Rhee, J. H., Song, I., Zuckerman, B., & McElwain, M. 2007, Astrophys. J., 660, 1556 69

Rice, W. K. M., Armitage, P. J., Wood, K., & Lodato, G. 2006, Mon. Not. R. Astron. Soc., 373, 1619 11

Rieke, G. H., Su, K. Y. L., Stansberry, J. A., et al. 2005, Astrophys. J., 620, 1010 15, 16

Robertson, H. P. 1937, Mon. Not. R. Astron. Soc., 97, 423 13

Robitaille, T. P., Whitney, B. A., Indebetouw, R., Wood, K., & Denzmore, P. 2006, Astrophys. J., Suppl. Ser., 167, 256 44

Rodríguez, L., D'Alessio, P., Wilner, D., et al. 1998, Nature, 395, 355 37

Rodríguez, L., Porras, A., Claussen, M., et al. 2003, Astrophys. J., Lett., 586, L137 37

Sandford, S. A. 1996, Meteoritics and Planetary Science, 31, 449 32

SAO Staff. 1995, VizieR Online Data Catalog, 1131, 0 65

Savage, R. S. & Oliver, S. 2007, Astrophys. J., 661, 1339 61

Schneider, G., Silverstone, M. D., Hines, D. C., et al. 2006, Astrophys. J., 650, 414 9

Shen, Y., Draine, B. T., & Johnson, E. T. 2009, Astrophys. J., 696, 2126 33

Sheret, I., Dent, W. R. F., & Wyatt, M. C. 2004, Mon. Not. R. Astron. Soc., 348, 1282 117

Shirahata, M., Matsuura, S., Hasegawa, S., et al. 2009, pasj, 61, 737 xxiv, 28

Shu, F., Najita, J., Galli, D., Ostriker, E., & Lizano, S. 1993, in Protostars and Planets III, ed. E. H. Levy & J. I. Lunine, 3–45 15

Shu, F. H. & Adams, F. C. 1987, in IAU Symposium, Vol. 122, Circumstellar Matter, ed. I. Appenzeller & C. Jordan, 7–22 12

Shu, F. H., Lizano, S., & Adams, F. C. 1987, in IAU Symposium, Vol. 115, Star Forming Regions, ed. M. Peimbert & J. Jugaku, 417–433 12

Skrutskie, M. F., Cutri, R. M., Stiening, R., et al. 2006, Astrophys. J., 131, 1163 39, 111

Smith, R., Churcher, L. J., Wyatt, M. C., Moerchen, M. M., & Telesco, C. M. 2009, Astron. Astrophys., 493, 299 9

Song, I., Zuckerman, B., & Bessell, M. S. 2003, Astrophys. J., 599, 342 20

Spangler, C., Sargent, A. I., Silverstone, M. D., Becklin, E. E., & Zuckerman, B. 2001, Astrophys. J., 555, 932 16

Stapelfeldt, K., Burrows, C. J., Krist, J. E., & WFPC2 Science Team. 1997, in IAU Symposium, Vol. 182, Herbig-Haro Flows and the Birth of Stars, ed. B. Reipurth & C. Bertout, 355–364 37

Stern, S. A. 1996, Astron. J., 112, 1203 20

Stojimirović, I., Narayanan, G., Snell, R. L., & Bally, J. 2006, Astrophys. J., 649, 280 36

Strubbe, L. E. & Chiang, E. I. 2006, Astrophys. J., 648, 652 26

Su, K. Y. L., Rieke, G. H., Misselt, K. A., et al. 2005, Astrophys. J., 628, 487 21, 32

Su, K. Y. L., Rieke, G. H., Stansberry, J. A., et al. 2006, Astrophys. J., 653, 675 16, 152

Su, K. Y. L., Rieke, G. H., Stapelfeldt, K. R., et al. 2009, Astrophys. J., 705, 314 126

Sumi, T. 2009, in American Institute of Physics Conference Series, Vol. 1158, American Institute of Physics Conference Series, ed. T. Usuda, M. Tamura, & M. Ishii, 239–242 125, 126

Swift, J. J. & Welch, W. J. 2008, Astrophys. J., Suppl. Ser., 174, 202 37

Swift, J. J., Welch, W. J., & Di Francesco, J. 2005, Astrophys. J., 620, 823 37

Swift, J. J., Welch, W. J., Di Francesco, J., & Stojimirović, I. 2006, Astrophys. J., 637, 392 37

Tachibana, S., Huss, G. R., Kita, N. T., Shimoda, G., & Morishita, Y. 2006, Astrophys. J., Lett., 639, L87 20

Thébault, P. & Augereau, J. 2007, Astron. Astrophys., 472, 169 xi, 4, 32, 33

Thompson, M. A., Smith, D. J. B., Stevens, J. A., et al. 2010, aap, 518, L134+ 124

Trilling, D. E., Bryden, G., Beichman, C. A., et al. 2008, Astrophys. J., 674, 1086 18, 69, 89

Trilling, D. E., Stansberry, J. A., Stapelfeldt, K. R., et al. 2007, Astrophys. J., 658, 1289 19, 69

van Boekel, R., Min, M., Leinert, C., et al. 2004, Nature, 432, 479 ix, 6, 7

van Boekel, R., Waters, L. B. F. M., Dominik, C., et al. 2003, Astron. Astrophys., 400, L21 8

van Leeuwen, F. 2007, Astron. Astrophys., 474, 653 126

Verdugo, E., Yamamura, I., & Pearson, C. 2007, AKARI FIS Data Users Manual, 1–107 x, xi, xii, xxiv, 28, 29, 52, 54, 57, 62

Vitense, C., Krivov, A. V., & Löhne, T. 2010, aap, 520, A32+ 109

Weinberger, A. J., Becklin, E. E., & Zuckerman, B. 2003, Astrophys. J., Lett., 584, L33 9

Weingartner, J. C. & Draine, B. T. 2001, Astrophys. J., 548, 296 34

White, G. J., Fridlund, C. W. M., Bergman, P., et al. 2006, Astrophys. J., Lett., 651, L41 36

White, G. J., Liseau, R., Men'shchikov, A. B., et al. 2000, Astron. Astrophys., 364, 741 36

Whittet, D. C. B., Boogert, A. C. A., Gerakines, P. A., et al. 1997, Astrophys. J., 490, 729 5

Williams, J. P. & Andrews, S. M. 2006, Astrophys. J., 653, 1480 26

Witt, A. 1989, in IAU Symposium, Vol. 135, Interstellar Dust, ed. L. J. Allamandola & A. G. G. M. Tielens, 87–+ 31

Wolf, S., Moro-Martín, A., & D'Angelo, G. 2007, Planet. Space Sci., 55, 569 11

Wolf, S. & Voshchinnikov, N. V. 2004, Computer Physics Communications, 162, 113 33

Wooden, D. H., Harker, D. E., Woodward, C. E., et al. 1999, Astrophys. J., 517, 1034 7

Wyatt, M. C. 2008, Ann. Rev. Astron. and Astrophys., 46, 339 ix, x, 17, 22, 23

Wyatt, M. C., Smith, R., Su, K. Y. L., et al. 2007, Astrophys. J., 663, 365 152

Zuckerman, B. 2001, Ann. Rev. Astron. and Astrophys., 39, 549 114

Zuckerman, B. & Becklin, E. E. 1993, Astrophys. J., 414, 793 25

Zuckerman, B., Song, I., Bessell, M. S., & Webb, R. A. 2001, Astrophys. J., Lett., 562, L87 7